Atmospheric Processes in a young Biomass Burning Plume

—

Radiation and Chemistry

Dissertation
zur Erlangung des Doktorgrades
der Naturwissenschaften
im Fachbereich Geowissenschaften
der Universität Hamburg

vorgelegt von

Jörg Trentmann
aus Osnabrück

Hamburg

2001

ISSN 0938 - 5177

Als Dissertation angenommen vom Fachbereich Geowissenschaften
der Universität Hamburg
auf Grund der Gutachten von Prof. Dr. H. Graßl
und Prof. Dr. M. O. Andreae

Hamburg, den

Prof. Dr. U. Bismayer

Dekan des Fachbereichs Geowissenschaften

Abstract

Biomass burning contributes significantly to the global budgets of a number of atmospheric trace gases and particles. The gaseous emissions are involved in photochemical formation of tropospheric ozone. The particulate emissions contribute to the direct and indirect effect of the aerosol on the radiation budget of the earth-atmosphere system.

In this thesis, atmospheric processes in young biomass burning plumes in the first tens of minutes are investigated. For this purpose, the three-dimensional (3D) atmospheric plume model ATHAM is used to simulate the evolution of a biomass burning plume. The simulation represents the situation during the Quinault prescribed fire conducted during the Smoke, Cloud, and Radiation-C (SCAR-C) experiment. The model reproduces well the general appearance of the plume and the observed aerosol mass concentrations. Remaining differences between the model results and the measurements are attributed to limited meteorological and fire emission information. Remote sensing measurements indicate a lower limit for the single-scattering albedo, ω, of the emitted biomass burning aerosol at 550 nm of 0.94. The calculation of ω based on in situ measurements results in a significant lower value of 0.85. Possible reasons for this discrepancy are discussed.

Three-dimensional solar radiative transfer simulations show that horizontal photon transfer significantly influences the actinic flux in the center of the biomass burning plume. The magnitude of this 3D radiation effect depends on the absorbing properties of the aerosol and can influence photochemistry in biomass burning plumes and other phenomena of similar dimensions, e.g., convective clouds. For the interpretation of measurements of the upward irradiance above finite plumes, the use of one-dimensional (1D) radiative transfer models is inappropriate because of the decreasing solid angle of the plume with increasing altitude. This effect cannot be taken into account in 1D radiative transfer simulations.

Atmospheric photochemistry in young biomass burning plumes leads to the formation of ozone and nitrogen reservoir species. The simulated ozone mixing ratio of about 70 ppb agrees well with the observations from the Quinault fire. Significant production of nitrogen reservoir species is simulated with HNO_3 and peroxyacetyl nitrate (PAN) accounting for about $\sim 60\%$ and $\sim 30\%$, respectively. The availability of radicals is the limiting factor for photochemistry in the plume. Production of radicals is dominated by photolysis of formaldehyde ($\sim 80\%$ of the total radical production). The concentrations of the alkenes are significantly reduced by oxidation in the plume. Neglecting the emission of formaldehyde from the fire leads to unrealistic low ozone concentrations. Decreasing the emissions of nitrogen oxides as

well as neglecting aerosol absorption lead to an increase in the ozone concentrations within the range of observations.

Overall, it appears that young biomass burning plumes are a highly interesting research field for several disciplines in the atmospheric science. Plumes from vegetation fires include a number of atmospheric processes and offer the potential to combine field observations and modeling studies.

Contents

Chapter 1

Introduction

Fires must have existed on Earth and influenced its atmosphere since the evolution of land plants, some 350 to 400 million years ago. Before humans learnt to use fire as an active tool, about 2 million years ago, fires were naturally ignited mostly by lightning strikes. Today, fires result almost exclusively from human activity. Only in the boreal and savanna regions of the world, natural wildfires play a significant role where they occur with a frequency of 3 to 5 years and some tens of years, respectively [*Andreae*, 1991, 1993; *Andreae and Merlet*, 2001].

The term biomass burning includes vegetation fires as well as other human uses of fire, e.g., the use of fuelwood for cooking and heating and the burning of agricultural residues. However, vegetation fires account for about 2/3 of the mass of global biomass burned [*Andreae*, 1993].

Despite the long tradition of fire as a cause for atmospheric pollution, only very few investigations on the impact of fire on the atmospheric composition were published before the late 1970s focussing on local effects [*Hobbs and Radke*, 1969; *Hobbs and Locatelli*, 1969; *Pueschel and Langer*, 1973; *Evans et al.*, 1974, 1977; *Radke et al.*, 1978]. Scientific interest in biomass burning grew in the early 1980s when estimates suggested that biomass burning could rival fossil fuel burning as a source of atmospheric pollution [*Crutzen et al.*, 1979; *Seiler and Crutzen*, 1980; *Crutzen and Andreae*, 1990]. Additional, it became evident that these emissions could effect large areas as a consequence of long-range transport [*Andreae*, 1983; *Reichle et al.*, 1986; *Watson et al.*, 1990; *Fishman et al.*, 1990].

Since the mid 1980s large efforts have been made in order to characterize and quantify the emissions from biomass burning. Several measurement campaigns focused on the emission from fires and their impact on atmospheric chemistry. These include FOS/DECAFE91 (Fire of Savannas/Dynamique et Chimie de l'Atmosphère en Forêt Equatoriale 91) in West Africa [*Lacaux et al.*, 1995], SAFARI-92 (Southern African Fire-Atmosphere Research Initiative) [*Andreae et al.*, 1996b; *Lindesay et al.*,

1996] and TRACE-A (Transport and Atmospheric Chemistry near the Equator-Atlantic) [*Fishman et al.*, 1996] over Brazil, southern Africa and the South Atlantic, SCAR-B (Smoke, Clouds, and Radiation - Brazil) [*Kaufman et al.*, 1998] in Brazil, and EXPRESSO (Experiment for Regional Sources and Sinks of Oxidants) in Central Africa [*Delmas et al.*, 1999]. Additionally, numerous ground based, airborne, and spaceborne observations have shown the impact of biomass burning on the regional and global atmosphere [*Fishman et al.*, 1991; *Andreae et al.*, 1994; *Kent et al.*, 1998; *Waibel et al.*, 1999; *Connors et al.*, 1999; *Wotawa and Trainer*, 2000; *Singh et al.*, 2000; *Jones et al.*, 2001; *Thompson et al.*, 2001].

1.1 Significance of Biomass Burning

Most of the vegetation fires occur in the tropics during the dry season [*Dwyer et al.*, 1998]. Based on satellite observations and information from the Food and Agricultural Organization (FAO) of the United Nations supplemented by additional information, global databases of the spatial and temporal distribution of biomass burning were established [*Hao and Liu*, 1994; *Lobert et al.*, 1999; *Galanter et al.*, 2000]. Figure 1.1 presents the spatial distribution of the emission of carbon monoxide, CO, one of main emission products from biomass burning, for four months taken from the database of *Galanter et al.* [2000]. The seasonal change in the spatial distribution of the emission is easy to recognize. In the tropics, it closely follows the dry season. In the boreal region, fire emissions maximize during the summer.

The gaseous and particulate emissions from biomass burning are involved in several atmospheric processes with potential importance for local air quality as well as for the regional and global climate. Trace gas emissions from biomass burning include nitrogen oxides and reactive organic compounds [*Andreae and Merlet*, 2001]. In the troposphere, the oxidation of these organic compounds in the presence of nitrogen oxides leads to photochemical formation of ozone [*Seinfeld and Pandis*, 1998; *Crutzen et al.*, 1999]. Tropospheric ozone is harmful to plants, animals and humans [*McKee*, 1993], and one of the most important greenhouse gases [*Ramaswamy et al.*, 2001]. Additionally, ozone is the central compound for tropospheric chemistry, because it serves as the primary precursor for the hydroxy radical, OH, the detergent of the atmosphere [*Crutzen et al.*, 1999]. Satellite observations and airborne measurements have shown that the emissions from biomass burning enhance the tropospheric ozone concentration on a regional to global scale [*Fishman et al.*, 1991; *Browell et al.*, 1996; *Fenn et al.*, 1999; *Thompson et al.*, 2001].

The particulate emissions from biomass burning alter the atmospheric energy budget by modifying the amount of reflected solar radiation from the earth-atmosphere system, the so called 'direct' effect, and by modifying the properties of clouds,

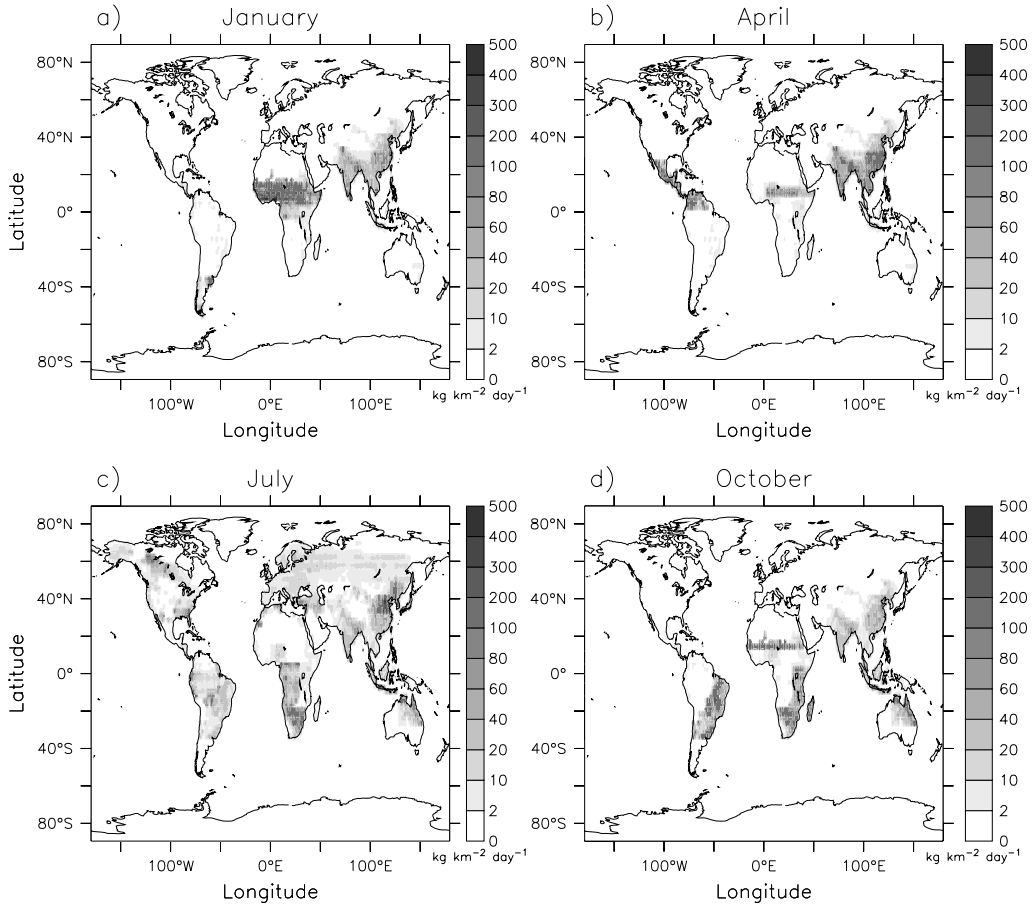

Figure 1.1: Spatial distribution of the mean CO emission flux from biomass burning for (a) January, (b) April, (c) July, and (d) October [*Galanter et al.*, 2000].

the so called 'indirect' effect. The direct effect is strongly linked to the optical properties of the biomass burning aerosol. Especially the absorption of the particles as well as their size distribution determine their importance for the atmospheric radiation budget. The current estimate for the radiative forcing of the aerosol from biomass burning based on several model results is -0.2 W m^{-2} with a range from -0.07 to -0.6 W m^{-2} [*Ramaswamy et al.*, 2001]. The interaction of the biomass burning aerosol with clouds has at least two implications. The first indirect effect describes the increase in the number of cloud droplets and the decrease in cloud droplet size [*Twomey*, 1974]. This enhances the reflection of solar radiation in aerosol-affected clouds. This effect was observed in clouds affected from smoke aerosol over Brazil [*Kaufman and Fraser*, 1997]. However, the absorption of the biomass burning aerosol might also decrease the reflection of the clouds [*Kaufman and Nakajima*, 1993]. The second indirect effect refers to the change in cloud microphysics due to smaller cloud droplets leading to a reduced precipitation efficiency

and longer lifetimes of clouds [*Albrecht*, 1989]. This effect was observed in clouds over Indonesia from satellite measurements [*Rosenfeld*, 1999]. Model studies indicate, that this effect has the potential to impact the atmospheric circulation on the regional up to the global scale [*Graf et al.*, 2001].

1.2 Impact of Biomass Burning Emissions on Atmospheric Chemistry

Tropospheric chemistry is driven by the oxidation of organic compounds that are released into the atmosphere by natural processes and human activities. Whether ozone is produced in the chemical oxidation cycles depends on the concentrations of several compounds, especially on that of the nitrogen oxides. However, this dependency is highly non-linear. Significant photochemical ozone production and formation of nitrogen reservoir species occurs close to the sources of pollution in the atmospheric boundary layer. Atmospheric transport couples these local processes to the regional and global scale leading to enhanced ozone and nitrogen reservoir concentrations. The release of the nitrogen from the reservoir species into the form of nitrogen oxides enhances photochemical ozone production far from the source regions.

The impact of biomass burning on the composition of the atmosphere occurs on two different scales. On the scale of individual plumes from vegetation fires, atmospheric chemical reactions take place in a highly concentrated mixture of nitrogen oxides and organic compounds. Especially the compounds that undergo fast photochemical reactions in the atmosphere determine the processes on this scale. On a larger scale, biomass burning emissions enhance the concentrations of nitrogen oxides and long-lived organic compounds, and therefore impact regional atmospheric chemistry.

The regional and global impact of biomass burning is influenced by local processes close to fires. The fire emissions are transported with the fire-induced convection into the atmosphere. This injection height has a strong impact on the regional transport of the emissions and on the atmospheric photochemistry. The possible formation of a convective cloud above a fire leads to effective uptake of soluble gases and aerosol particles into the cloud droplets and subsequent removal from the atmosphere. Possible photochemical formation of soluble compounds, e.g., nitric acid, in the plume could enhance this removal. Because ozone production depends highly non-linear on the concentrations of the trace gases, chemical processes in individual biomass burning plumes with high concentrations of trace gases might be significant. Based on observations, the contribution of ozone production in biomass burning plumes to the total ozone production was estimated be negligible in the bo-

real region [*Mauzerall et al.*, 1996]. However, in the tropical South Atlantic region, most of the atmospheric ozone production occurs in plumes [*Mauzerall et al.*, 1998].

Atmospheric chemical transport models include the emissions from biomass burning. Several studies estimate the impact of biomass burning to the tropospheric ozone concentration to be in the range of 10% [e.g., *Lelieveld and Dentener*, 2000; *Marufu et al.*, 2000; *Galanter et al.*, 2000; *Granier et al.*, 2000]. In the boundary layer over Africa, biomass burning contributes to $\sim$24% of the ozone concentration [*Marufu et al.*, 2000]. However, photochemical processes occurring within individual biomass burning plumes cannot be considered in these kind of models, because of their comparably large horizontal grid spacing in the order of 100 km and their long time step in the order of tens of minutes. Therefore, the high concentrations that are found in individual plumes as well as the local transport effects are not reproduced in these models.

Global models tend to underestimate ozone concentrations in tropical biomass burning regions, although the concentrations of CO are reproduced reasonably well [*Emmons et al.*, 2000]. Nitric acid concentrations are overestimated in these models, especially in biomass burning regions [*Wang et al.*, 1998b; *Hauglustaine et al.*, 1998; *Lawrence et al.*, 1999]. A comparison of NO_2 satellite measurements with a global model revealed little deviations over the regions of burning, but showed an underestimation of the modeled NO_2 mixing ratio in areas downwind the burning, e.g., the southern Atlantic [*von Kuhlmann*, 2001]. These differences point to limitations in the representation of the chemical processes in fire-affected regions in global atmospheric chemistry transport models.

1.3 Motivation

The aim of this thesis is to improve our understanding of the chemical processes that occur in individual biomass burning plumes. Detailed knowledge of these processes is the necessary requirement for a better characterization of the emissions from biomass burning. Model simulations are well suited in order to investigate the different processes, because they allow the determination of the impact of single processes in the simulations. However, in order to assure a realistic representation of the atmospheric processes, the model results have to be evaluated with appropriate observations.

On a Dahlem conference in Berlin, 1992, is was concluded that "dynamic cloud models, with heat and aerosol emission rates from fires [...] complemented with atmospheric chemistry and emission description could provide important insights into the chemistry and scavenging of trace gases and aerosols in the near-source region and would be of great assistance in the development of parameterizations

needed by regional and global models." [*Crutzen and Carmichael*, 1993]. However, no such model was available at the beginning of this work.

In this thesis, for the first time, simulations of the atmospheric transport of fire emissions and the chemical evolution of an individual biomass burning plume are presented. For this purpose, the active tracer high-resolution atmospheric model (ATHAM) [*Herzog et al.*, 1998; *Oberhuber et al.*, 1998] was expanded by the inclusion of fire emissions and a chemical mechanism. ATHAM is well suited for this type of studies, because it was designed and used for the simulation of vulcano eruptions [*Graf et al.*, 1999]. Additional modules treat the microphysical processes leading to the formation of cloud water and ice as well as scavenging of trace gases and aerosol particles [*Textor*, 1999]. With the inclusion of a chemical module, ATHAM treats all important atmospheric processes that occur in biomass burning plumes.

In order to evaluate the model results with observations, simulations were performed for the conditions during the Quinault prescribed fire conducted during the Smoke, Cloud, and Radiation-C (SCAR-C) experiment in the Pacific Northwest of the United States [*Kaufman et al.*, 1996; *Hobbs et al.*, 1996; *Martins et al.*, 1996]. This 19.4-ha clearcut burn on the North American Pacific Coast on the Olympic Peninsula, was ignited in order to study the evolution of the plume from different observational platforms, e.g., a low altitude aircraft performing in situ measurements as well as a high altitude aircraft for remote sensing observations. Additionally, information about the heat release of the fire is available from model simulations. All available information from the observations were incorporated into the model simulations.

Different aspects of the biomass burning plume are investigated. These include the dynamical evolution of the plume, the optical properties of the aerosol, solar radiative transfer in the plume, and the chemical processes leading to the formation of ozone and nitrogen reservoir species. This thesis contains three main chapters, each of those deals with a different aspect of the plume from the Quinault fire. In Chapter 2, the meteorological situation during the Quinault fire is presented. Based on the fire emissions, the transport of the emitted aerosol particles is simulated and the results are compared to observations. The optical properties of the aerosol, especially their absorbing efficiency, is investigated with the help of radiative transfer calculations in combination with measurements of the reflected solar irradiance and radiance. Chapter 3 presents the results from three-dimensional solar radiative transfer calculations using the simulated aerosol plume presented in Chapter 2. Especially, the impact of three-dimensional solar radiative transfer on the actinic flux in the plume and on the reflected irradiance are be addressed. In Chapter 4, the chemical processes in the plume of the Quinault fire are investigated. For this purpose, a reduced chemical mechanism is presented for the use in three-dimensional

atmospheric transport models. The simulated concentrations of ozone and nitrogen compounds are evaluated with measurements and the most important aspects of the photochemistry in a young biomass burning plume are be discussed. Chapter 5 summarizes the main results of this work and an outlook for possible future research directions resulting from the present work are given.

Each of the main chapters is based on a publication in a scientific journal. It therefore includes a separate abstract, introduction, and conclusion. In order to focus on the scientific results, the numerical models used in this study are described only briefly, highlighting the relevant parts for this work. If additional information is required, the reader is referred to the references given. For a general introduction into the atmospheric processes, the reader is referred to available textbooks [e.g., *Seinfeld and Pandis*, 1998; *Jacobson*, 1998b; *Brasseur et al.*, 1999; *Warneck*, 1999].

Chapter 2

Simulation of a Biomass Burning Plume: Comparison of Model Results with Observations[1]

Abstract. In this chapter, results from the simulation of the dynamical evolution of the plume from a prescribed biomass fire, using the active tracer high-resolution atmospheric model (ATHAM) are presented. Initialization parameters were set to reflect the conditions during the fire. The model results are compared with airborne remote sensing and in situ measurements of the plume. ATHAM reproduces the injection height (250 m to 600 m) and the horizontal extent of the plume ($\sim$4 km) with good accuracy. The aerosol mass concentrations are underestimated, but still in the range of the observations. Remaining differences between the model results and the measurements are attributed to limited meteorological and fire emission information. Additionally, one-dimensional radiative transfer simulations are performed. Using the ATHAM-generated spatial aerosol distribution, a comparison between the measured and simulated upward irradiance yields an underestimation by the model over the ocean surface, which is most likely due to an underestimation of the aerosol optical depth in the model. Analysis of the upwelling radiance above the plume using variable aerosol optical depths yields a lower limit for the aerosol single-scattering albedo at 550 nm of 0.94, which is larger than derived from in situ measurements.

Overall it appears that ATHAM is a valuable tool for the investigation of transport processes within biomass burning plumes and, together with a chemical and microphysical module, is suitable for studies of the interaction between transport, chemistry and microphysics within such plumes.

[1]Parts of this chapter are accepted for publication in the *Journal of Geophysical Research,* 2002, with M. O. Andreae, H.-F. Graf, P. V. Hobbs, R. D. Ottmar, and T. Trautmann as coauthors.

2.1 Introduction

Vegetation fires are known to be a major contributor to the global budgets of several trace gases (e.g., CO, CH_4, and NO_x) as well as aerosol particles [*Crutzen and Andreae*, 1990]. The regional and global effects from fire emissions have been demonstrated in field campaigns, such as the Transport and Atmospheric Chemistry near the Equator-Atlantic (TRACE-A), Southern African Fire-Atmosphere Research Initiative (SAFARI) [*Andreae et al.*, 1996b] and the Smoke, Clouds, and Radiation - Brazil (SCAR-B) [*Kaufman et al.*, 1998], and in modeling studies [e.g. *Chatfield et al.*, 1998; *Galanter et al.*, 2000]. The regional and global impacts of vegetation fires on atmospheric composition depend on the processes that take place near the fire, e.g., the height of the injection of the emissions [*Liousse et al.*, 1996], the nonlinear production of ozone [*Poppe et al.*, 1998], and the possible formation of clouds and scavenging of the emissions [*Radke et al.*, 1991]. Therefore, *Crutzen and Carmichael* [1993] concluded that small-scale models "complemented with atmospheric chemistry and emission description could provide important insights into the chemistry and scavenging of trace gases and aerosols in the near-source region and would be of great assistance in the development of parameterizations needed by regional and global models."

However, until now, no such model studies have been performed. Existing models of coupled fire dynamics and meteorology focus mainly on the fire dynamics [*Clark et al.*, 1996; *Grishin*, 1996] and do not include detailed atmospheric processes. The only numerical simulation of the atmospheric transport of particles from a vegetation fire and their interaction with clouds did not include quantitative comparisons with observations [*Penner et al.*, 1991].

Here, model simulations of the atmospheric transport of aerosol particles from a vegetation fire using the nonhydrostatic active tracer high-resolution atmospheric model (ATHAM) [*Oberhuber et al.*, 1998; *Herzog et al.*, 1998] are presented. The atmospheric conditions, and the heat and particle fluxes from the fire used in the model simulation correspond to those of a prescribed fire conducted on 21 September 1994 during the Smoke, Cloud, and Radiation-C (SCAR-C) experiment in the Pacific Northwest of the United States [*Kaufman et al.*, 1996]. The simulated aerosol concentrations are compared with in situ and remote sensing measurements of the smoke plume from this fire [*Kaufman et al.*, 1996; *Hobbs et al.*, 1996; *Martins et al.*, 1996].

The primary aim of this chapter is the evaluation of the general features of the model results, rather than a detailed comparison with the observations. A comprehensive comparison between model results and observations of natural biomass burning plumes is probably impossible because of the high temporal and spatial variability of the emissions, which cannot be adequately represented in this kind

of model. The model was initialized on the basis of observational data in order to constrain model assumptions as far as possible.

2.2 Model Description

ATHAM was used for the study of eruptive volcanic plumes by *Graf et al.* [1999]. Only a short description of the model is given here. For a more detailed description of the model the reader is referred to *Oberhuber et al.* [1998] and *Herzog et al.* [1998].

The nonhydrostatic plume model ATHAM has a modular structure, which allows easy coupling of new modules. Existing modules treat the dynamics, turbulence, transport, cloud microphysics, gas scavenging, and radiation. The Navier–Stokes equations for the volume-mean of a gas–particle mixture, including the transport of active tracers, are solved in the dynamical part of the model. Active tracers influence the simulated density and heat capacity within the model grid boxes and therefore affect the modeled dynamics. Turbulent exchange coefficients for each dynamic variable are computed with a turbulence closure scheme. Atmospheric transport of the active and passive tracers is treated using the method of *Smolarkiewicz* [1984], and the advection of heat and turbulent quantities are described using a scheme similar to *Crowley* [1968]. The cloud microphysics is based on a Kessler-type parameterization and describes condensation and formation of precipitation as well as the scavenging of soluble gases [*Textor*, 1999]. The fire is represented by heat and particulate fluxes into the lowest vertical model layer at prescribed grid boxes. There is no feedback from the atmospheric wind field on the fluxes from the fire.

The calculation of the heating rates and the radiative forcing are performed with the radiative transfer model described by *Loughlin et al.* [1997], which is based on the 2-stream practical improved flux method (PIFM) [*Zdunkowski et al.*, 1982] and includes radiative effects of gases, aerosol particles, and clouds. Alternatively, the radiative transfer model described in *Langmann et al.* [1998] can be used. In the present study the PIFM model is used. According to *Briegleb et al.* [1986], the lambertian surface albedo for land is set to 4% for $\lambda < 690$ nm and 25% for $\lambda > 690$ nm. For the ocean surface, an albedo of 6% for the diffuse light is used, while for the direct light the solar zenith angle dependency is taken into account [*Briegleb et al.*, 1986].

ATHAM is formulated three-dimensionally on a horizontally and vertically stretched Cartesian grid with an implicit time stepping scheme. Besides the three-dimensional (3D) model version a 2D cartesian and a 2D cylindrical version exist. In this study only 3D model results are presented.

Figure 2.1: Photograph of the smoke plume produced from the Quinault prescribed fire at 1250 LT, at about 100 min after the ignition. (Photo taken by R. Ottmar, reproduced from *Kaufman et al.* [1996] with the permission of the MIT Press.)

2.3 The SCAR-C Experiment

The SCAR-C experiment was conducted in September 1994 in the Pacific Northwest of the United States. A detailed description of the campaign is given by *Kaufman et al.* [1996] and *Hobbs et al.* [1996]. Only an overview is given here.

The emphasis of SCAR-C was "on measuring the entire process of biomass burning, including ground-based estimates of fuel consumption, airborne sampling of the smoke aerosols and trace gases, and airborne and spaceborne remote sensing of both the fires and the smoke" [*Kaufman et al.*, 1996]. In the present study, the prescribed fire on 21 September 1994 on the Pacific Coast of Washington State in the Quinault Indian Reservation on the Olympic Peninsula (47.32° N, 124.27° W) will be investigated. The Quinault fire was a 19.4-ha clearcut burn, with fuel consisting of the dry remnants of large western red cedar debris left over from logging [*Kaufman et al.*, 1996]. Measurements before and during this fire included fuel loadings, airborne in situ measurements of trace gases and particles, and airborne remote sensing observations of the fire and the smoke plume from the University of Washington's Convair C-131A and NASA's ER-2 research aircrafts [*Kaufman et al.*, 1996; *Hobbs et al.*, 1996; *Martins et al.*, 1996]. The ignition sequence was started at 1105 LT (local time). Figure 2.1 shows a photograph of the smoke plume above the fire at about 100 minutes after the ignition. The smoke was first lofted directly above the

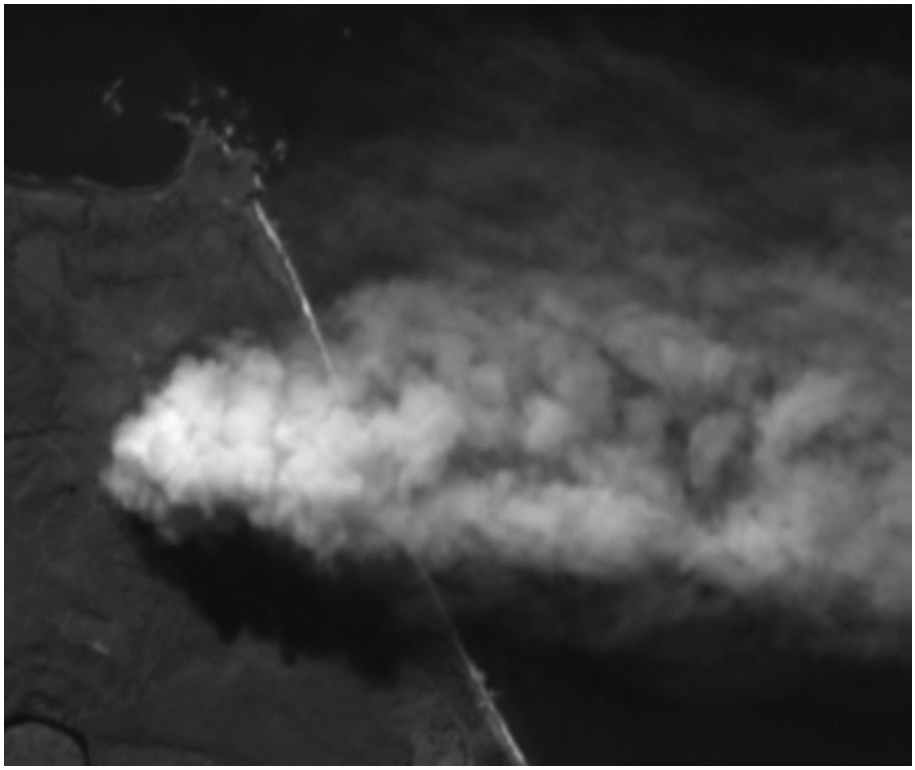

Figure 2.2: View of the smoke plume from the Quinault prescribed fire derived from spectral measurements taken from the AVIRIS instrument onboard the ER-2 aircraft at 1243 LT, about 95 min after ignition. This picture was created using the spectral measurements at 750 nm, 650 nm, and 550 nm for the RGB color palette. Calibrated AVIRIS data were obtained from Robert Green, JPL.

fire up to about 600 m. It was then transported by the prevailing wind out over the Pacific Ocean (Figure 2.2). Figure 2.2 was obtained from spectral measurements of the airborne visible/infrared imaging spectrometer (AVIRIS) [*Green et al.*, 1998] on board the NASA ER-2 aircraft. The high variability in the smoke loading is easily seen in Figures 2.1 and 2.2.

As the plume remained intact and was readily discernible over a long distance, and there are no terrain-induced effects over the ocean, this fire presents an excellent opportunity to study the processes within a biomass burning plume using an atmospheric model. Besides the detailed analysis of the in situ measurements [*Hobbs et al.*, 1996; *Martins et al.*, 1996], the remote sensing observations of the smoke plume have been used in previous studies for the retrieval of aerosol properties [*Tanré et al.*, 1997] and for a comparison of remote sensing retrieved aerosol properties with the in situ measurements [*Gassó and Hegg*, 1998].

2.4 Model Initialization

In this section, the model setup for the simulations, the atmospheric initial conditions, the emissions of the fire, and the calculated optical aerosol properties are presented. Initialized with the meteorological variables, ATHAM calculates the wind field resulting from the thermal forcing of the fire. In particular, the induced vertical wind due to the heating from the fire is simulated. The emitted aerosol particles are transported with this simulated wind.

2.4.1 Model Setup

The model domain (x,y,z) of the 3-D ATHAM version was set to 35 km $\times$ 28 km $\times$ 3.75 km, with a minimal grid spacing of 50 m $\times$ 50 m $\times$ 20 m in the central part of the model domain where the fire forcing was initialized. The number of grid boxes in the x-, y-, and z-direction was 120, 110, and 80, respectively, resulting in 1 056 000 model grid boxes. The time step is determined automatically by the Courant–Friedrichs–Lewy (CFL) criterion; it lies usually in the range of 3 to 8 s. The model simulations were started at 1100 LT, with a spin-up time of 6 min before the ignition of the fire. In this chapter, model results at 100 min after fire ignition are presented.

2.4.2 Initial Profiles of Meteorological Variables

The atmospheric initial conditions for the simulations are taken from airborne measurements aboard the Convair C-131A before the ignition of the fire (between 1100 LT and 1111 LT); these initial profiles are shown in Figure 2.3. The airborne measurements were available between altitudes of 320 m and 1890 m. Above 1890 m, atmospheric conditions from a radiosonde [*CODIAC*, 1999], supplemented by data from the US Standard Atmosphere [*Anderson et al.*, 1986], were used. From the surface up to 200 m a dry adiabatic lapse rate was assumed. From 200 to 320 m an increase in temperature to the values measured at 320 m was taken on the basis of other temperature profiles measured during the flight of the Convair 131A. Since the relative humidity does not affect the dynamic evolution of the model simulations, it was set to a constant value below 300 m. The horizontal wind speed was assumed to decrease to zero below 225 m, based on the visual observations shown in Figure 2.1. The atmospheric conditions above 1500 m do not influence the model results and are not included in Figure 2.3. Also not shown in Figure 2.3 is the wind direction, which is, however, included in the model simulations: between 300 m and 800 m easterly winds prevailed, and between 800 m and 1100 m the wind changed to northerly.

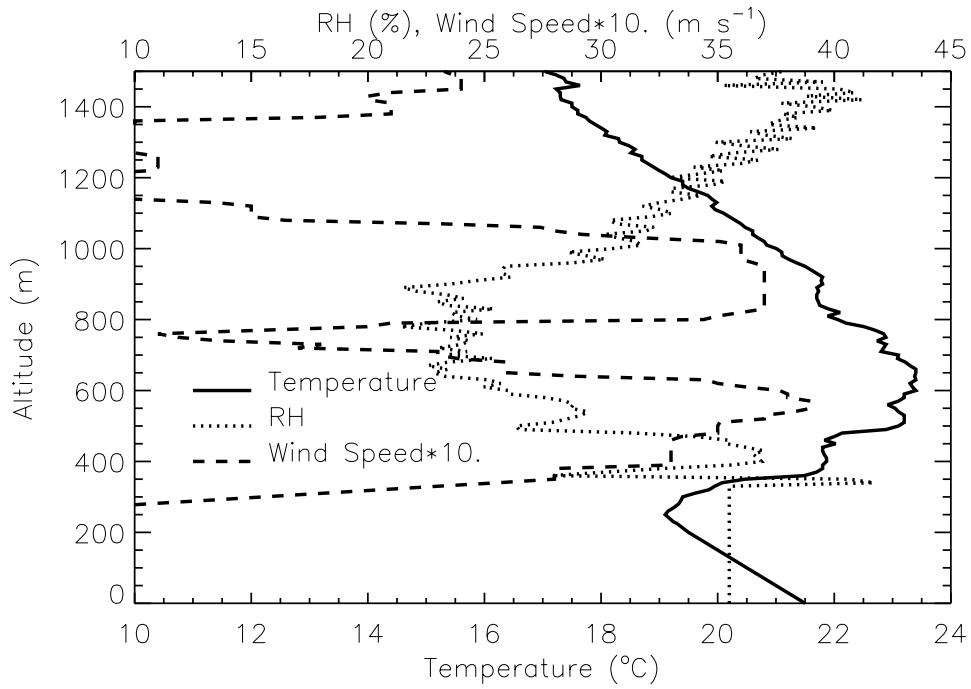

Figure 2.3: Initial atmospheric profiles of the temperature (lower axis), relative humidity (RH) (upper axis), and horizontal wind speed (upper axis) up to an altitude of 1.5 km used in the model simulations. Above 320 m, aircraft measurements are used. For the values below this altitude, see the text.

The main feature of the atmospheric profile is the strong temperature inversion between 300 m and 600 m. The temperature profile above 600 m is dry stable with a lapse rate of -0.73 K/100 m. The relative humidity is quite low with maximum values around 40%. The maximum wind speed is 4 m s^{-1}.

The whole model domain was initialized with the same atmospheric profile. Since the region of interest was located near the coast, the assumption of horizontal homogeneity of the atmosphere is probably not fulfilled in reality and may lead to discrepancies between the model results and observations. Unfortunately, there is no information about the horizontal variations of the atmospheric profile before the fire.

2.4.3 Fire Emissions

Fire emissions of energy and particles (shown in Figure 2.4) were obtained using the emission production model (EPM) [*Sandberg and Peterson*, 1984; *Ferguson et al.*, 2000]. EPM takes into account the loading, consumption, and moisture of different fuel size classes and the duff. Additionally, information about the method of ignition

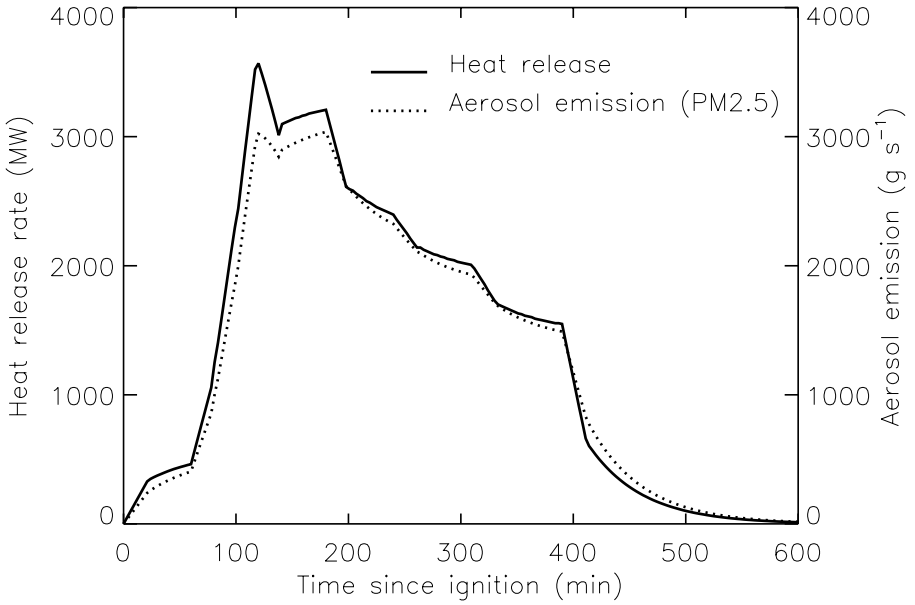

Figure 2.4: Convective heat and particle (<2.5 μm diameter) emission over time for the Quinault fire, calculated using the EPM model.

and the overall size of the fire is taken into account. The parameters used for the Quinault fire are given in Table 66.1 of *Hobbs et al.* [1996]. With theses parameters, EPM calculates the time-dependent emissions of energy, particulate matter (diameter < 2.5 μm, PM2.5), and some trace gases (CO_2, CO, CH_4), accounting for different phases of the fire (flaming and smoldering). The emission factors are taken from the Compilation of Air Pollutant Emission Factors (AP-42) provided by the United States Environmental Protection Agency (US EPA) (available on the Internet: http://www.epa.gov/ttn/chief/ap42/index.html). For the Quinault fire the values for the PM2.5 emission factor ranged between 6 and 17 g kg^{-1} depending on the fuel type and the phase of the fire. The modeled values for the total energy emissions are multiplied by the factor 0.55 to account only for convective energy [*McCarter and Broido*, 1965, S. Ferguson, personal comm., 1999]. This factor depends on several characteristics of the fuel. The value used here is in the middle of the commonly accepted range of 0.4 to 0.8 [*Ferguson et al.*, 2000]. These spatially integrated emissions are introduced into ATHAM as fluxes into the lowest model layer. The spatial distribution of fire pixels in the model was set following Figure 65.2 in *Kaufman et al.* [1996]. and is shown in Figure 2.5. The 10 subunits were 'ignited' in the model simulations according to the information from the ignition sequence of the U.S. Forest Service. The total ignition time was 35 minutes.

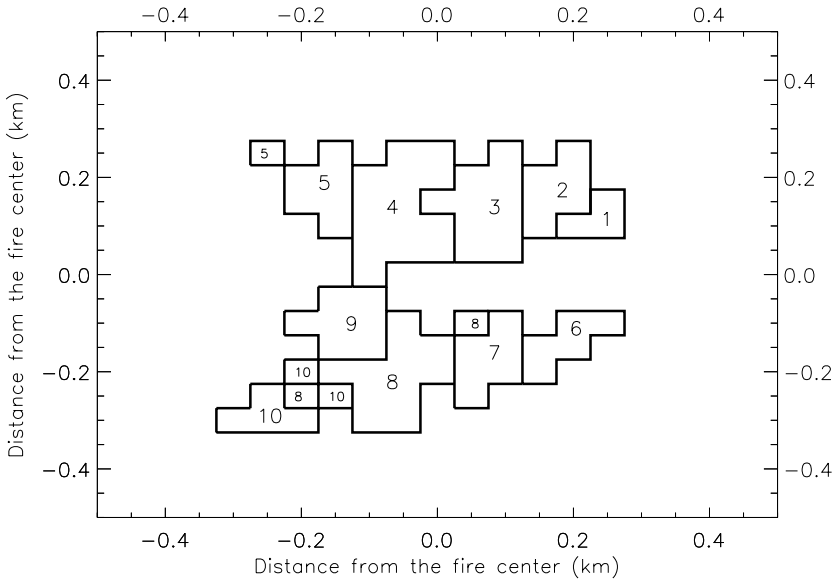

Figure 2.5: Fire pixels used in the model simulations. The 10 subplots were 'ignited' successively according to information from the ignition sequence from the observations. Total ignition time was 35 min.

2.4.4 Aerosol Optical Properties

To simulate atmospheric radiative transfer and calculate atmospheric heating rates, the wavelength-dependent aerosol optical properties are needed. If the number distribution and the refractive index of the aerosol particles are known, and if the particles are assumed to be spherical, their optical properties can be calculated from Mie theory. The number distribution of the aerosol in the smoke plume was measured from the aircraft using three instruments as described by *Hobbs et al.* [1996] and *Gassó and Hegg* [1998]. For the present study, a size distribution that was measured with a differential mobility particle sizing system (DMPS) between 0.01 and 0.56 μm diameter at a distance of 7.6 km from the fire (see Figure 2.6) was used. As shown by *Gassó and Hegg* [1998], the size distribution varied along the length of the plume, especially close to the fire. This study focuses on the plume properties further downwind, where the particle size distribution did not change so much. Therefor, the size distribution shown in Figure 2.6 is assumed to be representative for most parts of the plume. Also included in Figure 2.6 is a fitted curve based on the sum of two log-normal distributions. The resulting effective particle radius of 0.14 μm is in reasonable agreement with the value of 0.127 μm given by *Gassó and Hegg* [1998]. The fitted curve is used for the calculation of the wavelength-dependent optical properties of the aerosol particles.

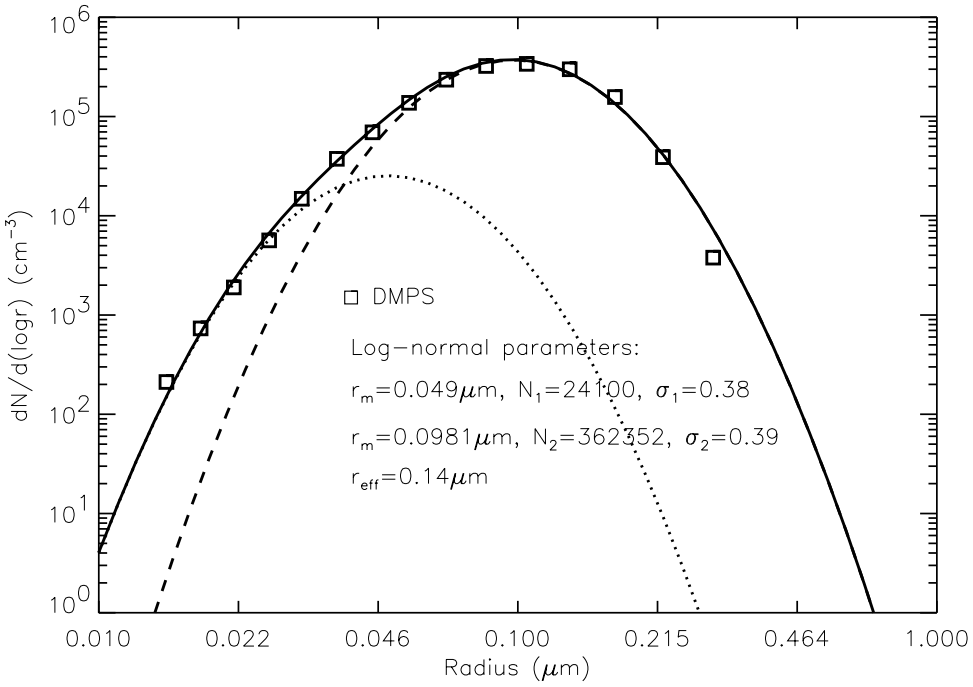

Figure 2.6: DMPS measurement of the particle number size distribution in the range 0.005−0.28 μm radius (squares) at an approximate distance of 7.6 km from the fire at 1247 LT (about 100 min after ignition). Also included is the sum of two log-normal distributions (solid line) as well as the two log-normal distributions (dotted and dashed lines). The sum of the log-normal distributions is used in the calculation of the optical properties of the particles.

The black carbon (BC) content of the aerosol particles determines their absorbing properties. For the particles from the Quinault fire, the BC mass content was determined to be 8 ± 1.2% from reflectance technique and 7.7% from thermal measurements [*Martins et al.*, 1996]. A value of 8% was used for the simulations of the optical properties. The remaining particle mass is assumed to be organic carbon (OC) [*Martins et al.*, 1996; *McDow et al.*, 1996].

A wavelength-dependent refractive index of the aerosol particles has to be assumed for the Mie calculations of the optical properties. For the BC part, the values from *Fenn et al.* [1985] for soot are used. In the wavelength region between 2 and 19 μm, the values of *Sutherland and Khanna* [1991] are taken for OC. Outside this wavelength range, only very limited information about the refractive index of OC exists. The values commonly used are between 1.43 and 1.54 for the real part of the refractive index and 0 and 0.0035 for the imaginary part with little wavelength dependence [*Sloane*, 1983; *Holben et al.*, 1991; *Krekov*, 1992; *Ross et al.*, 1998]. As the refractive index of ammonium sulfate, $(NH_4)_2SO_4$, shows a similar behavior, the

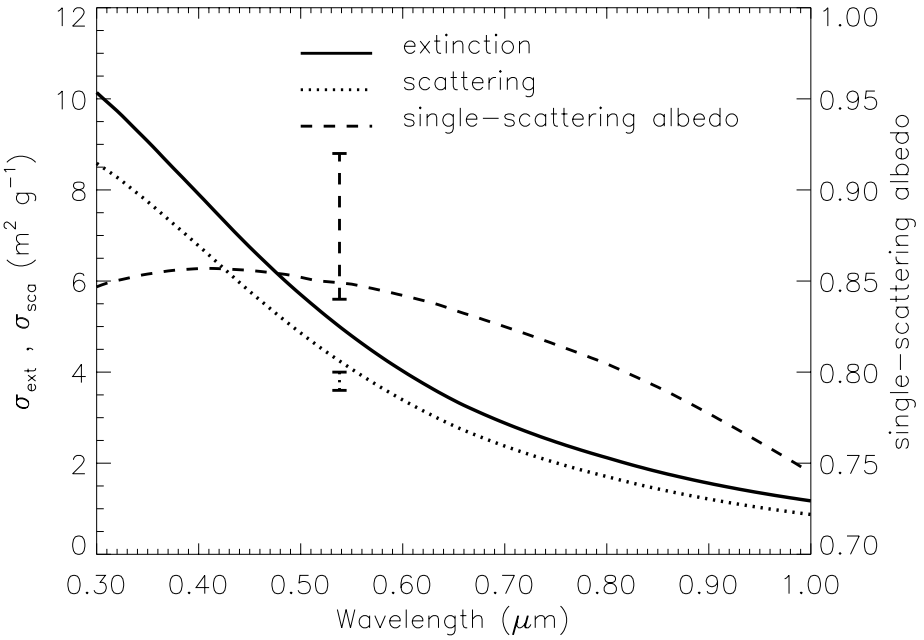

Figure 2.7: Mass extinction coefficients (left axis), mass scattering coefficients (left axis), and single-scattering albedo (right axis) calculated from the assumed size distribution and composition of the particles using Mie theory. The bars indicate the ranges of the corresponding measurements of the mass scattering coefficient and the single-scattering albedo taken from *Hobbs et al.* [1996] and *Reid* [1998].

wavelength dependent refractive index of ammonium sulfate from *Toon et al.* [1976] for OC in the remaining wavelength region is used [*Grant et al.*, 1999]. In the visible spectral range, values between 1.52 and 1.54 for the real part of the refractive index are used, the imaginary part is set to zero.

The effect of humidity on the optical properties is neglected in this study, because the relative humidity was low (<40%). Additionally, the humidification factor for biomass burning aerosol is small compared to those for industrial and urban aerosol particles [*Kotchenruther and Hobbs*, 1998].

The refractive index of the internal mixture of BC and OC was calculated using the Maxwell–Garnett mixing rule [*Bohren and Huffman*, 1983], assuming the same density for BC and OC. The resulting value of the imaginary refractive index ($n = 1.55 - 0.034i$ at 550 nm) is only slightly different from the value obtained from the volume mixing rule [*Horvath*, 1993].

The optical properties of the particles were calculated using a Mie code [*Bohren and Huffman*, 1983] based on the particle size distribution and the calculated refractive index; the results are shown in Figure 2.7 for the most relevant spectral range.

spectral interval (nm)	σ_{ext} (m^2 g^{-1})	σ_{sca} (m^2 g^{-1})	ω	g
200–690	5.80	4.93	0.85	0.64
690–1300	1.62	1.27	0.78	0.47
1300–1900	0.39	0.22	0.56	0.24
1900–2500	0.18	0.06	0.33	0.13
2500–3510	0.20	0.018	0.088	0.076
3510–4000	0.15	0.008	0.055	0.046

Table 2.1: Optical properties of the aerosol particles used in the radiative transfer calculation. Given are the mass extinction coefficient, σ_{ext}, the mass scattering coefficient, σ_{sca}, the single-scattering albedo, ω, and the asymmetry parameter, g. These values were obtained by energy-weighted averaging of the spectral high-resolved optical properties shown in Figure 2.7.

For the density of the aerosol particles, a value of 1.53 g cm^{-3} was calculated from the values given in *Martins et al.* [1996]. The calculated values of the mass scattering efficiency and the single-scattering albedo at 550 nm are 4.06 m^2 g^{-1} and 0.848, respectively. These numbers are in satisfactory agreement with the measured values of 3.8 ± 0.2 m^2 g^{-1} for the scattering efficiency and 0.84–0.92 for the single-scattering albedo [*Hobbs et al.*, 1996; *Reid*, 1998].

Use of the aerosol optical properties in the radiative transfer model requires the determination of the values for the model wavelength bands. For this purpose the optical properties with high spectral resolution are weighted by the extraterrestrial solar flux [*Wehrli*, 1985] and averaged over the wavelength intervals of the radiative transfer model. The values used are listed in Table 2.1.

Although the radiative transfer model includes the solar and the terrestrial spectrum, only the solar spectrum is taken into account in this study.

2.5 Comparison of the Aerosol Mass Concentration

In this section the model results are compared with in situ and remote sensing measurements of the smoke plume. Using the present model setup, the simulation time is limited to 100 minutes, during which the fire emissions reach the border of the model domain. Nearly all observations used for the comparison are from 1230 to 1300 LT, i.e., 85 to 115 minutes after ignition. Within this time, the general appearance of the plume did not change significantly. Nevertheless, for the comparison the modeled aerosol concentrations the observations, temporally as close as possible are

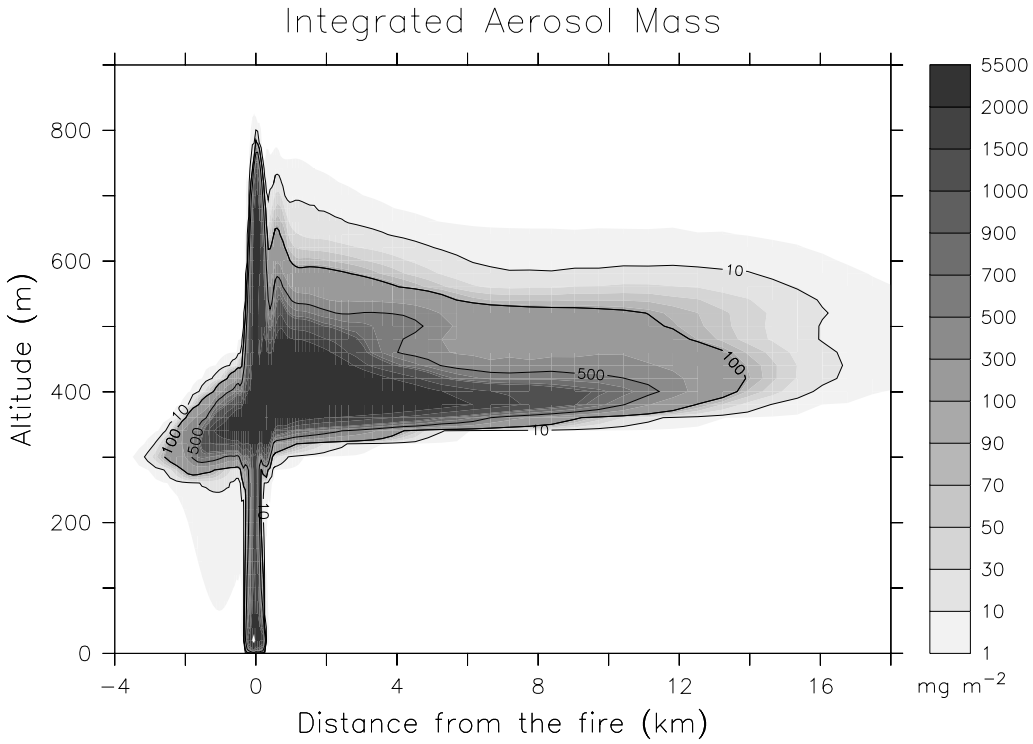

Figure 2.8: Simulated horizontally integrated aerosol mass concentrations after 100 minutes of simulation time. The unit of the contour lines is mg m^{-2}.

used.

In the first section, remote sensing observations are used to evaluate the general appearance of the simulated plume in terms of the injection height and the width of the plume. The in situ measurements of the aerosol mass concentrations in the second section are used to evaluate the simulated absolute concentrations.

A principal limitation in the comparison is that small-scale fluctuations in the plume due to the fire forcing and small scale atmospheric turbulence cannot be reproduced realistically by ATHAM. This is due to limited information on the temporal and spatial development of the fire emissions and the limited spatial resolution of the model. Nevertheless, the goal of this study was to show that the general feature of the plume can be reproduced reasonably well and that ATHAM is suitable for sensitivity studies of processes within biomass burning plumes.

Shown in Figure 2.8 is the simulated horizontally integrated aerosol mass in the plume, which reveals the general features of the simulated plume. A quantitative comparison with observations is given in the following subsections.

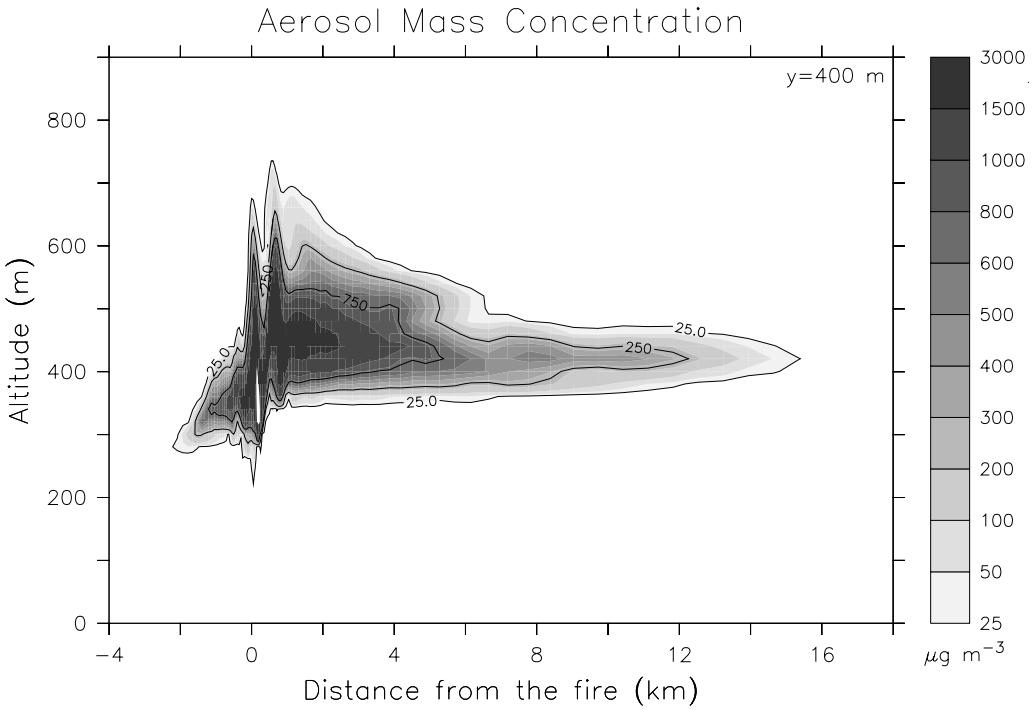

Figure 2.9: Simulated vertical cross section of the aerosol mass concentrations along the length of the plume 100 min after ignition at a distance of 400 m behind the center of the fire. The unit of the contour lines is μg m^{-3}.

2.5.1 Remote Sensing Observations

The simulated aerosol mass concentration along the plume at a distance of 400 m behind the center of the fire is shown in Figure 2.9. This result is compared with airborne LIDAR measurements [*Hobbs et al.*, 1996] in Figure 2.10. These downward-pointing measurements were taken at 1254–1259 LT ($\sim$110 min after the ignition) from the University of Washington's Convair C-131A aircraft (for a description of the aircraft and its instrumentation see *Hobbs et al.* [1991]). The observed injection height of the aerosol particles was between 250 m and 600 m, compared to 300 m to 700 m in the model simulations. This height range is determined by the atmospheric profile (in this case by the strong temperature inversion between 300 m and 600 m) and the heat emissions from the fire. Downwind of the fire the thickness of the aerosol plume derived from the LIDAR measurements is about 300 m, whereas in the model simulations the plume is only about 100 m thick. The simulated downwind aerosol concentrations are between 25 and 1000 μg m^{-3}, and thus in the same range as the measured aerosol concentrations. The maximum distance from the fire of the smoke aerosol in the measurements is about 28 km (after $\sim$110 min), whereas in the simulations the aerosol particles only traveled a distance of about 16 km (after 100 min). The observed aerosol plume exhibited a strong lofting downwind, which

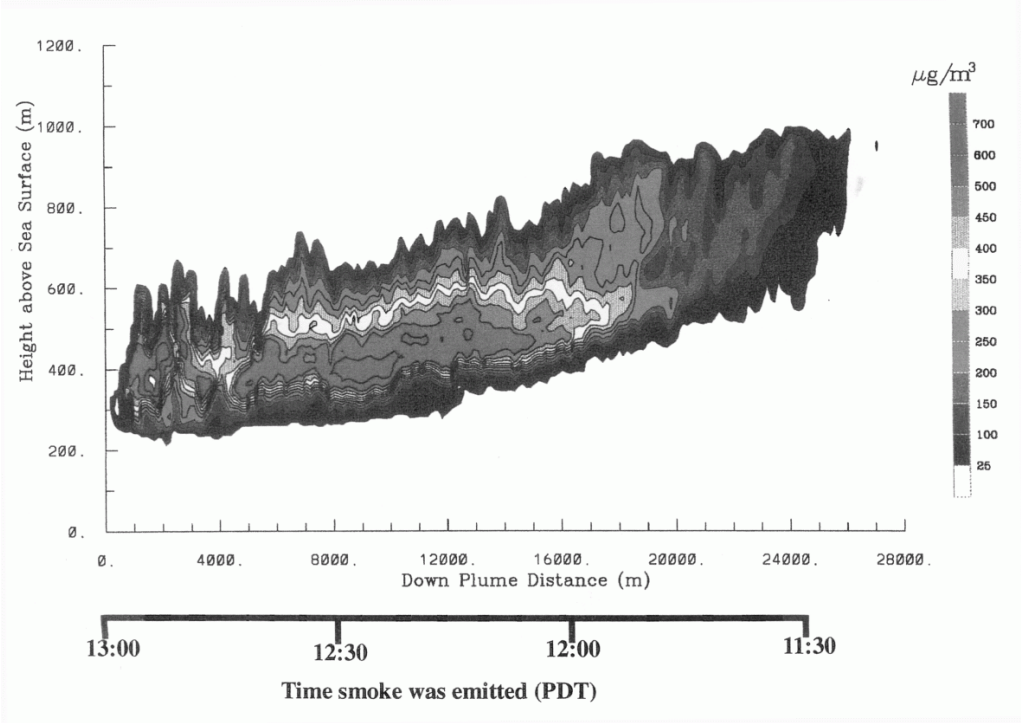

Figure 2.10: Vertical cross section of aerosol mass concentrations along the length of the smoke plume obtained with an airborne LIDAR between 1254 and 1259 LT (about 110 min after ignition). Also included is the approximate time when the smoke was emitted (calculated from the wind speed). (Reproduced from *Hobbs et al.* [1996] with the permission of the MIT Press.)

is not as intense in the simulated plume.

The simulated aerosol mass concentration across the plume at a distance of 3 km from the fire is shown in Figure 2.11. This can be compared with the LIDAR measurements obtained at 1339 LT ($\sim$2.5 h after ignition) 3 km downwind of the fire [*Hobbs et al.*, 1996] shown in Figure 2.12. The simulated aerosol plume is rather flat at the lower boundary, while the observations show a horizontal gradient of the lower plume boundary. The reasons for this discrepancy are most probably inhomogeneities in the atmospheric conditions, which were not accounted for in the model. The mass concentrations within the plume in the simulations, as well as in the observations, are around 700 μg m^{-3}. The overall width of the plume in the simulations is $\sim$5.5 km, which is in close agreement with the observations ($\sim$6 km). The peak at the 7500-m cross-plume distance in the observations also appears in the simulations (at 500 m cross-plume distance). In the model simulations, and possibly also in the observations, this peak is caused by intense vertical transport of the smoke directly above the fire where the heat-produced convection intruded into the stable atmospheric layer. Similar 'overshooting' has been observed in simulations

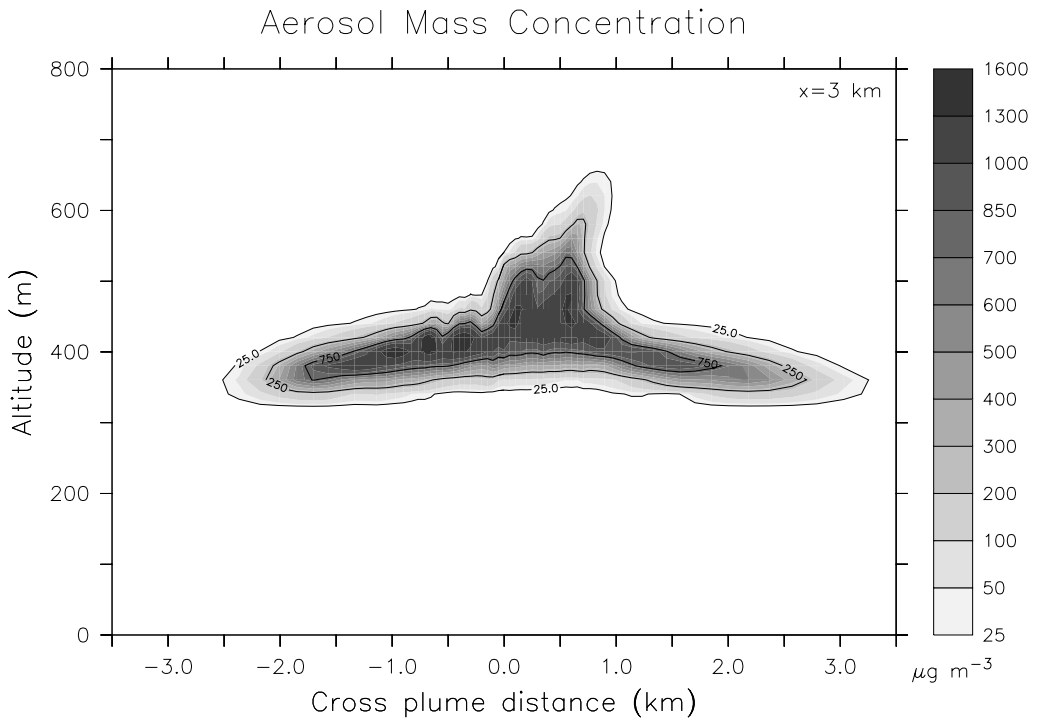

Figure 2.11: Simulated aerosol mass concentrations across the plume at a distance of 3 km from the fire 100 min after ignition. The unit of the contour lines is μg m^{-3}.

of large-scale fires [*Penner et al.*, 1986].

In general, the agreement between the model results and the LIDAR measurements is satisfactory for the purpose of this study. The injection height and the overall particle concentrations are reproduced reasonably well. One major difference is found in the maximum travel distance. This is related to a higher wind speed over the ocean, which was not included in the model simulations. Another feature that is not reproduced well by the model is the downwind lofting of the aerosol plume. This lofting may be due to the heating of the aerosol by the absorption of solar radiation, as observed in fossil fuel burns [*Radke et al.*, 1990; *Herring and Hobbs*, 1994]. In order to quantify the impact of the solar heating on the lofting of the aerosol plume in the simulation, a model simulation without accounting for the interaction of the aerosol particles with solar radiation and therefore neglecting the solar heating of the aerosol was performed. Figure 2.13 shows the impact of the solar heating on the simulated aerosol concentrations. The simulation including the aerosol heating shows a lofting of the plume downwind of the fire, although it is much smaller than in the observations. The observed lofting was therefore probably caused by changing atmospheric conditions over the ocean, (e.g., height of the boundary layer) that are not included in the simulations.

The radiance at 850 nm measured at an altitude of about 20 km aboard the ER-

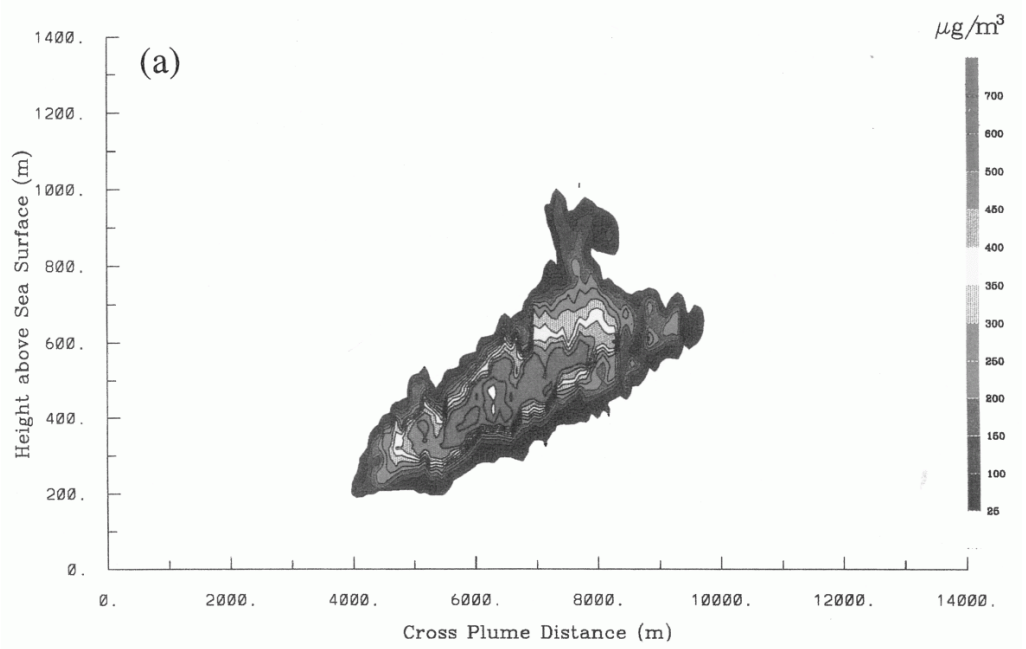

Figure 2.12: Vertical cross section across the width of the smoke plume obtained at 1339 LT (about 150 min after ignition) 3 km downwind of the fire. (Reproduced from *Hobbs et al.* [1996] with the permission of the MIT Press.)

2 aircraft with the AVIRIS instrument [*Green et al.*, 1998] at 1243 LT ($\sim$100 min after the ignition) is shown in Figure 2.14. The signature of the biomass burning plume is easily seen in the enhanced reflectivity, especially over the ocean where the surface reflectance is negligible. It can be seen that the width of the plume was about 3 km (using a reflectance of 0.01 W m^{-2} nm^{-1} sr^{-1} as an arbitrary measure of the edge of the plume). Small-scale fluctuations within the plume can be seen.

Figure 2.15 shows the simulated vertically integrated aerosol mass, which can be compared with the AVIRIS measurements. Using an arbitrary 1 mg m^{-2} isoline to define the edges of the plume, the width of the plume in the model simulation is a little larger than in the observations, but still reasonably close. The overall travel distance of the plume is larger in the observations than in the simulations. This was already observed in the comparison with the LIDAR measurements, and can be explained by an underestimation of the wind speed over the ocean. Because of the vertically changing horizontal wind speed and direction, as well as the asymmetric fire forcing, the simulations show a horizontal asymmetry. The observed small-scale fluctuations within the plume are not reproduced by the model, because they are caused by small-scale processes (e.g., fluctuations in the fire emissions, and small scale turbulent processes), that are not resolved by the model.

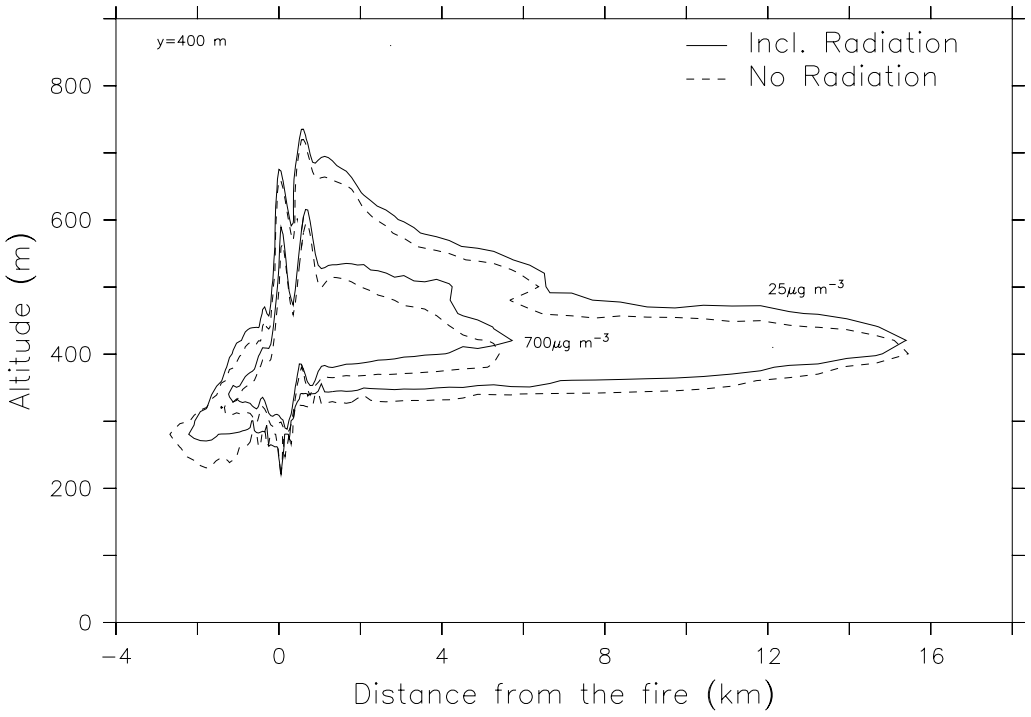

Figure 2.13: Simulated vertical aerosol mass concentrations along the length of the plume at a distance of 400 m behind the center of the fire 100 min after ignition, including and neglecting the solar heating of the aerosol particles.

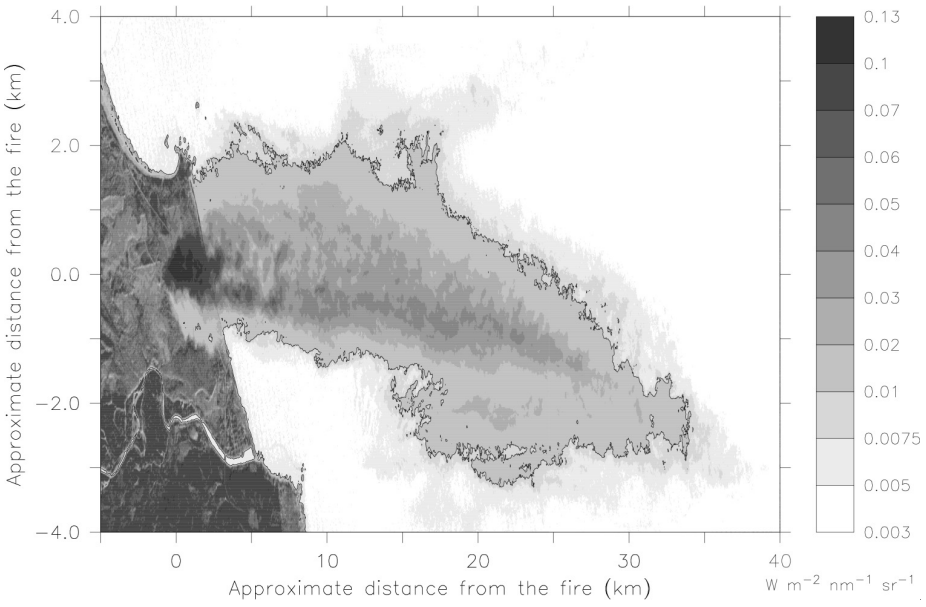

Figure 2.14: Measured radiances at 850 nm, measured on board the ER-2 aircraft using the AVIRIS instrument between 1243 and 1248 LT (about 100 min after ignition). Calibrated AVIRIS data were obtained from Dr. Robert Green, JPL.

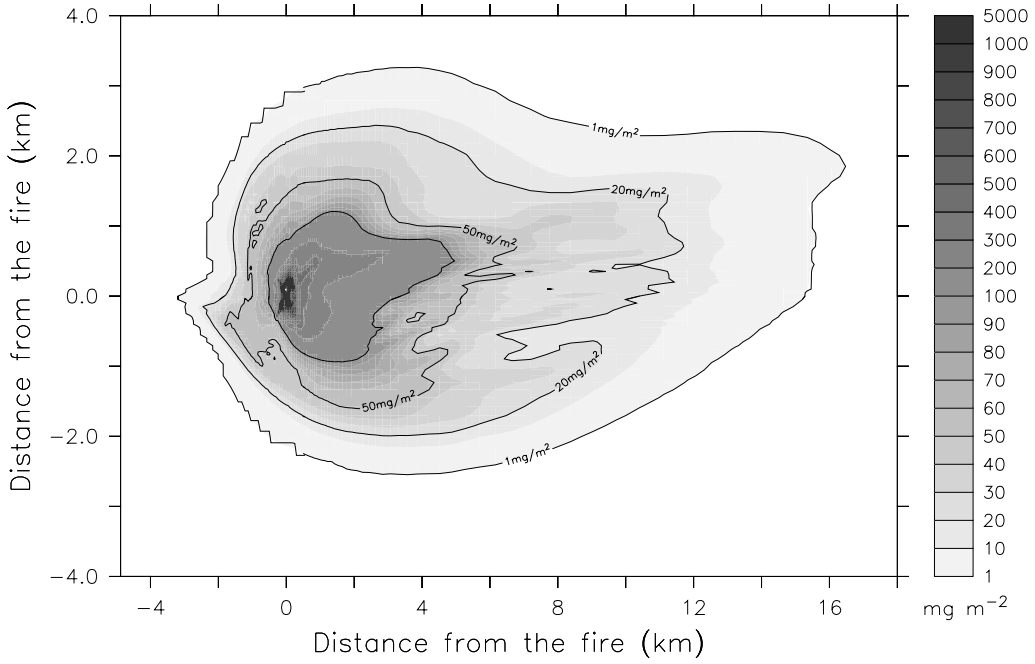

Figure 2.15: Simulated vertically integrated aerosol mass concentrations 100 min after ignition.

2.5.2 In situ Measurements

In this section, in situ measurements made aboard the University of Washington's Convair C-131A research aircraft are used to evaluate the model results. The aircraft flew several times along and across the plume. Aerosol samples were obtained, as well as measurements of the optical properties of the smoke. Unfortunately, there were no direct high-resolution measurements of aerosol mass concentrations to compare with the model results. However, aerosol mass concentrations were determined from filter samples taken during three encounters with the plume from the Quinault fire and two other fires during the SCAR-C experiment [*Martins et al.*, 1996]. Using the filter data from all three fires during SCAR-C and simultaneous measurements of the light scattering coefficient at 538 nm, the dry aerosol mass scattering efficiency was determined to be 3.8 ± 0.2 m^2 g^{-1} [*Hobbs et al.*, 1996; *Reid*, 1998]. By multiplying the high-resolution measurements of the scattering coefficient by the mass scattering efficiency, the aerosol mass concentrations can be approximated with high temporal and spatial resolution.

Figure 2.16 shows the measured aerosol mass concentration along the plume and the model results 90 minutes after ignition. The measurements were performed at 1236 LT ($\sim$90 min after ignition). Particle mass concentrations exceeding 2500 μg m^{-3} were observed near the fire; these are consistent with the values of 1820 μg m^{-3} and 2880 μg m^{-3} given by *Martins et al.* [1996] for the Quinault fire. Downwind

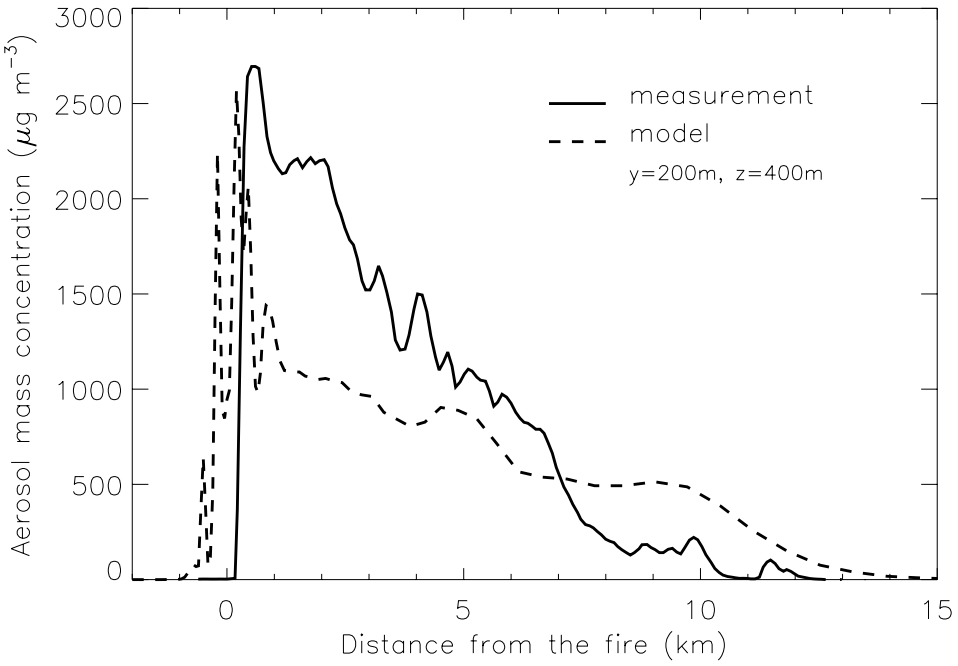

Figure 2.16: Measured and simulated aerosol mass concentrations along the plume from the Quinault fire. The measurements were performed at 1236 LT (about 90 min after ignition) at altitudes between 350 and 500 m. The model results are taken 90 min after ignition along the line at $y = 200$ m, $z = 400$ m.

of the fire, the mass concentrations decreased gradually with distance from the fire, reaching the background concentration at 13 km downwind. The model also shows the highest particle mass concentrations, which are similar to the observed values but with higher variability, above the fire. However, the mass concentrations from the model are significantly lower (by up to a factor of 2) than the measurements up to 8 km downwind, and the model results are greater than the measurements between 8 km and 15 km downwind.

The most plausible reason for the differences between the model results and the measurements is an underestimation of the fire emissions at the beginning phase of the fire by the EPM model. Although the EPM model predicts a strong increase in aerosol emissions after 60 minutes (see Figure 2.4), the visible observations showed a strong increase in fire emissions already around 40 min after ignition [*Hobbs et al.*, 1996]. Additionally, the emission factors used in the EPM model might be too low for this scenario. The difference between the observed and simulated aerosol mass concentrations beyond 8 km is probably due to the fact that the aircraft did not fly within the center of the plume at these distances.

Shown in Figure 2.17 are the measured and simulated aerosol mass concentra-

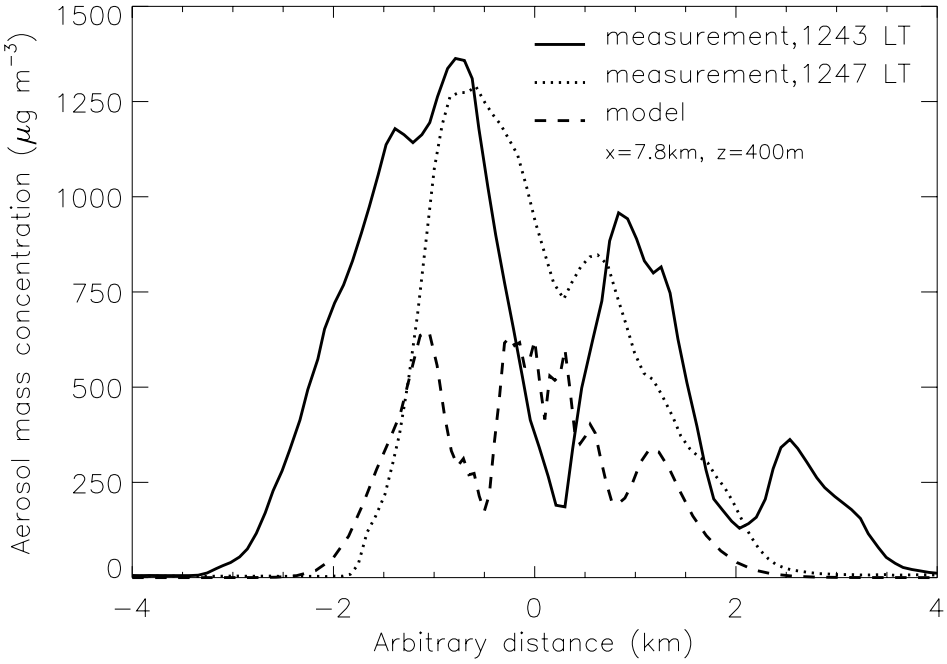

Figure 2.17: Measured and simulated aerosol mass concentrations across the plume from the Quinault fire. Shown are mass concentrations measured during two transects of the plume (perpendicular to the main axis) at 1243 LT and 1247 LT (about 100 min after ignition) between 8.5 and 10.5 km distance from the fire at altitudes between 430 and 530 m. The model results are taken 100 min after ignition along the line at $x = 7.8$ km, $z = 400$ m.

tions perpendicular to the main plume axis. The measurements were obtained at 1243 and 1247 LT ($\sim$100 min after ignition) about 8 km downwind of the fire. The two measured aerosol concentrations differ in their horizontal extent and in their shape even though they were obtained close to each other (in space and time). This reflects the strong inhomogeneities within the plume, which are not reproduced by the model simulations. As mentioned previously, the measured concentrations are nearly twice the simulated concentrations. Nevertheless, the simulated aerosol concentrations show similarities with the measurements. The simulated aerosol concentrations in the plume have three local maxima, which are also present in the measurements at 1243 LT. The width (4 km) of the simulated plume is very close to the measured value during the aircraft crossing at 1247 LT.

It is interesting to compare the measured aerosol mass concentrations across and along the plume. At the distance of 8 km, the concentrations along the plume in Figure 2.16 are considerably lower than the maximum value shown in Figure 2.17. This supports the hypothesis that during the end of the plume transect at 1236 LT

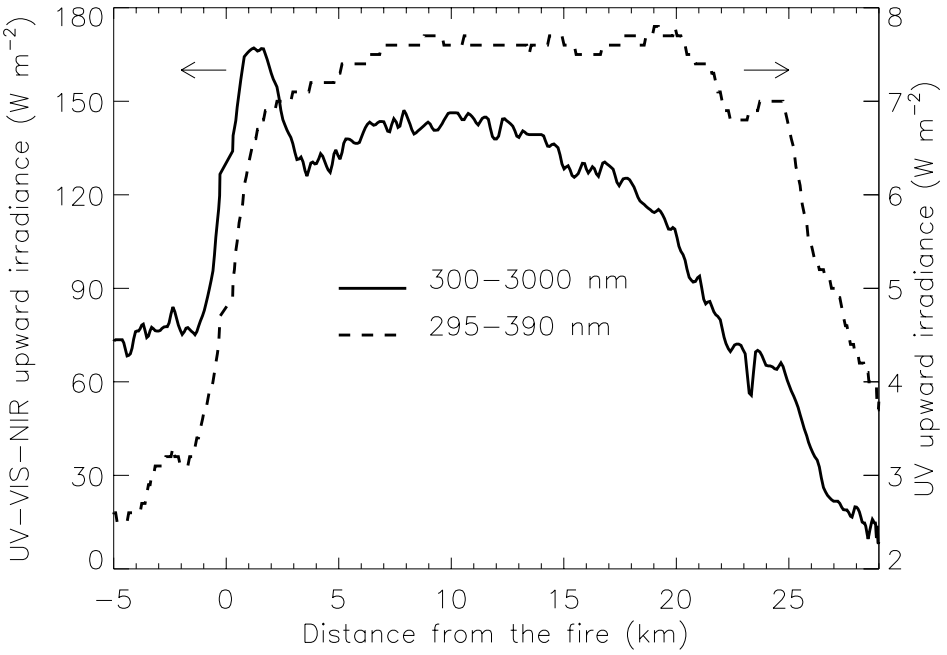

Figure 2.18: Measured upward irradiance in the wavelength intervals 300 to 3000 nm (UV–VIS–NIR, solid line, left scale) and 295 to 390 nm (UV, dashed line, right scale) above the plume. These measurements were obtained between 1254 and 1259 LT at an altitude of about 1350 m simultaneously with the LIDAR measurements shown in Figure 2.10.

the aircraft did not fly along the main axis of the plume.

Overall, ATHAM is able to predict the observed aerosol mass concentration and its variability along and across the plume reasonably well. Together with the results from Section 2.5.1, it can be concluded that ATHAM reproduced the general features within the biomass burning plume and thus can be used for further sensitivity studies of the processes within the plume.

2.6 Comparison of the Upward Irradiance

In the following, a comparison of the measured and simulated upward radiation above the smoke plume is presented.

Aboard the University of Washington's Convair C-131A aircraft were broad-band up- and downward looking ultra-violet (UV) (295 to 390 nm) and ultra-violet–visible–near-infrared (UV–VIS–NIR) (300 to 3000 nm) pyranometers. Shown in Figure 2.18 are the measured upward irradiance in the UV–VIS–NIR and the UV for a flight transect above the plume of the Quinault fire from 1254 to 1259 LT ($\sim$110 min after ignition) at an altitude of about 1350 m. There is a strong increase

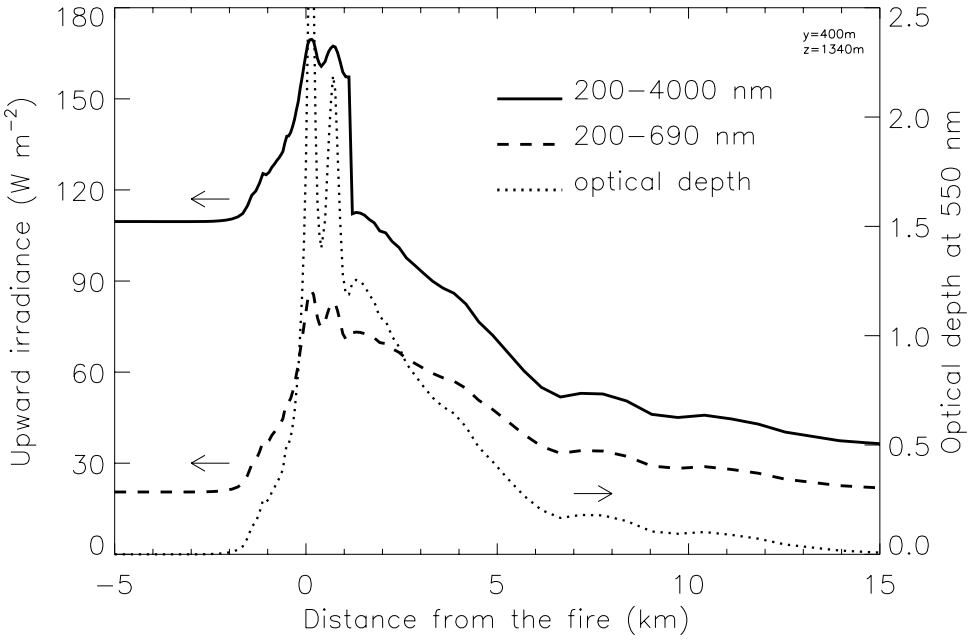

Figure 2.19: Simulated upward irradiance in the wavelength intervals 200 to 4000 nm (solid line) and 200 to 700 nm (dashed line) above the plume at an altitude of 1340 m and a horizontal distance from the center of the fire of 400 m. The solar zenith angle was set to 47°. Also included is the simulated optical depth at 550 nm (dotted line).

in the upward irradiance over the fire in both wavelength regions, whereas at about 2 km downwind the UV–VIS–NIR flux shows a decrease that is not seen in the UV irradiance. Both irradiances stay more or less constant over most of the distance along the plume, until they decrease to background values. The background value of UV–VIS–NIR irradiance at the end of the transect ($\sim$10 W m^{-2}) is significantly lower than at the start of the transect ($\sim$75 W m^{-2}), whereas the change in the background values in the UV is not significant.

To simulate the upward irradiance, only the aerosol from the fire is taken into account and the aerosol mass concentrations simulated after 100 minutes of fire emissions were used. The solar zenith angle (SZA) was set to 47°, corresponding to the time and place of the observations in Figure 2.18. The simulations were performed with the PIFM model included in ATHAM and are therefore restricted to the available spectral bands (see Table 2.1). They are not identical with the measured spectral bands, but for the purpose of this study the first spectral band of the radiative transfer model (200 to 690 nm) (UV–VIS) can be used for comparison with the UV measurements. The full spectral range of the simulations (UV–VIS–NIR) (200 to 4000 nm) is used for comparison with the UV–VIS–NIR measurements.

The wavelength regions 200 to 300 nm and 3000 to 4000 nm do not contribute significantly to the solar energy near the surface.

Figure 2.19 shows the model results in the UV–VIS (200−690 nm) and UV–VIS–NIR (200−4000 nm) wavelength region of the upward irradiance together with the aerosol optical depth at 550 nm. Over land, the simulated values outside of the plume (left sides of Figures 2.18 and 2.19) are significantly higher than the measurements (110 W m^{-2} compared to 75 W m^{-2} in the UV–VIS–NIR). A comparison of the UV–VIS–NIR downward irradiance shows that this was also overestimated by the model (measurement, 712 W m^{-2}; model, 757 W m^{-2}). This underestimation of extinction of incoming solar radiation in the model simulations may be explained by the neglect of aerosol extinction in the absence of smoke. Additional uncertainty in the simulated upward radiation arises from limited information on the surface albedo. Over the ocean, the simulated upward irradiance in the UV–VIS–NIR is also overestimated (35 W m^{-2} compared to 10 W m^{-2}). Further comparisons below focus on the change in the upward irradiance, rather than their absolute values.

As shown before, the total distance traveled by the smoke in a given time is underestimated by the model. This is also seen in the comparison of the upward irradiance. In the simulations as well as in the measurements, the upward irradiance in the UV–VIS–NIR over land is much higher than over the ocean (right sides of the Figures 2.18 and 2.19), whereas this feature is not significant in the UV and UV–VIS. This behavior is explained by the wavelength dependence of the surface albedo over land, which strongly increases for wavelengths longer than 700 nm.

As seen in the measurements, the simulations also show a strong increase in the upward irradiance above the plume. Also the sharp decrease in the UV–VIS–NIR irradiance is observed at about 2 km downwind, but the UV–VIS radiation does not change. In the model simulations this decrease is due to the changing surface albedo for the UV–VIS–NIR in passing from land to ocean (albedo changes from 14.8% to 4.1%). This effect is not significant in the UV–VIS (albedo changes from 4.0% to 4.3%). This suggests that the decrease in the observed UV–VIS–NIR irradiance shown in Figure 2.18 is due to the change in the surface albedo, although it is more gradual. This hypothesis is supported by the fact that there was no observed decrease in the UV irradiance.

Downwind of the plume, the measurements show a constant irradiance in both the UV–VIS and UV–VIS–NIR range, but the simulated irradiance decrease. The reason for this different behavior is the decrease in the aerosol optical depth in the model downwind the plume, which is not as pronounced in the observations [*Gassó and Hegg*, 1998]. The low variability in the observed irradiance might be due to the absorbing properties of the aerosol which lead to a saturation of the upward irradiance at high optical depth.

Overall the upward irradiance above the plume are underestimated by the model, although the background values are too high. This might arise from too low aerosol concentrations or too low backscattering of the aerosol or most probably a combination of both. As shown before, the simulated aerosol mass concentrations are too low. Additional uncertainties arise from the aerosol properties, e.g., size distribution, composition, state of mixing, and the neglect of humidity effects. The use of the refractive index of soot for the measured BC content of the aerosol may lead to an overestimation of the aerosol absorption. The black carbon determined by thermal or optical techniques from biomass burning aerosol is not necessarily identical with soot [*Novakov and Corrigan*, 1995; *Mayol-Bracero et al.*, 2001]. However, as long as no further data is available, the use of the refractive index of soot is the only appropriate way to account for BC. Additionally, the assumed internal mixing of the aerosol as well as the use of the same density for OC and BC lead to high aerosol absorption.

A underestimation of the aerosol optical depth from biomass burning aerosol is also found on global scale especially in the source regions [*Tegen et al.*, 1997]. Together with the results presented here, this points to uncertainties in the direct aerosol emission from biomass burning applied in global models. Further studies using a combination of small-scale and regional to global models may help to reduce this discrepancy.

2.7 Comparison of the Zenith Radiance

As discussed in section 2.6, the comparison between the observed and the simulated upward irradiance yields an underestimation of the model. Possible reasons are the underestimation of the aerosol optical thickness, which is taken from the ATHAM simulation, or the use of non appropriate optical properties of the aerosol, which are derived from in situ measurements. The previous analysis is extended in this section. For this purpose, measurements of the upwelling radiance from the AVIRIS instrument are analyzed. These measurements, shown in Figure 2.14 for a wavelength of 850 nm, were performed 10 min before the measurements of the irradiance shown in Figure 2.18.

The AVIRIS instrument measures the upwelling radiance at 224 spectral channels at 10 nm resolution across the wavelength region from 400 nm to 2500 nm [*Green et al.*, 1998]. The field of view of AVIRIS is 30°, perpendicular to the flight track with an instantaneous field of view of 1 mrad. The instrument scans this field of view at a rate of 12 Hz. At the flight altitude of the ER-2 of 20 km, this transfers to a field of view of 11 km and a spatial resolution of $\sim$20$\times$20 m. Because the plume is roughly 4 km wide, the measurements were made $\pm$10° from nadir.

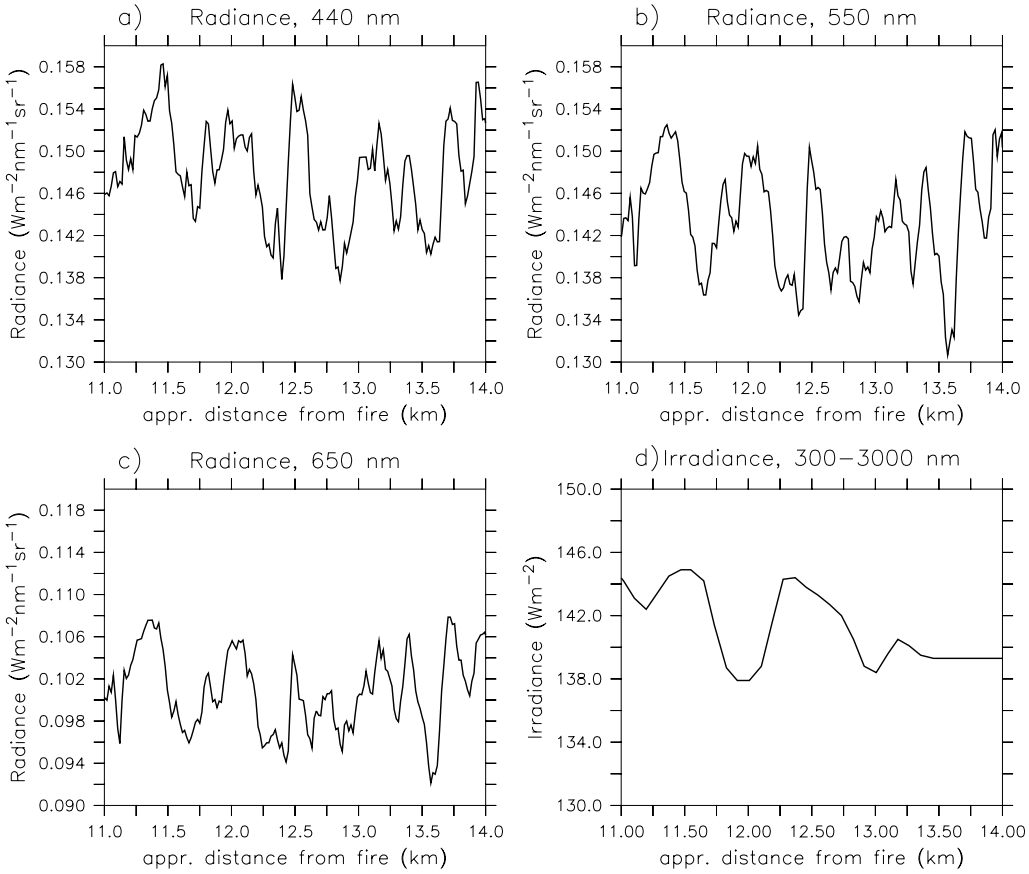

Figure 2.20: a–c) Measured radiance from the AVIRIS instrument at an altitude of 20 km above the plume at (a) 440 nm, (b) 550 nm, and (c) 650 nm. Measurements were acquired at 1245 LT. Shown are the maximum values of the radiance at each cross track scan. Calibrated AVIRIS data were obtained from Dr. Robert Green, JPL. (d) Measured upward irradiance between 300 and 3000 nm performed at 1257 LT at an altitude of about 1350 m.

Figure 2.20a–c shows the measured radiance at 440 nm, 550 nm, and 650 nm from the AVIRIS instrument as a function of distance from the fire. The maximum radiance of each cross track scan is shown. The dependence of the radiance on the viewing angle is much less than that on the aerosol optical depth. Therefore, the presented radiance corresponds to the maximum aerosol optical depth at every cross track scan. Figure 2.20d presents the measured upward irradiance above the plume at an altitude of about 1350 m performed ∼10 min after the AVIRIS measurements.

In order to simulate the measurements of the radiance with a radiative transfer model, the 2-stream model PIFM used in the previous sections cannot be used, because 2-stream models can only simulate the irradiance. For the simulation of the radiance, the public-available STREAMER model is used [*Key*, 1999]. This one-dimensional radiative transfer model calculates the atmospheric radiation field based on the discrete ordinate method [*Stamnes et al.*, 1988], and includes gas

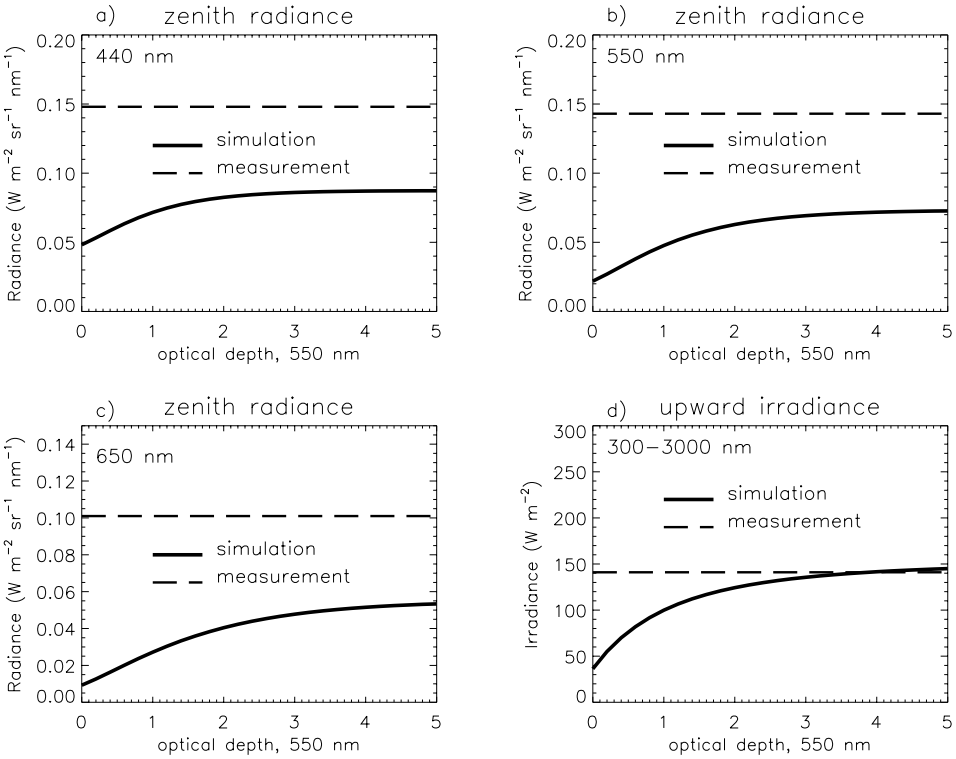

Figure 2.21: Simulated zenith radiance for (a) 440 nm, (b) 550 nm, and (c) 650 nm and (d) simulated UV–VIS–NIR irradiance as a function of aerosol optical depth at 550 nm using the aerosol model presented in section 2.4.4. In each plot, the corresponding observations are indicated.

absorption and scattering as well as the interaction of aerosol particles and cloud droplets with radiation. The phase function of the aerosol is parameterized by the expansion of the Mie phase function into Legendre polynoms [Olivier Boucher, pers. comm.]. Especially for the simulation of radiances, the use of the Henyey–Greenstein phase function for the aerosol introduces additional errors [*Boucher*, 1998].

In the following, the simulated zenith radiances at an altitude of 20 km are compared with the horizontal average of the maximum radiances measured from the AVIRIS instrument (Figure 2.20). The ocean surface albedo was determined by reproducing aerosol free radiance measurements with the albedo as a free parameter. A value of around 1% was derived for all wavelengths. The albedo is slightly lower than the one used in section 2.6 for the simulation of the irradiance, because only the surface reflection into the zenith direction is considered.

In the radiative transfer simulations, aerosol particles are homogeneously distributed between the surface and 1 km altitude. The results are relatively insensitive to the location of the aerosol. The aerosol optical properties shown in Figure 2.7 derived from in situ measurements are used. Several calculations were performed

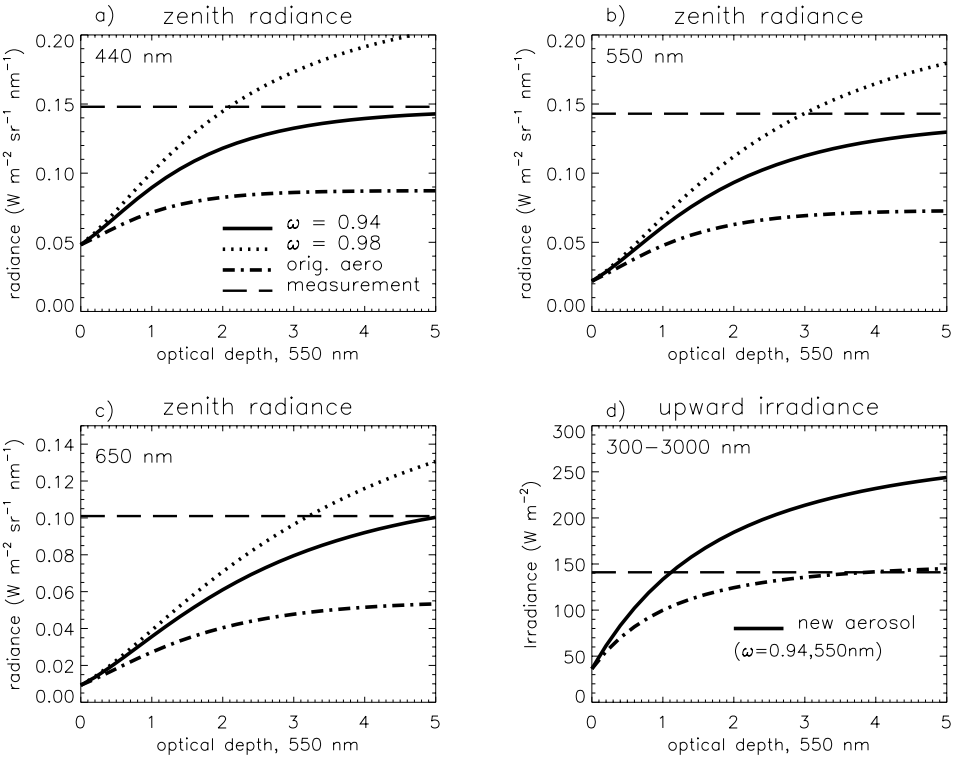

Figure 2.22: Simulated zenith radiance for (a) 440 nm, (b) 550 nm, and (c) 650 nm using the original aerosol and two aerosol models with $\omega = 0.98$ and $\omega = 0.94$ as a function of aerosol optical depth at 550 nm. (d) Simulated UV–VIS–NIR upward irradiance using the original aerosol and a new aerosol model with $\omega = 0.94$ for $\lambda = 550$ nm as a function of aerosol optical depth at 550 nm. In each plot, the corresponding observations are indicated.

with increasing aerosol optical depth. Remote sensing observations indicate aerosol optical depths at 550 nm between 2 and 3 [*Tanré et al.*, 1997; *Gassó and Hegg*, 1998].

In Figure 2.21, (a–c) the simulated zenith radiances at 3 wavelengths and (d) the simulated UV–VIS–NIR upward irradiance above the plume as a function of aerosol optical depth are shown. The corresponding observations are also indicated as dotted lines. In general, such an analysis can be used to retrieve the aerosol optical depth from radiance measurements if the aerosol optical properties are known. However, in this case the measured radiance cannot be reproduced by the simulations, because the simulated radiance as a function of aerosol optical depth saturates below the measurements. In addition to the radiance, the upward UV–VIS–NIR irradiance at an altitude of 1.5 km was simulated with the STREAMER model and is shown in Figure 2.21d. The simulated irradiance reproduces the measured value of around 140 W m^{-2} at aerosol optical depths larger than 3. The results shown in Figure 2.21 point to a discrepancy between measurements of the radiance and the irradiance

that will be further investigated.

For this purpose, the optical parameters of the aerosol are changed in such a way that the observed radiance is reproduced by the model simulations. Several aerosol parameters impact the zenith radiance, e.g., the aerosol size distribution and the chemical composition of the aerosol. However, in this case, the most sensitive optical parameter for the simulated zenith radiances is the aerosol absorption. Therefore, in the following investigation, only the aerosol absorption, described by the single-scattering albedo ω, is varied. Variation of other parameters, e.g., the size distribution, have a much smaller effect on the zenith radiance.

Radiative transfer simulations were performed with different wavelength independent values for ω, ranging from 0.85 to 1.0 in steps of 0.01. The total extinction as well as the phase function of the aerosol were kept constant in all simulations. Based on the comparison between the simulated and measured zenith radiances, a new single scattering albedo of the aerosol is determined that is consistent with the measurements of the radiance.

Figure 2.22 presents (a–c) the simulated zenith radiance at 3 wavelengths and (d) the simulated upward irradiance calculated with 3 different absorbing properties of the aerosol. The strong impact of the aerosol absorption on the zenith radiance is easily seen. The use of a single-scattering albedo of 0.98 leads to significant higher values of the simulated zenith radiance compared to a single-scattering albedo of 0.94. In order to reproduce the observed radiance at a realistic aerosol optical depth, a value for the single-scattering albedo between 0.94 and 0.98 seems to be appropriate. If a value below 0.94 for the single-scattering albedo is used, the observed radiances cannot be reproduced by the model simulations. The value of ω = 0.94 can be considered as the lower limit of the single-scattering albedo in the visible wavelength region derived from the radiance measurements.

For the calculation of the UV–VIS–NIR irradiance, a wavelength-dependent single-scattering albedo has to be used. In order to keep the wavelength dependency of ω from the original aerosol, the new single-scattering albedo is calculated by reducing the absorption, i.e., $1-\omega$, of the original aerosol by 60% yielding a single-scattering albedo of 0.94 at 550 nm corresponding to the lower limit derived from the analysis of the radiance. The simulated irradiance using this new aerosol model is shown in Figure 2.22d. The reduced aerosol absorption leads to an overestimation of the upward irradiance. The reasons for this overestimation are probably the finite dimensions of the plume and the use of a 1D radiative transfer model for the simulation of the upward irradiance. This effect will be further investigated in chapter 3. The fact that the flight track did not follow the maximum aerosol optical depth might also contribute to this discrepancy.

The comparison between the simulated and measured upwelling radiance above

the plume from the Quinault fire indicates that the aerosol absorption derived from in situ measurements is higher than that derived from remote sensing observations. A similar conclusion was derived from remote sensing and in situ measurements also for biomass burning aerosol [*Remer et al.*, 1998; *Chu et al.*, 1998] as well as for dust particles [*Kaufman et al.*, 2001]. There are several possible reasons for the overestimation of the aerosol absorption in the present study as already discussed in section 2.6. These include the neglect of humidity effects, the use of the same density for OC and BC, the use of the refractive index of soot for BC as well as the assumption of spherical, internal mixed particles. In situ measurements of the single-scattering albedo from the Quinault fire range from 0.84 to 0.92 [*Hobbs et al.*, 1996]. These values are also below the lower limit derived from the remote observations. This analysis underlines the large uncertainty that exists in the measurement and calculation of absorption by aerosol particles.

2.8 Conclusions

For the first time, a model simulation of the atmospheric evolution of a biomass burning plume and a comparison with measurements were presented. The plume model ATHAM was used to simulate the atmospheric transport of aerosol particles emitted from a prescribed fire based on information on the fire emissions and atmospheric conditions. The simulated aerosol mass concentrations were compared with remote sensing and in situ measurements of the plume. The injection height and the general appearance of the plume are reproduced with good accuracy by the model. The absolute value of the aerosol mass concentration shows an underestimation roughly by a factor of 2, probably due to an underestimation of the fire emissions. Other differences were attributed to the simplified description of the meteorological situation and small scale features that cannot be resolved in this kind of model. Modeled and measured results for the upward solar irradiance above the plume were compared. The impact of the changing surface albedo on the upward radiation is clearly seen in both the model simulations and the measurements. Using the ATHAM-generated spatial aerosol distribution, the upward solar irradiance is underestimated by the model, which is attributed to the underestimation of the aerosol concentration. Using variable aerosol optical depths, the analysis of the upwelling radiance above the plume yields a lower limit of $\omega = 0.94$ for the single-scattering albedo in the visible wavelength region. This value of ω leads to an overestimation of the upward irradiance at realistic aerosol optical depths probably because of three-dimensional radiative effects due to the finite dimensions of the plume. This issue will be addressed in Chapter 3.

Chapter 3

Three-dimensional Solar Radiation Effects in a Biomass Burning Plume[1]

Abstract. Three-dimensional (3D) solar radiative transfer models describe atmospheric radiative transfer more accurately than the commonly used one-dimensional (1D) radiative transfer models that assume horizontal homogeneity of the atmosphere. Here, results of 3D radiative transfer simulations for a biomass burning plume are presented and compared with simulations employing the independent pixel approximation (IPA). The spatial distribution of the aerosol particles is derived from a 3D atmospheric transport simulation. The impact of 3D radiative effects on the actinic flux, F, within the plume center and on the upward irradiance, E_{up}, above the plume are investigated. The differences in the actinic flux between results from the 3D and the IPA simulations are considerable, ranging from -40% to more than $+200\%$, depending on the absorbing properties of the aerosol. The reason for this discrepancy is the neglect of horizontal photon transport in the 1D simulation. These large 3D effects on the actinic flux have the potential to influence the photochemistry within the plume significantly. The 3D model simulates a decreasing upward irradiance with increasing vertical distance from the plume, because of the decrease of the solid angle under which the plume is seen. The IPA simulation overestimates E_{up}, because the changing solid angle of the plume cannot be considered within this approximation. This vertical decrease of E_{up} has to be taken into account, when interpreting irradiance measurements over finite clouds or aerosol plumes.

[1]This chapter is submitted for publication in the *Journal of Geophysical Research,* 2001, with B. Früh, O. Boucher, T. Trautmann, and M. O. Andreae as coauthors.

3.1 Introduction

Radiative transfer in the atmosphere is a three-dimensional phenomenon. Nevertheless, commonly used radiative transfer models only consider vertical photon transfer and assume that the atmosphere is homogeneous in the horizontal directions. This assumption of one-dimensional (1D) radiative transfer is a good approximation for clear-sky conditions over a uniform surface, but is generally not fulfilled if aerosol plumes or broken clouds are present or if the surface does not have uniform properties.

In the past, the three-dimensional distributions of cloud droplets and aerosol particles were often not available for atmospheric studies, since the resolution of global circulation models and satellite instruments was too coarse. High resolution in situ measurements are rare and can only yield very limited information about all spatial dimensions. Recently, significant improvements of the resolution of atmospheric models and remote sensing instruments were achieved. Large-eddy simulation (LES) models have become a valuable modeling tool [*Duynkerke et al.*, 1999; *Vilà-Guerau de Arellano and Cuijper*, 2000; *Stevens et al.*, 2001] along with convective cloud and plume models [*Oberhuber et al.*, 1998; *Lu et al.*, 2000; *Skamarock et al.*, 2000]. Meanwhile, modern satellite and airborne remote sensing instruments are able to observe the atmosphere with a horizontal resolution of some hundreds of meters in the case of spaceborne instruments (such as the moderate resolution imaging spectroradiometer (MODIS), the medium resolution imaging spectrometer instrument (MERIS), and the earth system science pathfinder 3 (ESSP3) and a few tens of meters in the case of airborne instruments (such as the MODIS airborne simulator (MAS) and the airborne visible infrared imaging spectrometer (AVIRIS)). Thus, the possibility and need of detailed studies on the effects of horizontally inhomogeneously distributed particles on the atmospheric radiation field arise. For these investigations, three-dimensional (3D) radiative transfer models have to be used.

The modification of the backscattered radiation field due to cloud inhomogeneities has drawn special attention, because of the nonlinearity between cloud optical depth and cloud albedo. The mean albedo of a cloud with horizontally varying optical depth is less than the albedo of a uniform cloud with the same mean optical depth. This effect is called the "plane-parallel albedo bias" (PPA) [*Cahalan et al.*, 1994]. This needs to be taken into account in global circulation models, which simulate only the averaged cloud optical depth within a grid box.

Additionally, it was suggested that cloud inhomogeneities are at least in part responsible for the discrepancy between modeled and observed absorption within clouds [*Cess et al.*, 1995; *Ramanathan et al.*, 1995]. The effect of cloud inhomogeneities on atmospheric absorption is a complex interplay between gaseous absorption, cloud droplet absorption, and solar zenith angle. There have been studies on

the effect of cloud inhomogeneities on atmospheric absorption, indicating that they are, at least in part, responsible for the enhanced absorption that is observed [*Borde and Isaka*, 1996; *O'Hirok and Gautier*, 1998a,b; *Cairns et al.*, 2000].

A similar underestimation of atmospheric absorption is found when model results are compared with measurements in the cloud-free atmosphere in the presence of aerosol particles [*Kato et al.*, 1997; *Wild*, 1999; *Halthore and Schwartz*, 2000]. However, the possible effects of inhomogeneities in the spatial distribution of the aerosol on the atmospheric radiation field have not been addressed yet. So far, the spatial distribution of the aerosol is assumed to be horizontally homogeneous on the scale of some tens of kilometers and the IPA can be employed in radiative transfer simulations. Nevertheless, this assumption is not valid for an individual plume (or a set of individual plumes, e.g., from vegetation fires). To the authors knowledge, the only investigation so far of three-dimensional radiation effects in the presence of aerosol particles was recently published by *Lyapustin and Kaufman* [2001]. They used a 3D radiative transfer model to investigate the role of the spatial heterogeneity of land surfaces on the remote sensing of the aerosol. However, only horizontal homogeneous aerosol distributions were used in the simulations.

Most of the previous studies of three-dimensional radiative effects focused on the reflected or transmitted irradiance. Despite the potential importance of the actinic flux for atmospheric chemistry (photolysis frequencies) and dynamics (heating rates), the impact of 3D atmospheric radiative transfer on the actinic flux within inhomogeneous cloud fields has been studied only recently [*Los et al.*, 1997; *Trautmann et al.*, 1999; *Vogelmann et al.*, 2001].

3.1.1 Three-dimensional Radiation Effects and Model Types

Two different types of heterogeneity effects can be distinguished [*Várnai and Davis*, 1999; *Benner and Evans*, 2001]: the *one-dimensional heterogeneity effect* and the *horizontal transport effect*. The one-dimensional heterogeneity effect describes the nonlinearity between cloud optical depth and albedo (also called PPA, as mentioned before) [*Cahalan et al.*, 1994]. The horizontal transport effect results from the horizontal transfer of direct or scattered radiation between adjacent columns. Photons within a cloud or an aerosol plume can leak out through the sides due to scattering processes or enter the cloud or aerosol plume from the side due to direct illumination or scattering.

The one-dimensional heterogeneity effect can be addressed with 1D models based on the independent pixel approximation (IPA) [*Cahalan et al.*, 1994]. In the IPA, 1D radiative transfer simulations are performed independently in every column of the model domain. Horizontal transport of photons between adjacent columns is not taken into account. A first attempt to improve the IPA is the tilted IPA (TIPA) that

takes the horizontal transfer of the direct solar radiation into account by orientating the vertical columns along the slant path of the incoming solar photons [*Várnai and Davis*, 1999]. However, side leakage and radiative smoothing [*Marshak et al.*, 1995] can only be considered in 3D radiative transfer simulations.

The most common type of 3D radiative transfer models use the Monte Carlo technique [e.g., *Marchuk et al.*, 1980; *Podgorny et al.*, 1998; *O'Hirok and Gautier*, 1998a]. These models simulate the transfer and fate of a single photon within the model domain. By repeating this calculation for a large number of photons, radiative quantities are derived with good accuracy. An alternative approach is the explicit calculation of the 3D radiation field with a numerical solution method as commonly performed in 1D radiative transfer simulations. An overview about explicit 3D radiative transfer models is given by *Gabriel et al.* [1993]. The advantage of explicit methods is the calculation of the complete atmospheric radiation field at one time. This allows the determination of several radiative quantities without any extra effort.

In the present work, the spherical harmonics discrete ordinate method (SHDOM) [*Evans*, 1998], which belongs to the latter group of models, is used. SHDOM agrees well with Monte Carlo models for the zenith upwelling radiance, the up- and downwelling irradiance [*Evans*, 1998] and the actinic flux [*Trautmann et al.*, 1999] for inhomogeneous cloud fields. It has been used in several studies of 3D radiation effects, including the effect of inhomogeneous clouds on atmospheric UV transmittance [*Meerkötter and Degünther*, 2001] and the effect of broken cloud fields on surface photolysis frequencies [*Junkermann et al.*, 2001]. In the present study, SHDOM will be used to simulate the atmospheric radiation field in the presence of a biomass burning plume. Results from SHDOM for the actinic flux and the upward irradiance are presented and compared to IPA simulations in order to investigate and quantify the 3D radiation effects.

The 3D radiative transfer simulations were performed by Dr. Barbara Früh, Institute for Atmospheric Physics, University of Mainz.

3.2 Scenario for the Radiative Transfer Modeling

In the following section, the scenario for the model simulations, i.e., the aerosol distribution, aerosol optical properties, and the model parameters, is presented.

The spatial distribution of the aerosol particles is taken from the 3D atmospheric transport simulation with the active tracer high-resolution atmospheric model (ATHAM) presented in Chapter 2. This simulation reproduced the evolution of the biomass burning plume from the Quinault prescribed fire during the Smoke, Cloud, and Radiation-C (SCAR-C) experiment on 21 September 1994 with reason-

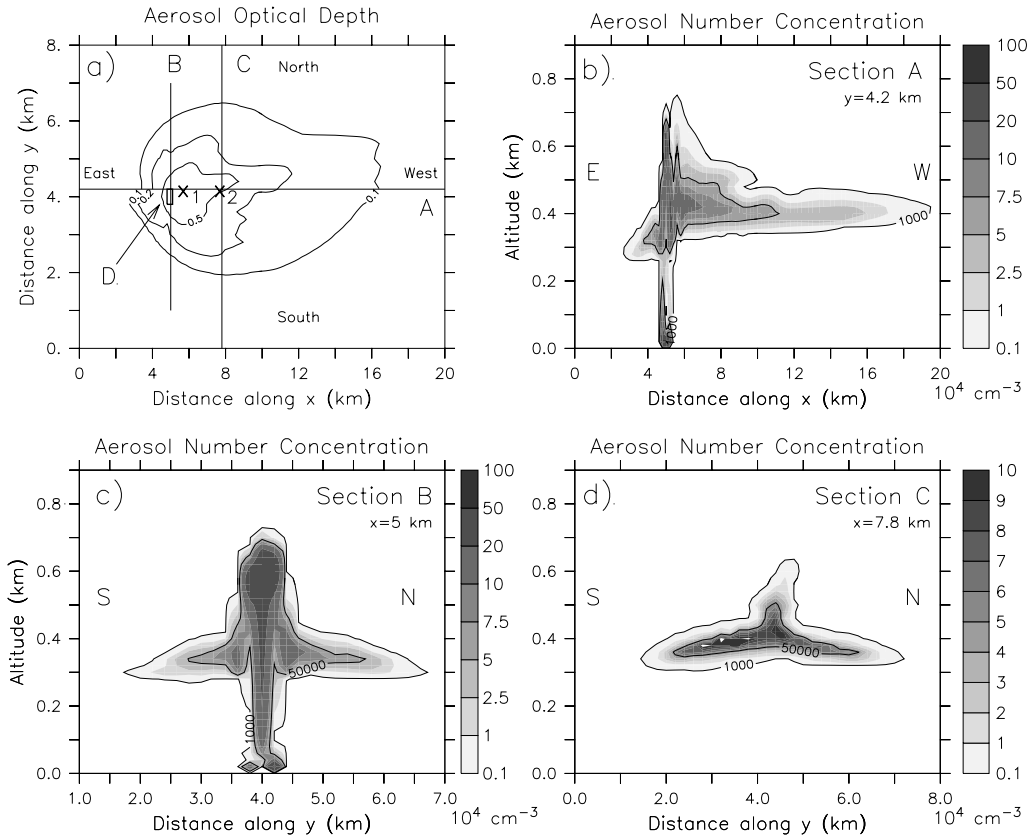

Figure 3.1: (a) Aerosol optical depth at 500 nm. The cross sections (A, B, and C), the plume center (D), and two columns (X1, X2) are also depicted. The fire is located inside box D. Cross sections of the aerosol number concentration (10^4 cm^{-3}) (b) along the plume at y = 4.2 km, (c) across the plume at x = 5 km, and (d) across the plume at x = 7.8 km.

able accuracy. This 19.4 ha clearcut burn on the Pacific Coast of Washington state on the Olympic Peninsula and the resulting aerosol plume were intensively studied by remote sensing and in situ measurements [*Kaufman et al.*, 1996; *Hobbs et al.*, 1996; *Martins et al.*, 1996; *Tanré et al.*, 1997; *Gassó and Hegg*, 1998].

The distribution of the aerosol optical depth as well as the aerosol number concentrations along three cross sections through the simulated aerosol distribution are shown in Figure 3.1. ATHAM was able to reproduce the observed injection height of the aerosol particles (between 300 m and 700 m) as well as the horizontal extent of the plume from the Quinault fire reasonably well (see Chapter 2). The distinct aerosol plume with a width between 3 km and 4 km was transported westwards over the Pacific Ocean. Discrepancies between the observations and the simulated aerosol plume are seen in the underestimation of the aerosol mass concentration as well as the total traveled distance. The aerosol distribution simulated 90 minutes after the ignition of the fire was used.

For the spatial discretization within SHDOM, a model domain of 116 grid cells in the east–west direction, 41 grid cells in the south–north direction and 59 grid cells in the vertical direction was employed. The spatial resolution in the horizontal directions was 200 m, and 20 m in the vertical up to an altitude of 700 m. Since essentially all of the plume was situated within this altitude range, the properties of the plume and its heterogeneity could be reproduced. Above 700 m, the resolution was decreased to 20 km at an altitude of 60 km. The spatial distribution of the aerosol from the original ATHAM simulation was linearly interpolated onto the grid used in SHDOM.

For the aerosol particles, two different optical models are employed, A_{CON} and A_{ABS}. A_{ABS} relies on the same optical properties as in the dynamical ATHAM simulation presented Chapter 2. They are based on measurements of the size distribution and the chemical composition of the aerosol during the Quinault fire [*Martins et al.*, 1996; *Gassó and Hegg*, 1998]. The bimodal log-normal number size distribution with the effective radius $r_{\text{eff}} = 0.14$ μm (Figure 2.6) and a black carbon mass content of 8% yields a value for the single-scattering albedo at 550 nm of $\omega = 0.85$ calculated from Mie-Theory (see Figure 2.7). This value for the single-scattering albedo corresponds to a rather high aerosol absorption, but it is a reasonable value for biomass burning aerosol [*Hobbs et al.*, 1996; *Reid et al.*, 1998]. In order to investigate the impact of aerosol absorption, a second aerosol model (A_{CON}) is defined assuming conservative scattering, i.e., the single-scattering albedo of A_{ABS} is set to unity at all wavelengths. For both aerosol models, the phase function is identical and was approximated from the asymmetry parameter using the Henyey–Greenstein function, which was expanded into Legendre polynomials.

Profiles for the meteorological data (temperature and pressure) and the ozone concentration were taken from the compilation for the standard atmosphere under midlatitude summer conditions [*Anderson et al.*, 1986]. These vertical profiles are assumed to be horizontally homogeneous. The ocean is treated as a lambertian surface. Sun glint is not considered and a constant value for the surface albedo of 1% was chosen at all wavelengths. The low surface albedo allows the effects of the aerosol plume to be easily identified in the simulations.

The spectral radiation transfer equation was solved for the wavelengths $\lambda =$ 320 nm, 400 nm, 550 nm, and 800 nm. The solar azimuth was set to 90°, leading to illumination of the plume from the south. The simulations were carried out for 5 solar zenith angles (SZA): $\theta = 0°$, 30°, 45°, 60°, and 70°. The radiative quantities that are investigated are the actinic flux and the upward irradiance. The actinic flux and the upward irradiance were calculated using the 3D model setup with 8 streams in zenith and 16 streams in azimuth direction. Lateral boundary conditions were assumed to be open so that outside the model domain no aerosol exists.

For the following comparison of the model results, some abbreviations are introduced. Every model simulation is characterized by the kind of approximation (3D or IPA) as well as the aerosol model used (CON, ABS). For instance, the 3D simulation using the conservative aerosol model is called 3D_CON. Additionally, some comparisons are presented for the clear sky case: NOAERO.

In the following sections, relative differences between different model simulations for different radiative quantities are presented. The definition of all the relative differences (%) is

$$\Delta\Phi(A) = \left(\frac{\Phi(REF) - \Phi(A)}{\Phi(A)}\right) \times 100, \tag{3.1}$$

where the letter A stands for the simulation NOAERO, IPA_CON, IPA_ABS, 3D_CON, or 3D_ABS. The parameter Φ is F or E_{up}, where F is the actinic flux, and E_{up} the upward irradiance. The definitions of F and E_{up} as well as of the reference simulation (REF) are given in the following sections.

3.3 Impact on the Actinic Flux

The actinic flux is the radiative measure which quantifies photodissociation of atmospheric molecules [*Madronich*, 1987] and is therefore a critical parameter for photochemistry. It is defined as the integral of the radiance over the unit sphere and includes direct as well as diffuse radiation:

$$F(\lambda, z) = \int_0^{2\pi} \int_{-1}^{+1} L(\lambda, z, \mu, \varphi)\, d\mu\, d\varphi, \tag{3.2}$$

where $L(\lambda, z, \mu, \varphi)$ is the spectral radiance at the wavelength λ, μ the cosine of the zenith angle θ, φ the azimuth angle, and z the altitude. In the following sections, 3D radiation effects on the actinic flux will be presented.

3.3.1 General Impact of the Aerosol

In this section, the general impact of the biomass burning plume, as well as the effect of the absorbing properties on the actinic flux are investigated. Finally, a comparison between 3D and IPA results is presented.

Figure 3.2a shows the actinic flux at $\lambda = 400$ nm along cross section B in Figure 3.1a through the center of the fire in the north–south direction calculated with the 3D_CON (= REF) simulation for $\theta = 45°$. The relative difference of the actinic flux between the 3D_CON and the NOAERO simulation, ΔF(NOAERO), is presented in Figure 3.2b. The effects of the aerosol plume on the radiation field are very distinct. While the actinic flux is reduced in the lower part and below the plume,

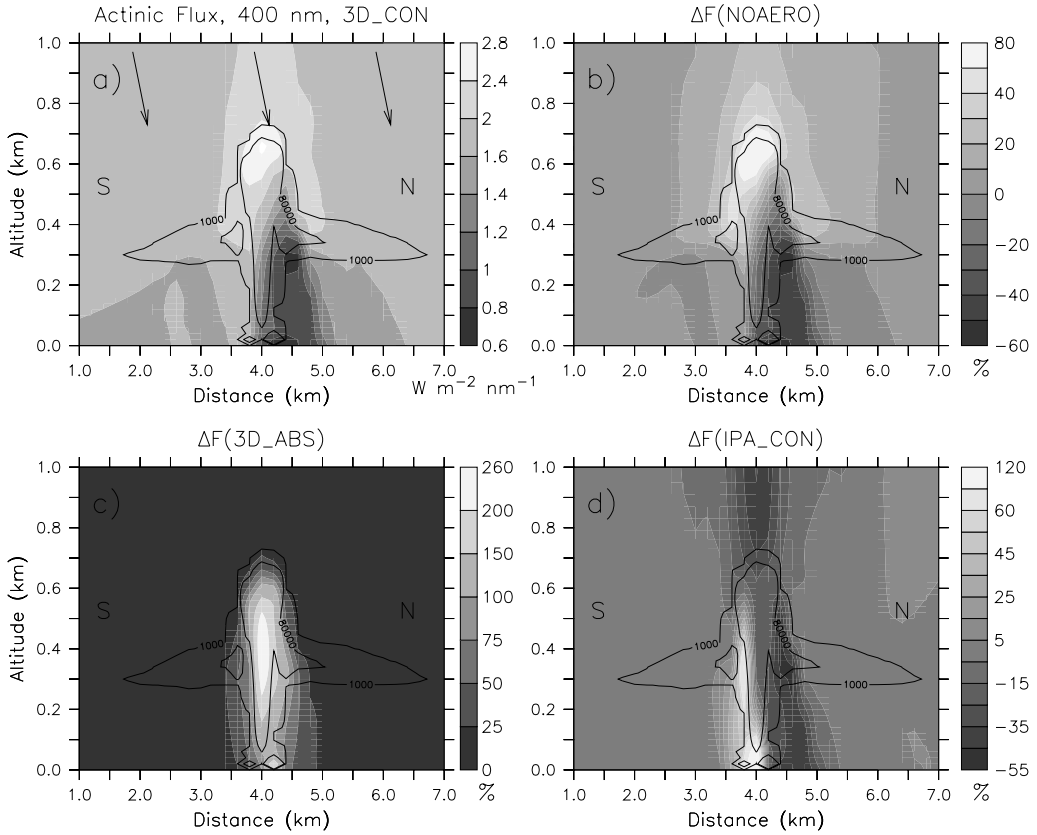

Figure 3.2: (a) Cross section (at Section B) of the simulated actinic flux (W m^{-2} nm^{-1}) at 400 nm using the A_{con} aerosol model for a SZA of 45° across the aerosol plume (x = 5 km). Arrows represent the solar illumination. The other pictures show (b) ΔF(NOAERO), (c) ΔF(3D_ABS), and (d) ΔF(IPA_CON) (REF = 3D_CON for all differences). Contour lines represent the aerosol number concentration (cm^{-3}). Note that the vertical scale differs from the horizontal.

it is enhanced in the upper part and above the plume compared to the simulation without aerosol. A strong reduction (up to −54%) below the plume as well as a pronounced enhancement (up to +72%) in the upper part and above the aerosol plume can clearly be seen. It is interesting to note that the strongest reduction in the actinic flux does not occur in the center of the plume but is shifted to the north. This is due to the shadowing of the direct solar beam by the plume. In Figure 3.2c, ΔF(3D_ABS) is shown, representing the impact of aerosol absorption on the actinic flux. The differences remain relatively small outside the center of the plume but increase to more than +200% within the plume center. This indicates the importance of the correct representation of aerosol absorption for radiative transfer simulations and atmospheric photochemistry. In Figure 3.2d, the relative difference between the actinic fluxes calculated with the 3D_CON and the IPA_CON simulations, ΔF(IPA_CON), is presented. F(IPA_CON) exceeds F(3D_CON) in the upper

part of the plume as well as above the plume significantly. The neglect of horizontal scattering resulting in a loss of photons in the IPA_CON simulation is the reason for the overestimation of the actinic flux in this region. In the lower part of the plume, a dipole-like structure with an underestimation of the actinic flux in the IPA_CON simulation on the illuminated side of the plume (south) and an overestimation on the north side and behind the plume can be observed. The neglect of both the side illumination and the shadowing effect of the plume in the IPA_CON simulation is the reason for this structure. The maximum and minimum values of ΔF(IPA_CON) for the presented cross section are +115% and −51%, respectively.

More than 2 km downwind the fire, the differences in the actinic flux, ΔF(IPA_CON), are comparable low (<5% within and below the plume, <15% above the plume, not shown here), because the optical depth of the plume is small and its structure shows only small 3-dimensional features. Large differences only occur close to the fire and near the center of the plume. The high aerosol numbers, together with their horizontally inhomogeneous distribution, increase the importance of 3D radiation effects.

The general effect of aerosol particles, as well as of the aerosol absorption on the actinic flux and on photochemistry, have already been discussed in the literature [*Dickerson et al.*, 1997; *Jacobson*, 1998a; *Liao et al.*, 1999; *He and Carmichael*, 1999]. Therefore, we focus in the following on the effects of 3D radiative transfer simulations on the atmospheric radiation field, especially on the actinic flux.

3.3.2 Actinic Flux in the Center of the Plume

As shown before, the center of the plume exhibits the largest 3D radiation effects on the actinic flux. Additionally, this region is of special importance for photochemical processes, because here the concentrations of trace gases emitted by the fire (e.g., CO, NO, HCHO) are extremely high, reaching up to some 10 ppm for CO and some 100 ppb for NO_x (= NO + NO_2) [*Ward et al.*, 1992; *Hobbs et al.*, 1996; *Goode et al.*, 2000]. In this part of the plume, sunlight is the limiting factor for photochemistry.

In Figure 3.3 we present the horizontal average of the actinic flux over the plume center, $\langle F \rangle_{\mathrm{pc}}$ ($\langle\,\rangle_{\mathrm{pc}}$ denotes the horizontally averaging over the plume center) for the 3D_CON (=REF) and IPA_CON simulations at a SZA of 45° and wavelength of 400 nm. The averaging only considers grid boxes where the aerosol number concentration exceeds 80 000 particles cm^{-3} in the column above the fire defined by the rectangle with x = 4.8 km to 5.1 km, y = 3.8 km to 4.2 km (Box D in Figure 3.1a). For the conservative aerosol model (Figure 3.3a), $\langle F(\mathrm{IPA\_CON}) \rangle_{\mathrm{pc}}$ exceeds $\langle F(\mathrm{3D\_CON}) \rangle_{\mathrm{pc}}$ at nearly all altitudes. This can be explained by the horizontal photon transfer in the 3D_CON simulation which is not taken into account in the IPA simulation. Photons scattered horizontally by aerosol particles escape from

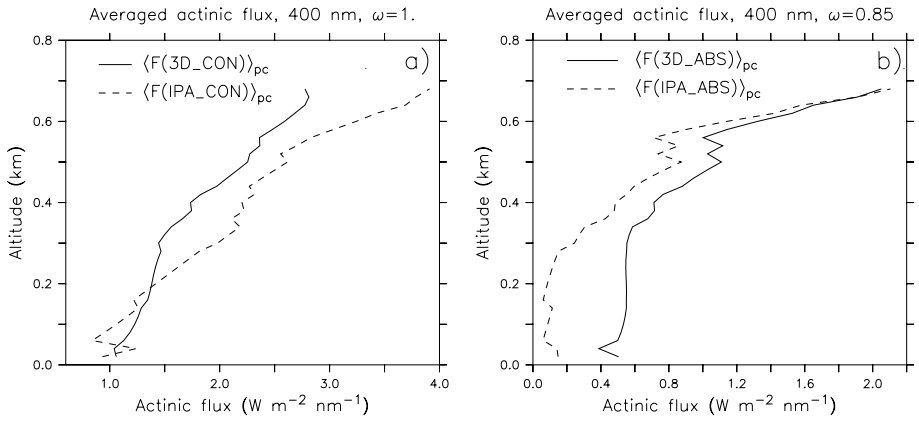

Figure 3.3: Horizontally averaged actinic flux (W m^{-2} nm^{-1}) at 400 nm calculated for a SZA of 45° for the (a) conservative and the (b) absorbing aerosol models. The average includes only grid boxes with aerosol number concentrations higher than 80 000 particles cm^{-3} in Box D (Figure 3.1a) close to the fire. Note the different scales on the abscissa.

the region of the smoke plume. In the IPA case, no horizontal loss or gain of photons is considered. The averaged difference between the 3D and the IPA simulations for this case is $\overline{\Delta\langle F(\text{IPA\_CON})\rangle_{\text{pc}}} = -10.7\%$ (the bar represents the vertical average).

In Figure 3.3b, the horizontally averaged actinic fluxes within the center of the plume are shown for the case of the absorbing aerosol model, $\langle F(\text{3D\_ABS})\rangle_{\text{pc}}$ and $\langle F(\text{IPA\_ABS})\rangle_{\text{pc}}$. This is the more realistic case for a biomass burning plume although the absorption might be overestimated (see Section 2.7). For both cases the values are much lower than in the simulations using the conservative aerosol model. The differences between 3D_ABS and IPA_ABS are distinct: $\langle F(\text{3D\_ABS})\rangle_{\text{pc}}$ exceeds $\langle F(\text{IPA\_ABS})\rangle_{\text{pc}}$, especially in the lower part of the plume up to an altitude of about 350 m. While in the IPA_ABS simulation the actinic flux nearly goes down to zero below the plume (0.09 W m^{-2} at z = 200 m), the 3D_ABS simulation gives a significant value for the actinic flux (0.55 W m^{-2} at z = 200 m). This behavior can be explained by a net horizontal transport of photons into the plume center from regions with low aerosol loading which could not be taken into account in the IPA simulation. Two processes account for the horizontal transfer of photons: direct illumination of the plume center from the side and the scattering from regions with lower aerosol loading into the plume center. In the plume center, the optical depth and the absorption are very high (maximum: $\tau_{\text{max}} = 13.2$, average: $\tau_{\text{ave}} = 8.1$ at 400 nm) leading to the strong reduction of radiation in the plume center in the IPA_ABS simulation. In the 3D_ABS simulation, the direct solar beam is not attenuated by this large optical depth, but is affected by a much smaller optical depth along its way to the plume center, because of the lateral illumination. Additionally, Rayleigh scattering from regions outside the plume center into the plume enhances

	Wavelength (nm)			
SZA	320	400	550	800
	$\overline{\Delta\langle F(\text{IPA\_CON})\rangle_{\text{pc}}}$			
0°	−36.7	−39.5	−44.6	−44.3
30°	−27.7	−27.8	−31.0	−33.4
45°	−17.4	−10.7	−9.9	−14.5
60°	−7.1	14.2	32.7	26.9
70°	−6.9	37.5	91.7	95.3
	$\overline{\Delta\langle F(\text{IPA\_ABS})\rangle_{\text{pc}}}$			
0°	142.6	68.9	8.6	−19.0
30°	199.8	120.2	41.7	−0.3
45°	293.1	216.2	112.5	38.3
60°	358.2	378.7	261.7	126.4
70°	350.0	509.6	473.2	285.3

Table 3.1: Relative difference (%) of the averaged actinic flux in the center of the plume (Box D in Figure 3.1a) between the 3D_CON (= REF) and the IPA_CON simulations, $\overline{\Delta\langle F(\text{IPA\_CON})\rangle_{\text{pc}}}$, and the 3D_ABS (= REF) and the IPA_ABS simulations, $\overline{\Delta\langle F(\text{IPA\_ABS})\rangle_{\text{pc}}}$, for different wavelengths and solar zenith angles.

the actinic flux. Although there is no spatial inhomogeneity in the distribution of molecules that are responsible for Rayleigh scattering, there is a net flux into the plume. This is because the number of photons is much larger outside the plume, leading to higher scattering into the plume center than out of it. The loss of photons from the plume center due to Mie scattering by the aerosol particles is comparably small because of the limited number of available photons. The averaged difference for this case, $\overline{\Delta\langle F(\text{IPA\_ABS})\rangle_{\text{pc}}}$ (REF = 3D_ABS), is +216%. In contrast to the conservative aerosol model, horizontal photon transport leads to an increase in the actinic flux in the plume center when aerosol absorption is taken into account. Only at the lowerest altitudes a similar effect is observed in the case of the conservative aerosol (Figure 3.3a).

3.3.3 Dependence on Solar Zenith Angle and Wavelength

In this section, the dependences of the 3D effects on the actinic flux in the plume center on solar zenith angle and wavelength are presented.

The vertically averaged differences for all performed calculations are presented in Table 3.1. In the case of overhead sun and conservative aerosol, the actinic flux resulting from the IPA simulation is larger than the 3D results ($\overline{\Delta\langle F(\text{IPA\_CON})\rangle_{\text{pc}}} < 0$) at all wavelengths, because of the possibility of horizontal escape of photons in the 3D simulations. There is a slight decrease in $\overline{\Delta\langle F(\text{IPA\_CON})\rangle_{\text{pc}}}$ with increasing wavelength. For overhead sun, only scattering contributes to the horizontal photon transfer. Rayleigh scattering is the responsible process for the photon transfer into the plume, while Rayleigh and Mie scattering are responsible for the horizontal transfer out of the plume. With increasing wavelength, the magnitude of Rayleigh scattering decreases faster than that of Mie scattering. This leads to larger relative differences in the actinic flux in the plume center at longer wavelengths, because the net horizontal transfer out of the plume center increases in the 3D_CON simulation. Additionally, the mean free path of a photon increases at longer wavelengths, which enhances the likelihood that a scattered photon can escape from the plume before it undergoes further scattering.

For larger SZAs, the direct solar beam also contributes to the horizontal photon transfer in the 3D simulation and $\overline{\Delta\langle F(\text{IPA\_CON})\rangle_{\text{pc}}}$ increases at all wavelengths. The attenuation of the direct solar beam is less in the 3D simulations than in the IPA simulations, because the direct solar beam does not interact with the dense part of the plume above the fire but enters the plume center from the side. This effect is largest for wavelengths at which the direct solar beam has the highest contribution to the actinic flux. This is the case for the longer wavelengths that are not as much affected by Rayleigh scattering as the shorter wavelengths. At $\lambda = 320$ nm, the difference remains negative even at a SZA of 70° because of the fact that the actinic flux at this wavelength is almost fully determined by diffuse light, because of strong ozone absorption and Rayleigh scattering.

In the case of the absorbing aerosol model A_{ABS}, the values of $\overline{\Delta\langle F(\text{IPA\_ABS})\rangle_{\text{pc}}}$ are much larger than the corresponding values for A_{CON} ($\overline{\Delta\langle F(\text{IPA\_CON})\rangle_{\text{pc}}}$), but the dependence on wavelengths and SZAs are similar. In almost all cases the values of $\overline{\Delta\langle F(\text{IPA\_ABS})\rangle_{\text{pc}}}$ are positive, representing a higher actinic flux in the 3D than in the IPA simulations. The reason for this underestimation of the actinic flux by the IPA simulation is the low actinic flux within the plume center, because of the high aerosol absorption. Horizontal photon loss from the plume center therefore is limited, and gain of photons due to side illumination and Rayleigh scattering makes up a significant contribution to the total number of photons in the plume. This contribution is neglected in the IPA simulations resulting in the reduced actinic flux. Only at a wavelength of 800 nm and a SZA of 0° and 30°, the horizontal photon transfer leads to a net loss, because the aerosol optical depth at $\lambda = 800$ nm is comparably small, leading to a comparable high number of photons in the plume.

As the effect of side illumination is zero ($\theta = 0°$) or limited ($\theta = 30°$), scattering processes result in net horizontal photon loss, due to the small contribution from Rayleigh scattering at this wavelength.

At larger SZAs, the contribution of the direct solar light in the plume center in the 3D_ABS simulation increases, because of the illumination of the lateral plume faces, and $\overline{\Delta\langle F(\text{IPA\_ABS})\rangle_{\text{pc}}}$ exceeds +100% at all wavelengths. In the case of absorbing aerosol A_{ABS}, the relative contribution of the direct light to the actinic flux is enhanced as compared to the conservative scattering aerosol A_{CON}, because multiple scattering within the plume is strongly reduced due to the aerosol absorption.

3.3.4 Possible Impact on Photochemistry

Photodissociation of atmospheric molecules primarily occurs at wavelengths shorter than 420 nm. For these wavelengths, the results show a strong variability of the effects of 3D radiative transfer simulations, depending on the solar zenith angle and the absorbing properties of the aerosol particles. In the nonabsorbing case, for most SZAs the actinic flux and therefore the photolysis frequencies are overestimated by IPA_CON simulations by +10 to +40% because of the neglect of horizontal photon loss. At larger SZAs, this effect is opposite due to solar side illumination. The magnitude of this effect is expected to depend strongly on the spatial dimensions of the plume considered. In the case of an absorbing aerosol, the available actinic flux for photodissociation is heavily underestimated by the IPA_ABS simulation in the cases considered here. It is not possible to give a general estimate of the error in the actinic flux due to the neglect of 3D radiative transfer effects, because the strong impact of aerosol absorption, which can lead to an overestimation as well as to an underestimation of the actinic flux in IPA simulations. It is clear, however, that the impact of neglecting the 3-dimensional nature of radiative transfer in cloud- and plume-resolving photochemical models will in many cases results in significant errors for the simulation of photolysis frequencies.

How these errors in the simulated photolysis frequencies transfer into the simulation of photochemical processes, e.g., the formation of ozone in the troposphere, needs further investigation. Again, a general statement even for the sign of the 3D impact is not possible, because photochemical ozone production strongly depends on the available NO_x concentration. However, under the conditions of a biomass burning plume, i.e., absorbing aerosol and high concentrations of organic compounds and nitrogen oxides, the inclusion of 3D radiation effects would lead to enhanced photolysis frequencies and enhanced photochemical ozone formation. Three-dimensional radiation effects might contribute to the fast photochemistry appearing within these plumes. Also for the case of a convective cloud, 3D radiation effects might influence photochemistry. However, due to the conservative optical properties of the cloud

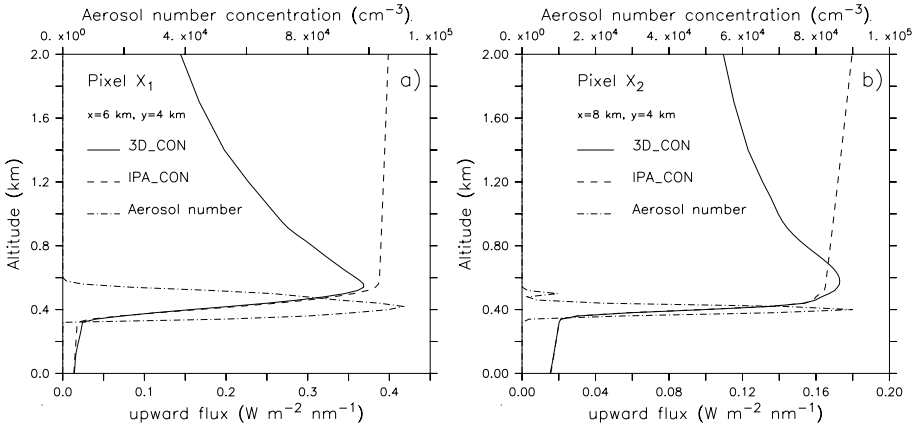

Figure 3.4: Vertical profile of the upward irradiance (W m^{-2} nm^{-1}) at 550 nm at two different model pixels (X_1 and X_2 in Figure 3.1a) for a SZA of 45° for the A_{con} aerosol model calculated with the 3D and the IPA simulations. Additionally, the aerosol number concentration (cm^{-3}) is shown. The aerosol optical depth at 550 nm is (a) $\tau = 0.94$ and (b) $\tau = 0.32$.

droplets, photolysis frequencies are expected to be reduced in the 3D case relative to the 1D case due to horizontal photon loss.

3.4 Impact on the Upward Irradiance

In the following section, three-dimensional effects on the upward irradiance over this finite biomass burning plume are investigated. The upward spectral irradiance, E_{up}, is defined as the integral of the radiance L weighted with the cosine of the zenith angle, μ=cos(θ), over the lower hemisphere:

$$E_{\mathrm{up}}(\lambda, z) = \int_0^{2\pi} \int_{-1}^{0} L(\lambda, z, \mu, \varphi)\, \mu \, d\mu \, d\varphi \, . \tag{3.3}$$

The irradiance is a key parameter for the atmospheric energy budget. Therefore, measurements as well as modeling of the atmospheric irradiance are of high interest in the atmospheric science [*Valero et al.*, 1997; *Wendisch and Keil*, 1999]. In the following, the impact of 3D effects on the upward irradiance, E_{up}, are investigated for the aerosol distribution used in this study.

In Figure 3.4, the vertical profiles of the upward irradiance at 550 nm at two grid points (marked X_1 and X_2 in Figure 3.1a) calculated with the 3D_CON and the IPA_CON simulations, E_{up}(3D_CON) and E_{up}(IPA_CON), respectively, are presented. Inside the plume as well as close to the plume top, the two simulations agree reasonably well. Above the plume, E_{up}(3D_CON) decreases, while E_{up}(IPA_CON) increases with altitude. The vertical decrease of E_{up}(3D_CON) is explained by the

limited horizontal extent of the smoke plume. With increasing distance from the plume, the solid angle of the plume decreases. Since the ground albedo is smaller than the albedo of the smoke aerosol, the reflectance of columns without aerosol is much smaller than that of the columns containing aerosol. In the IPA simulation, the effect of the limited extent of the smoke plume is not taken into account, because of the assumption of horizontal homogeneity.

In Figure 3.4b, representing conditions further downwind at X_2, the decrease of E_{up}(3D_CON) with altitude is similar to that in Figure 3.4a. But, between 450 m and 700 m altitude, E_{up}(3D_CON) exceeds E_{up}(IPA_CON). The reason for this underestimation of E_{up} in the IPA simulation is the fact that the optical depth in this column is low ($\tau = 0.32$) compared to the surrounding columns (see Figure 3.1a). Enhanced reflectance from the surrounding columns leads to enhanced upward irradiance in the 3D simulation that cannot be reproduced by the IPA simulation. At higher altitudes, this effect decreases and E_{up}(IPA_CON) exceeds E_{up}(3D_CON) as in Figure 3.4a.

The magnitude of the reduction of E_{up} with altitude is determined by the horizontal dimension of the aerosol plume and the altitude above the plume. There is no significant effect of the wavelength, SZA, or aerosol model. This investigation shows that 3D effects have to be taken into account when observed reflected irradiances over a finite plume or cloud are interpreted with radiative transfer models. For the interpretation of upward radiances, however, three-dimensional radiation effects are not expected to have a significant effect, because the viewing angle of the radiances is much smaller than that of the irradiances. Simulation of radiances with one-dimensional radiative transfer models are therefore not affected by the effect of the decreasing solid angle under which the plume is seen with increasing plume distance.

In the Sections 2.6 and 2.7, measurements of E_{up} above the plume ($\sim$600 m) from the Quinault fire were compared to model simulations using a 1D radiative transfer model. Using the aerosol optical depths generated from the ATHAM simulation, an underestimation of the simulated E_{up} is found (see Section 2.6). However, increasing the aerosol optical depth improves the agreement between the observations and the simulations (see Figure 2.21d). From measurements of the zenith radiance above the plume, a lower limit for the single-scattering albedo of $\omega = 0.94$ in the visible wavelength region was derived in Section 2.7. Using this value of ω for the calculation of the upward irradiance, the one-dimensional model overestimates the observations by about 50% (Figure 2.22d). However, the overestimation of the simulated upward irradiance using a 1D radiative transfer model due to the neglect of the reduced solid angle of the plume, is in the same order of magnitude (see Figure 3.4). The use of a one-dimensional transfer model in Section 2.7 is therefore the most probable cause of the overestimation of the upward irradiance in Section 2.7.

3.5 Conclusions

The impact of three-dimensional (3D) radiative transfer effects on the actinic flux and the upward irradiance in the presence of an aerosol plume from a vegetation fire was investigated. In order to quantify this effect, three-dimensional model simulations were compared with one-dimensional simulations using the independent pixel approximation (IPA). Horizontal photon transport due to direct illumination as well as horizontal scattering which are not accounted for in the IPA simulations are responsible for the difference between these two simulations.

For the scenario investigated here, the three-dimensional effect on the actinic flux within the plume center ranges from -40% to more than $+200\%$, depending on the solar zenith angle and the absorbing properties of the aerosol. The magnitude of the difference indicates the importance of three-dimensional radiative effects for photochemical processes within biomass burning plumes and similar atmospheric phenomena, e.g., convective clouds. However, at present, 3D radiative transfer models are not included in atmospheric chemistry models because of their high computer time and memory requirements. The upward irradiance above the plume decreases with altitude in the 3D simulation because of the finite horizontal dimension of the plume. This effect cannot be reproduced with one-dimensional (1D) simulations, which suggests limitations in the interpretation of measurements of the upward irradiance with 1D radiative transfer models.

Further investigations of 3D radiation effects using both model simulations and measurements would be desirable. This study shows that 3D effects on the atmospheric radiation field and their potential impact on photochemistry need to be considered, and suitable parameterizations should be investigated.

Chapter 4

Simulation of Photochemical Processes in a young Biomass Burning Plume[1]

Abstract. The photochemistry in young biomass burning plumes depends highly on the emissions from the fire. Chemical processes are strongly linked to the transport and dilution of the emissions. In the present study, a three-dimensional plume model is used to investigate the photochemical evolution of a biomass burning plume during the first tens of minutes after the fire emissions have been released into the atmosphere. The model results represent the evolution of the plume from the Quinault prescribed fire conducted during the Smoke, Cloud, and Radiation-C (SCAR-C) experiment. The modeled ozone concentrations of about 70 ppb are close to observations. The main nitrogen reservoir species downwind the fire are HNO_3 and peroxyacetyl nitrate (PAN), accounting for about $\sim 60\%$ and $\sim 30\%$ of the total nitrogen reservoir species, respectively. Photolysis of formaldehyde, which is emitted from the fire, is the primary source for radicals in the plume. Omitting the emissions of oxygenated volatile organic compounds in the modeled fire plume leads to unrealistically low ozone concentrations in the simulations. Additionally, neglecting these emissions changes the partitioning between the nitrogen reservoir species in favor of the formation of HNO_3. A non-absorbing aerosol as well as lower emission of NO_x in the simulations enhance the radical concentration, photochemical ozone formation, and the oxidation efficiency. It is shown that the correlation between propene and CO, the enhancement ratio, can be used as a measure for the oxidation efficiency of individual biomass burning plumes. Further investigations of the atmospheric processes in young biomass burning plumes will increase our understanding of the interaction of transport and chemical processes not only in a biomass burning plume, but also in other convective systems.

[1]This chapter is in preparation for publication in the *Journal of Geophysical Research,* 2001, with M. O. Andreae and H.-F. Graf as coauthors.

4.1 Introduction

Vegetation fires are a major source of several trace gases as well as aerosol particles [*Crutzen and Andreae*, 1990]. Large amounts of carbon- (e.g., CO, CH_4, C_2H_4, HCHO), nitrogen- (e.g., NO, NH_3), sulfur- (e.g., SO_2, COS), and halogen- (e.g., CH_3Cl) containing molecules are emitted into the atmosphere from fires [*Andreae and Merlet*, 2001]. Photochemical processing of these primary emissions leads to the formation of secondary pollutants, e.g., ozone. Several field studies show a large influence of primary emissions from biomass burning on the atmospheric composition and the formation of secondary pollutants in different regions, e.g., the Arctic Boundary Layer Experiment (ABLE-3B) [*Harriss et al.*, 1994], the Southern Tropical Atlantic Region Experiment (STARE) [*Andreae et al.*, 1996b], the Smoke, Clouds, and Radiation-Brazil experiment (SCAR-B) [*Kaufman et al.*, 1998], and the Experiment for Regional Sources and Sinks of Oxidants (EXPRESSO) [*Delmas et al.*, 1999]. Long-term satellite measurements provide evidence that vegetation fires influence the atmospheric composition regularly on a regional to global scale, especially in the tropics [*Fishman et al.*, 1991; *Fishman and Brackett*, 1997; *Thompson et al.*, 2001].

Several global atmospheric chemistry models include emissions from biomass burning and have been used to quantify the contribution of biomass burning emissions to the atmospheric concentration of several trace gases, e.g., CO and NO_x ($NO_x = NO + NO_2$). The impact of biomass burning on global tropospheric ozone concentrations were investigated in several studies because of the special role of ozone for atmospheric chemistry and climate [e.g., *Lelieveld and Dentener*, 2000; *Marufu et al.*, 2000; *Galanter et al.*, 2000; *Granier et al.*, 2000]. All studies estimate the contribution of biomass burning to the global tropospheric ozone concentration in the order of 10%. Nevertheless, on a regional scale close to the source region, biomass burning contributes to a much larger extent to the ozone concentration [*Marufu et al.*, 2000].

Regional and global models tend to underestimate ozone concentrations in tropical regions affected by biomass burning, although the concentrations of CO are reproduced reasonably well [*Emmons et al.*, 2000]. Nitric acid concentrations are overestimated in these models, especially in biomass burning regions [*Wang et al.*, 1998b; *Hauglustaine et al.*, 1998; *Lawrence et al.*, 1999]. A comparison of NO_2 satellite measurements with simulations from a global model revealed little deviations over the regions of burning, but showed an underestimation of the modeled NO_2 mixing ratio in areas downwind of the burning, e.g., the southern Atlantic [*von Kuhlmann*, 2001]. This suggests limitations in the representation of the chemical processes occurring in fire-affected areas.

Several observations give evidence that photochemical ozone production takes

place in very young biomass burning plumes, i.e., a few hours after the fire emissions are released [*Evans et al.*, 1974, 1977; *Stith et al.*, 1981; *Hobbs et al.*, 1996; *Goode et al.*, 2000]. Additionally, ozone production due to biomass burning occurs on a regional scale and on a timescale of days. The ozone production in individual biomass burning plumes was found to be insignificant on the regional scale at northern high latitudes, but significant for the tropical South Atlantic [*Mauzerall et al.*, 1996, 1998]. However, regional and global scale models cannot describe the ozone production in individual plumes, because of their coarse grid compared to the size of a fire. In these models, emissions from biomass burning are introduced into an unrealistic large area. As photochemical ozone production is a highly nonlinear process, depending on the concentrations of the emissions, this artificial dilution might lead to an over- or underestimation of the ozone concentration, depending on the concentrations and on the size of the model grid box [*Chatfield and Delany*, 1990; *Poppe et al.*, 1998].

In order to study the chemical processes in biomass burning plumes, box model studies have been performed by several groups [e.g., *Jacob et al.*, 1992; *Mauzerall et al.*, 1998; *Mason et al.*, 2001]. Due to the high initial concentrations in the model simulations, dilution has to be taken into account to reach realistic concentrations of hydrocarbons and nitrogen oxides. The amount of dilution is a very sensitive parameter in these simulations, because the amount of background air mixed into the fire-affected air parcel strongly influences the amount of ozone produced [*Chatfield and Delany*, 1990; *Poppe et al.*, 1998].

In the present investigation, the chemical evolution as well as the transport of the biomass burning emissions are considered in detail. The goal of this study is to investigate the chemical processes leading to the formation of ozone and nitrogen reservoir species during the first tens of minutes after the fire emissions are released. Understanding and quantifying these processes will help to improve the representation of vegetation fires in regional and global model studies. The framework for this study is the active tracer high-resolution atmospheric model (ATHAM) [*Herzog et al.*, 1998; *Oberhuber et al.*, 1998]. In Chapter 2, ATHAM was used to simulate the transport of the aerosol particles from a prescribed fire, and the results showed reasonable agreement with measurements. Here, these dynamical simulations are extended to include chemical processes.

4.2 Model Description

In this section, an overview of the different modules of ATHAM is given.

The 3-dimensional nonhydrostatic plume model ATHAM was designed and has been used for the study of volcanic plumes [*Graf et al.*, 1999]. For a detailed de-

scription of ATHAM, the reader is referred to *Herzog et al.* [1998]; *Oberhuber et al.* [1998] and *Textor* [1999].

ATHAM is formulated with a highly modular structure that allows the inclusion of independent modules. Existing modules treat the dynamics, turbulence, transport, cloud microphysics, gas scavenging, radiation, emissions, and chemistry. In the present investigation, only the transport, turbulence, radiation, emission, and chemistry modules of ATHAM are used. The transport of chemical species is based on the method of *Smolarkiewicz* [1984]. The turbulent quantities are calculated using a modified Kolmogorov-Prandtl formulation. The solar radiation is calculated with the 2-stream practical improved flux method (PIFM) [*Zdunkowski et al.*, 1982], including radiative effects of gases and aerosol particles. The chemical module and the fire emissions are described in more detail in the following sections.

4.2.1 Chemistry Module

Atmospheric chemistry in biomass burning plumes is dominated by the gaseous emissions from the fire. These include CO and other volatile organic compounds (VOCs), nitrogen oxides, as well as halogen-, and sulfur-containing compounds. In order to simulate the chemical processes in detail, a huge number of chemical reactions and species have to be taken into account. Although such detailed chemical mechanisms are available [e.g., *Saunders et al.*, 1997], the possible number of chemical species and reactions to be considered in a 3-dimensional (3D) atmospheric model is limited by the available computer power and memory. Therefore, a selection of species and reactions is necessary for practical purposes. The appropriate selection of the included species depends on the scenario, the simulation time, and the target species as well as on the available computer resources. Several chemical mechanisms are available for regional and global scale modeling of atmospheric photochemistry [e.g., *Lurmann et al.*, 1986; *Stockwell et al.*, 1997; *Brasseur et al.*, 1998; *Horowitz et al.*, 1998; *Zaveri and Peters*, 1999; *Pöschl et al.*, 2000]. While most of the regional-scale mechanisms focus on urban emissions and scenarios, the mechanisms used in global models include polluted as well as background chemistry. None of the available mechanisms is adequate for the simulation of the chemical processes occurring in a young biomass burning plume. Therefore, a selection of chemical reactions was performed to reproduce the chemical processes in a biomass burning plume during the first tens of minutes after the release of the emissions into the atmosphere.

The selection of reactions for the chemical mechanism was focused on the simulation of chemical processes leading to the formation of ozone and nitrogen reservoir species in a young biomass burning plume. Atmospheric chemistry occurring in biomass burning plumes is characterized by high concentrations of VOCs and nitro-

gen oxides. Photochemical ozone production in biomass burning plumes is driven by the oxidation of VOCs by the hydroxy radical (OH) in the presence of high concentrations of NO_x. One substantial difference between urban and biomass burning emissions is the large amount of oxygenated volatile organic compounds (OVOC) that are emitted by vegetation fires. The most important OVOCs emitted from biomass burning are HCHO, CH_3CHO, HCOOH, CH_3COOH, CH_3OH, CH_3COCH_3. All species included in the chemical mechanism are listed in Table A.1. The chemical mechanism is given in Table A.2.

The chemical mechanism includes the oxidation of the primary emissions from biomass burning: CO, CH_4, C_2H_6, C_2H_4, C_3H_6, HCHO, CH_3CHO, HCOOH, CH_3COOH, and CH_3COCH_3. Higher hydrocarbons are neglected because of their low emission ratios. Oxidation by OH is considered for all emitted species. Photolysis of aldehydes and acetone is included as well as ozonolysis of the alkenes. Oxidation of ethene is treated explicitly and includes reactions via the ethoxy radical on the basis of a recent laboratory study [*Orlando et al.*, 1998]. The formation of alkyl nitrates from the reaction of the peroxy radicals with NO is not taken into account, because alkyl nitrates are believed to be formed only from peroxy radicals with more than 3 carbon atoms, which are not included [*Atkinson*, 2000]. Additionally, measurements of the nitrate formation from smaller peroxy radicals are rare and uncertain, often only upper limits are given for the nitrate yield [e.g., *Tyndall et al.*, 2001]. The formation of HNO_4 and $CH_3O_2NO_2$ from the reactions of NO_2 with HO_2 and CH_3O_2 is included. Because of the high NO_x concentrations, cross reactions between higher peroxy radicals are not important under the present conditions [*Kirchner and Stockwell*, 1996]. The dominant reaction partner of the peroxy radicals is NO, only the reaction with HO_2 is additionally taken into account for all peroxy radicals.

Two heterogeneous reactions on aerosol particles are included in the mechanism: reactions of NO_2 to yield HONO, and of N_2O_5 to yield HNO_3. Heterogeneous reaction rates are calculated as first-order rate constants using the simulated aerosol surface: $k_{\mathrm{het}} = (1/4)\,\gamma\,c\,S$, where γ is the uptake coefficient given in Table A.2, c the mean molecular speed, and S the aerosol surface per volume of air. The aerosol surface is calculated from the aerosol mass concentration using a surface area per particle of $1.6{\times}10^{-9}$ cm^2, derived from measurements of the aerosol size distribution (see Figure 2.6).

Photolysis frequencies, which include the effect of absorption and scattering by molecules and aerosol particles are calculated on-line [*Landgraf and Crutzen*, 1998]. The method of *Landgraf and Crutzen* [1998] requires precalculation of polynomial coefficients in order to reduce the number of necessary radiative transfer simulations for the calculation of the photolysis frequencies. However, for some species included

in the present mechanism, these coefficients were not available. The photolysis frequencies of these species were calculated from the linear correlation with a photolysis frequency of a compound with similar absorption cross section and quantum yield. The correlation coefficients were taken from different sources and are given in the notes of Table A.2.

Simulated concentrations from this set of reactions were compared to those from a more detailed chemical mechanism in photochemical box model studies. The agreement for simulations representing the first hours of a young biomass burning plume was very good.

The numerical solution of the differential equations for the chemical integration is performed using the kinetic preprocessor (KPP) [*Damian-Iordache*, 1996]. KPP allows easy combinations of chemical reaction mechanisms and numerical solvers for the differential equations. In the present work, a 2-stage Rosenbrock method (ROS2) was applied to solve the chemical differential equations [*Verwer et al.*, 1997, 1999]. A comparison between ROS2 and and the FACSIMILE package [*Curtis and Sweetenham*, 1987], which uses the Gear-method to solve the differential equations [*Gear*, 1971], showed excellent agreement, but the required computer time was much lower for the ROS2 solver [*von Kuhlmann*, 2001]. The performance of ROS2 was satisfactory up to timesteps of a few minutes. Within ATHAM the chemical timestep is in the order of seconds, so that no numerical errors are expected to be introduced by the use of ROS2.

The numerical solution of the different processes within ATHAM, e.g., transport, microphysics, chemistry, is based on the operator-splitting approach, i.e., all processes are calculated separately and sequentially. The splitting-error introduced from this technique depends on the timestep. For the timestep used in this study, the numerical splitting error is much smaller than other potential errors in the model [*Berkvens et al.*, 2000; *Müller*, 2000].

4.2.2 Fire Emissions

The gaseous emissions from biomass burning include CO_2, CO, CH_4, nonmethane hydrocarbons (NMHCs), oxygenated volatile organic compounds (OVOCs) and nitrogen oxides, as well as aromatic compounds, nitrogen-containing compounds (NH_3, HCN, N_2O), methyl halogens, and sulfur-containing compounds (SO_2, COS) [*Andreae and Merlet*, 2001]. The emitted species is usually characterized by its emission factor or emission ratio [*Andreae and Merlet*, 2001]. The emission ratio relates the emission of the species of interest to that of a reference species, e.g., CO or CO_2.

The emission ratios used in the present study are listed in Table 4.1. The values were taken from laboratory studies, if available. The emission ratios of the carbon- and nitrogen-containing compounds depend on the phase of the fire (flaming or

compound	$\Delta X/\Delta CO$ (%)	note
methane (CH_4)	9.1	1
acetic acid (CH_3COOH)	2.0	2
formaldehyde (HCHO)	2.0	3
ethene (C_2H_4)	1.2	1
acetaldehyde (CH_3CHO)	1.2	4
methanol (CH_3OH)	1.0	3
formic acid (HCOOH)	0.9	5
ethane (C_2H_6)	0.7	1
acetone (CH_3COCH_3)	0.5	4
propene (C_3H_6)	0.5	1
	$\Delta X/\Delta CO_2$	
carbon monoxide (CO)	7.3	1
nitrogen oxides (NO_x)	0.2	1

Notes are 1, emission ratio taken from *Lobert et al.* [1991]; 2, emission ratio derived from *Yokelson et al.* [1997] and *Goode et al.* [1999]; 3, emission ratio derived from *Yokelson et al.* [1997],*Holzinger et al.* [1999], and *Goode et al.* [1999]; 4, emission ratio taken from *Holzinger et al.* [1999]; 5, emission ratio taken from *Yokelson et al.* [1997]

Table 4.1: Emission ratios related to CO for the trace gases emitted by vegetation fires used in the present study. For CO and NO_x the emission ratio related to CO_2 is given.

smoldering). The $\Delta NO_x/\Delta CO_2$ value additionally depends on the nitrogen content of the fuel. Although the emission ratios for CO, CH_4 and other hydrocarbons are relatively well-known, measurements of the emission ratios of the oxygenated organic compounds are still uncertain and differ between different studies.

Measurements close to the fire of the initial NO/NO_x ratio are very sparse; most of them point to values slightly less than 90% [*Griffith et al.*, 1991; *Delmas et al.*, 1995; *Yokelson et al.*, 1996]. Theoretical considerations indicate that in the smoldering stage the NO/NO_x ratio can decrease to 60% [*Lobert and Warnatz*, 1993]. In the following simulations, a value of 75% for the NO/NO_x ratio is used.

The selection of emitted species is based on their importance for the present study, i.e., the photochemistry in a biomass burning plume during the first tens of minutes after the release into the atmosphere. Long-lived hydrocarbons, e.g., ethine, propane, and halocarbons, are neglected, because their reactivity with OH is low, resulting in a relatively long lifetime as compared to the simulation time. Shorter-

lived aromatic compounds, e.g., benzene, toluene, and furanes, are neglected because of their complex, unknown oxidation mechanisms. Inclusion of these species would have required additional chemical reactions, which are highly uncertain in terms of their products and rate coefficients [*Atkinson*, 2000]. However, these aromatic species have the potential to influence photochemistry in young biomass burning plumes [*Koppmann et al.*, 1997; *Mason et al.*, 2001]. Nevertheless, it will be shown that even when aromatic emissions are neglected, atmospheric photochemistry in a young biomass burning plume is simulated realistically.

Glycolaldehyde is omitted as a primary emission from biomass burning in our reference scenario, because its emission was reported so far only by one group using laboratory FTIR measurements [*Yokelson et al.*, 1997]. A sensitivity study including the primary emission of glycolaldehyde did not show a significant dependency of the model results on its emission.

Emission of HNO_3 is not taken into account, because of contradicting results from laboratory studies [*Lobert et al.*, 1991; *Yokelson et al.*, 1997]. Additionally uncertainty in the simulations of HNO_3 arises from the potential scavenging of HNO_3 by the aerosol particles [*Tabazadeh et al.*, 1998]. However, the lifetime of HNO_3 is comparably long, so that additional emissions will not have a substantial impact on atmospheric photochemistry during the first hours after emission.

4.3 Model Initialization

In this section, the scenario for the present model study will be presented. This includes the setup of ATHAM, the meteorological and chemical initial conditions as well as the emissions from the fire and the optical properties of the smoke aerosol.

In this study, ATHAM is used with a constant 3-dimensional field of the meteorological quantities (wind, temperature, pressure) produced by the ATHAM simulation presented in Chapter 2. The scenario in the previous study was shown to give a reasonably good representation of the plume from the Quinault prescribed fire on 21 September 1994. This 19.4 ha clearcut burn on the Pacific Coast of Washington State on the Olympic Peninsula and the resulting plume was intensively studied by remote sensing and in situ measurements during the Smoke, Cloud, and Radiation-C (SCAR-C) experiment [*Kaufman et al.*, 1996; *Hobbs et al.*, 1996; *Martins et al.*, 1996; *Tanré et al.*, 1997; *Gassó and Hegg*, 1998]. The simulated fields of the meteorological quantities were linearly interpolated on the new grid and kept constant over the simulated time of 90 min. The wind field was interpolated so that the resulting wind field is free of divergence. The advantage of this strategy is that the model domain can be kept small and focused on the region of interest. The neglect of a time-dependent wind field is expected to have a small effect on the

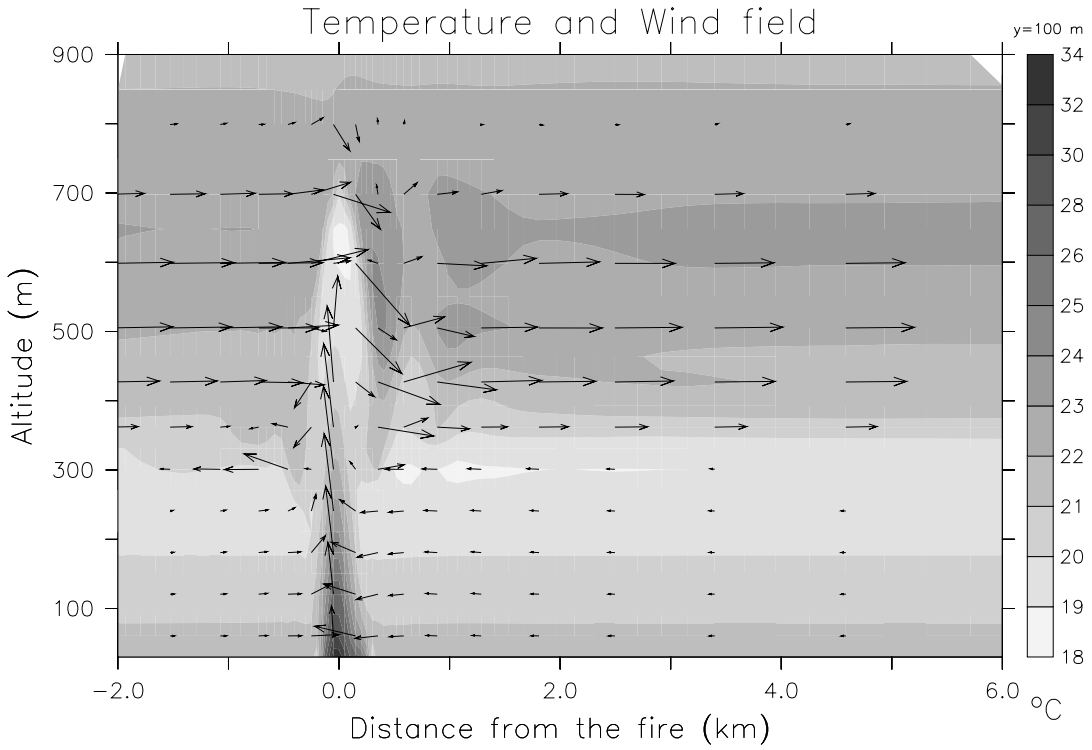

Figure 4.1: Temperature (color coding) and wind field (vectors, m s^{-1}) at y = 100 m. Results are taken from the model simulations presented in Chapter 2, 90 min after the ignition.

absolute values, but the overall description of the plume will not be affected by this assumption. The feedback from chemical processes on the dynamical evolution of the plume, e.g., through a change in atmospheric heating rates due to enhanced ozone concentrations, is negligible on the time scale considered here.

4.3.1 Model Setup

The 3-dimensional model domain (x,y,z) of ATHAM was set to 20 km x 7 km x 900 m with a minimal grid spacing of 50 m x 50 m x 30 m in the central part of the model domain. The number of grid boxes in the x-, y-, and z-direction was 85, 66, and 25, respectively. The transport timestep was set to 3 s. Two chemical time steps of 0.6 s and 2.4 s were calculated during one transport time step. The solar zenith angle was computed for 47° N, September 21, representing the conditions during the Quinault fire. Model simulations were set to correspond to an ignition at 1100 LT (local time) and duration of 90 minutes.

species	total number (molecule)	species	total number (molecule)
CO_2	6.62×10^{30}	CH_3CHO	7.25×10^{27}
CO	6.04×10^{29}	HCOOH	5.44×10^{27}
CH_4	3.43×10^{28}	CH_3COOH	1.21×10^{28}
C_2H_6	4.23×10^{27}	CH_3OH	6.04×10^{27}
C_2H_4	7.25×10^{27}	CH_3COCH_3	3.02×10^{27}
C_3H_6	3.02×10^{27}	NO_x	1.32×10^{28}
HCHO	1.21×10^{28}	aerosol mass	2703 kg

Table 4.2: Cumulative fire emissions 90 min after the ignition. The aerosol mass considers only particles with a diameter smaller than 2.5 μm (PM2.5).

4.3.2 Meteorological Situation

In Figure 4.1, the temperature field and the wind vectors for a cross section at y = 100 m are shown. These 3-dimensional fields were derived from the previous simulation of the Quinault fire presented in Chapter 2 and represent the situation 90 min after the ignition are used in the present study. The temperature increase of about 10 K due to the fire is easily seen. This temperature anomaly above the fire leads to an upward wind that vertically transports the fire emissions into the atmosphere. The atmospheric conditions are determined by a strong temperature inversion between $\sim$300 m and 600 m that prevents the fire-induced convection from reaching higher altitudes. The fire emissions are transported with the prevailing horizontal wind of $\sim$3.5 m s^{-1} to the west over the Pacific Ocean. Note that in the simulations, the x-axis is directed into the main wind direction. Therefore, the emissions are transported to the right in the model simulations.

4.3.3 Fire Emissions

Time-dependent fire emissions for the Quinault fire were obtained from the emission production model (EPM) [*Sandberg and Peterson*, 1984; *Ferguson et al.*, 2000]. EPM takes the loading, consumption, and moisture of different fuel size classes and the duff into account. With theses parameters, the time-dependent emissions of energy, particulate matter, and some trace gases (CO_2, CO, CH_4) are calculated, accounting for different phases of the fire (flaming and smoldering). The EPM-simulated heat and aerosol emissions were presented in Figure 2.4. The CO_2, CO, and CH_4 emissions used in the present study show the same temporal behavior with increasing emissions during the simulation time of 90 min. On the basis of the CO_2 and

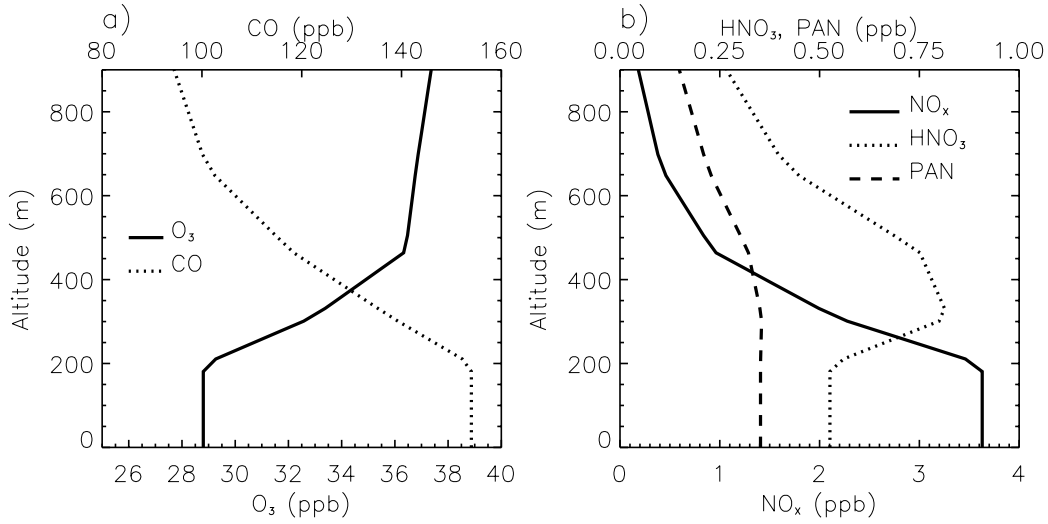

Figure 4.2: Vertical profiles of (a) O_3 and CO and (b) NO_x, HNO_3, and PAN used for the initialization of the model.

CO emissions given by EPM, the emissions of the other compounds were calculated using the emission factors presented in Table 4.1. The cumulative fire emissions over the 90 min of simulation time for all emitted gaseous compounds as well as for the aerosol particles with diameter <2.5 μm (PM2.5) are given in Table 4.2.

CO, CH_4, and aerosol emissions are taken directly from the EPM. All other emissions are calculated using the emission factors. The spatial distribution of the fire emissions in ATHAM is identical to the one used in Chapter 2 (Figure 2.5).

4.3.4 Initialization of the Chemical Species

Initial vertical profiles for the background chemical species are taken from the model of atmospheric transport and chemistry (MATCH) [*Lawrence et al.*, 1999; *von Kuhlmann*, 2001]. Monthly mean values for September at 47° N, 124° W were used. Figure 4.2 shows the initial profiles of O_3, CO, NO_x, HNO_3, and peroxyacetyl nitrate (PAN) used in the model simulation. Ozone mixing ratios in the range of 30 ppb are comparable to observations during the Quinault fire [*Hobbs et al.*, 1996]. Carbon monoxide concentrations decrease with altitude. The same vertical gradient is reproduced for all VOCs. The NO_x mixing ratio strongly decreases with altitude from 3.6 ppb at the ground to 0.1 ppb at an altitude of 900 m. The mixing ratios of HNO_3 and PAN do not show such a strong dependence on the altitude, although there is a small maximum of the HNO_3 concentration at 300 m, because of surface deposition. The initial surface values of the relevant chemical species are given in Table 4.3.

species	mixing ratio	species	mixing ratio
O_3	28.8 ppb	CH_3CHO	300 ppt
CO	154 ppb	HCOOH	68 ppt
CH_4	1.82 ppm	CH_3COOH	78 ppt
C_2H_6	800 ppt	H_2O_2	400 ppt
C_2H_4	500 ppt	CH_3OOH	300 ppt
C_3H_6	100 ppt	NO_x	3.6 ppb
CH_3OH	3.6 ppb	HNO_3	500 ppt
CH_3COCH_3	2.7 ppb	PAN	400 ppt
HCHO	1.6 ppb		

Table 4.3: Initial surface mixing ratios for the chemical compounds.

4.3.5 Calculation of the Photolysis Frequencies

For the calculation of the photolysis frequencies, the vertical extent of the model domain is increased up to 60 km. Inside the ATHAM model domain, i.e., up to an altitude of 900 m, temperature, pressure, as well as ozone and aerosol concentrations are taken from the simulations. Above 900 m, observations, supplemented by data from the standard atmosphere for midlatitude summer conditions are used as described in Section 2.4.2. No aerosol is considered above 900 m. The wavelength-independent surface albedo was assumed to be lambertian and set to 6%. This value is representative for vegetation as well as for the ocean surface in the wavelength region of interest [*Briegleb et al.*, 1986].

The interaction of the smoke particles with the solar radiation is included in the calculation of the photolysis frequencies. The aerosol optical properties were calculated on the basis of measurements of the aerosol composition [*Martins et al.*, 1996] and size distribution [*Hobbs et al.*, 1996; *Gassó and Hegg*, 1998] from the Quinault fire as explained in Section 2.4.4. The reported black carbon (BC) aerosol mass content of 8% leads to a relatively high aerosol absorption. The single-scattering albedo at 400 nm is calculated to be $\omega(400\ \text{nm}) = 0.86$. Similar values of ω are reported from in situ measurements of the single-scattering albedo from biomass burning aerosol [*Hobbs et al.*, 1996; *Reid et al.*, 1998]. The optical properties of the aerosol are linearly interpolated on the wavelength grid used for the calculation of the photolysis frequencies [*Landgraf and Crutzen*, 1998]. Photolysis frequencies were calculated at every transport time step (3 s) in order to account for the changing spatial distribution of the aerosol.

One-dimensional radiative transfer simulations were performed for every column of the model (independent pixel approximation (IPA) [*Cahalan et al.*, 1994]). No

interaction between neighboring columns was considered, i.e., no horizontal photon transfer. The neglect of three-dimensional radiation effects has a large impact on the calculated photolysis frequencies, especially in the center of the plume above the fire. Because the concentration of trace gases is very high in this region, these effects might influence photochemical processes significantly as shown in Chapter 3. However, 3D radiative transfer simulations cannot be performed on-line within a 3D atmospheric transport model at the present, because of computational limitations. Nevertheless, their possible effects have to be kept in mind when interpreting the model results.

In the following sections, the results from the model simulations will be presented. Section 4.4.1 introduces the general appearance of the plume due to the transport of the emissions. The photolysis frequencies and the influence of the emitted aerosol particles and their optical properties on the photolysis frequencies are presented in Section 4.4.2. The simulation results for the trace gases that are involved in photochemical processes will be presented in Section 4.5 together with an evaluation of the model results by comparison with available measurements. In Section 4.6, the results from three sensitivity studies will be presented and compared to the results from the reference simulation.

4.4 General Model Results

The general appearance of the biomass burning plume is characterized by the concentration of passive tracers. The term 'passive' is used here to indicate that the atmospheric concentrations of these trace species are not significantly influenced by photochemistry on the timescale considered here. Their spatial distribution is identical in all model simulations, because their concentrations are only influenced by transport effects. The aerosol concentration has a significant impact on the photolysis frequencies in and around the plume. The photolysis frequencies are presented in Section 4.4.2 for two different aerosol optical properties.

In the following analysis, the extent of the plume is defined by the aerosol mass concentration. Every grid cell with an aerosol mass concentration exceeding the threshold of 10 μg m^{-3} is considered to be in the plume. Only those grid cells are considered when plume-averaged quantities are presented.

4.4.1 Passive Tracers

As tracer transport in this study is performed with a constant wind field, the resulting spatial distribution of the passive tracers from the fire differs slightly from the simulation presented in Chapter 2.

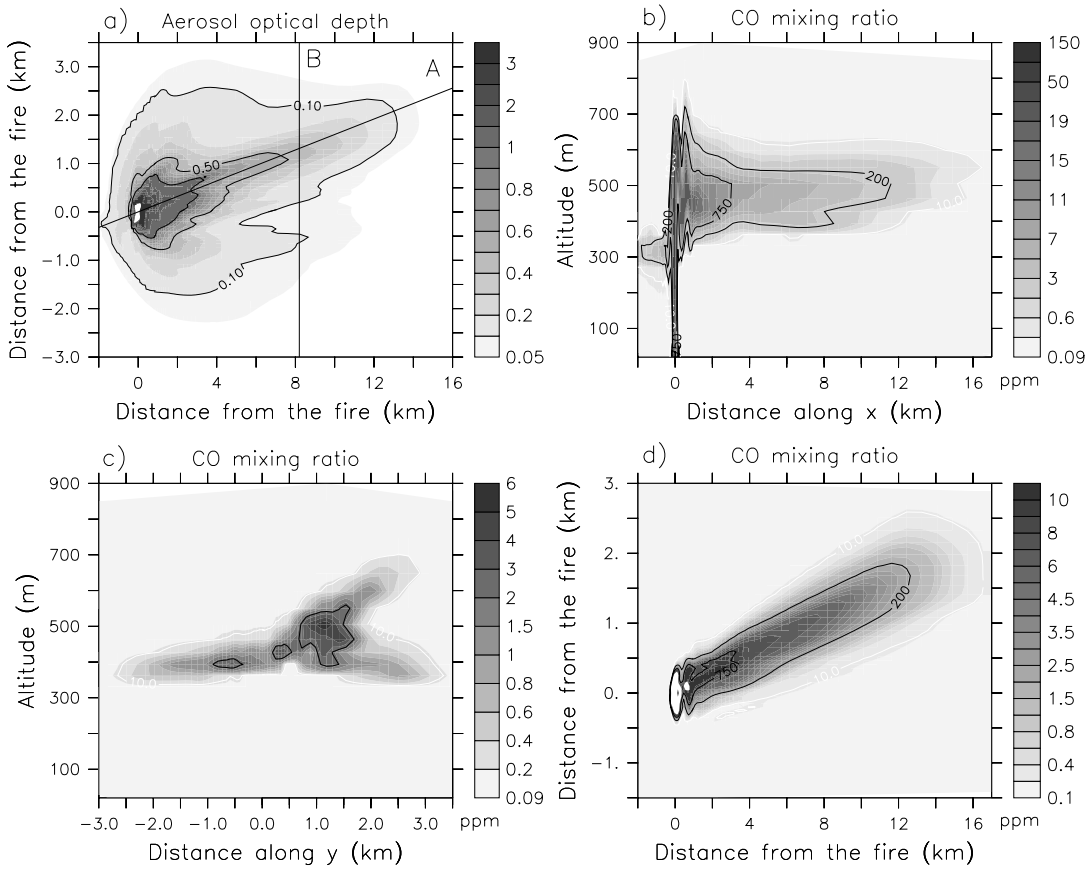

Figure 4.3: (a) Aerosol optical depth at 400 nm (color coding) after 90 min of simulation. The locations of the cross sections A and B are also shown. (b) CO mixing ratio (color coding) along the main plume axis, section A. (c) CO mixing ratio at section B across the plume at x = 8.2 km. (d) CO mixing ratio at an altitude of z = 500 m. Contour lines in b–d represent the aerosol mass concentration (μg m^{-3}). The white line indicates the border of the plume as defined by an aerosol mass concentration of 10 μg m^{-3}.

In Figure 4.3a, the simulated aerosol optical depth τ at 400 nm at 90 min is shown. Above the fire, τ exceeds 10, downwind it decreases to values between 0.2 and 1. Figure 4.3b shows the CO mixing ratio along the main plume axis, depicted as Section A in Figure 4.3a. Figure 4.3c presents the CO mixing ratio along Section B, and Figure 4.3d shows the values of the CO mixing ratio at an altitude of 500 m. CO and aerosol particles are emitted from the fire and transported up to an altitude of $\sim$700 m. The horizontal transport takes place at altitudes between 350 m and 600 m in the planetary boundary layer. The maximum traveling distance within the 90-min simulation time is around 16 km. The simulated CO mixing ratio in the plume is much higher than the background mixing ratio. At a distance of 8.2 km from the fire, corresponding to a traveling time of $\sim$40 min, the maximum and the average mixing ratio of CO in the plume are 5.9 ppm and 1.2 ppm, respectively.

species	VMR (ppb)		species	VMR (ppb)	
	fire	downwind		fire	downwind
CO	18000	1200	HCHO	359.2	21.9
CH_4	2818	1877	CH_3CHO	214.8	11.9
C_2H_6	125.9	8.0	CH_3OH	182.2	12.8
C_2H_4	214.9	11.3	HCOOH	161.0	9.4
C_3H_6	89.3	3.3	CH_3COOH	357.7	20.7
CH_3COCH_3	92.0	7.2	NO_x	403.9	22.2

Table 4.4: Source and downwind volume mixing ratio (VMR) of the emitted trace gases. The mixing ratio close to the fire is calculated as the average plume mixing ratio at z = 150 m. The downwind average is for the cross section at x = 8.2 km, also shown in Figure 4.3c.

The average mixing ratios at the source, defined as the horizontal average at an altitude of 150 m above the fire, as well as the average mixing ratios across the plume at a distance of 8.2 km, Section B in Figure 4.3a, for all compounds emitted by the fire are presented in Table 4.4. The concentrations of C_2H_4, C_3H_6, HCHO, CH_3CHO, and NO_x, are influenced by photochemical processes and are different in the different simulations. The values presented here are taken from the reference simulation.

The high concentrations of VOCs and NO_x in Table 4.4 as compared to the background concentrations (Table 4.3) demonstrate the strong impact of the fire on the chemical composition. The concentrations downwind the fire are smaller than those close to the fire, because of the mixing of the plume with background air and the increasing fire emissions as a function of time. Additionally, chemical processing influences the concentration of the nonpassive species during the simulation time of 90 min. By comparing the temporal and spatial evolution of the passive and nonpassive species, the chemical processes can be separated from the transport processes.

In Chapter 2, it was shown that the simulated aerosol mass concentration compares well with observations. No CO measurements from the Quinault fire are available for a comparison and evaluation of the model results. Measurements in an Alaskan biomass burning plume revealed CO concentrations between $\sim$1 ppm and 15 ppm near the source (<18 km from the fire) and between $\sim$1 ppm and 2 ppm downwind from the fire [*Goode et al.*, 2000]. During the Southern African Fire-Atmosphere Research Initiative 92 (SAFARI 92) as well as during SCAR-B, CO concentrations between 1 ppm and 20 ppm were observed close to fires [*Andreae et al.*, 1996c; *Koppmann et al.*, 1997; *Ferek et al.*, 1998]. Using a ground-based sam-

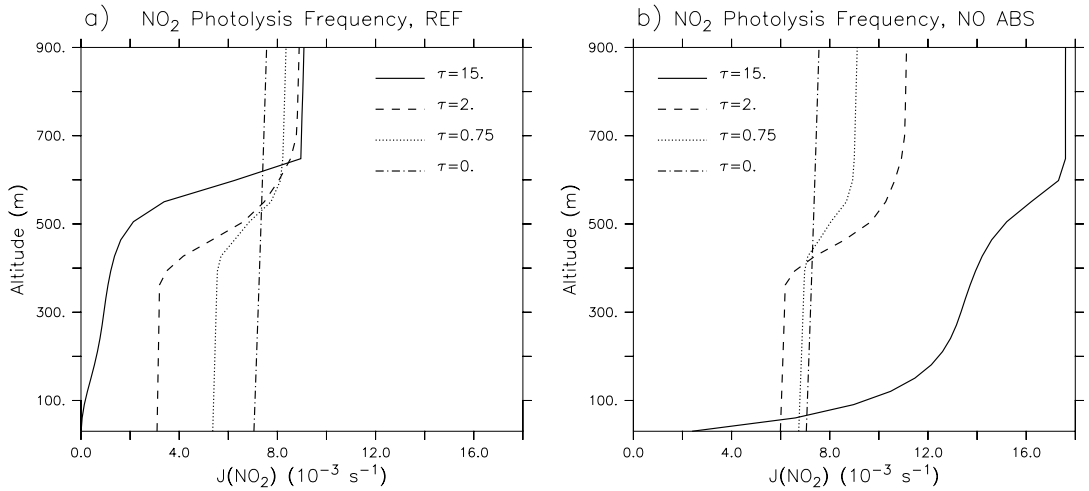

Figure 4.4: Vertical profiles of the NO_2 photolysis frequency at 4 locations along the main plume axis (Section A in Figure 4.3a) with different aerosol optical depths (τ) after 90 min of simulation for the (a) REF simulation and the (b) NO ABS simulation. The solar zenith angle is 48°. The aerosol plume is located between 350 m and 650 m altitude. Values for the aerosol optical depth (τ) are for $\lambda = 400$ nm. The locations of the profiles in the plume along the main axis are at $x = 0.1$ km ($\tau = 15$), $x = 1$ km ($\tau = 2$), and $x = 3.5$ km ($\tau = 0.75$).

pling system, CO mixing ratios up to 270 ppm were measured in a prescribed fire in Brazil [*Ward et al.*, 1992]. All these observations are in the same range as the simulated values for CO. The simulated concentrations of the other emitted trace gases are correlated with CO or CO_2 on the basis of experimental emission factors. The good agreement between the observed and simulated CO mixing ratios leads to the conclusion that the simulated concentrations of the emitted species are representative for emission concentrations in a young biomass burning plume. Therefore, the simulation of the photochemical processes that are closely linked to the concentrations of VOC and NO_x should be a realistic representation of the photochemical processes occurring in young biomass burning plumes.

4.4.2 Photolysis Frequencies

The emitted smoke aerosol strongly affects the solar radiation in the plume, leading to changes in the photolysis frequencies of the chemical species. The impact of the aerosol particles on the photolysis frequency, J, is only presented for NO_2, $J(NO_2)$. However, all photolysis frequencies are similarly affected by the smoke aerosol. In the following, photolysis frequencies calculated with two different aerosol optical properties are presented. The reference simulation (REF) includes the absorbing aerosol model as described in Section 4.3.5. In order to investigate the effect of aerosol absorption on the photolysis frequency and photochemistry, the single-scattering

albedo of the aerosol was set to unity at all wavelengths, representing a conservative, non-absorbing aerosol in a sensitivity study (NO ABS).

Figure 4.4 shows vertical profiles of the NO_2 photolysis frequency at 4 locations with different aerosol optical depths for the (a) REF and (b) NO ABS simulations. In the case of the absorbing aerosol (REF), the particles lead to a strong decrease of $J(NO_2)$ below and a slight increase above the plume that is located between around 350 and 650 m (Figure 4.3b). The strongest decrease is observed above the fire where $J(NO_2)$ locally drops to zero. The decrease of the photolysis frequency below the plume compared to clear-sky conditions is almost linear with optical depth and has a value of -31% for unity optical depth ($\tau = 1.$). The enhancement of $J(NO_2)$ above the plume due to the enhanced albedo of the smoke aerosol compared to the surface saturates at high optical depths. This saturation effect is linked to the absorbing properties of the aerosol. The relative difference for an optical depth of unity is $+13\%$.

In the case of the non-absorbing aerosol (NO ABS), the values of $J(NO_2)$ are larger than those for the absorbing aerosol. The enhancement above the plume is $+27\%$ for unity aerosol optical depth. The decrease of $J(NO_2)$ below the plume is -6% at $\tau = 1$. In the NO ABS simulation, $J(NO_2)$ is larger than the clear-sky value in the upper part of the plume (between an altitude of $\sim$450 and 650 m), because of multiple scattering of the aerosol particles. In the REF simulation, this enhancement is much smaller because of the strong aerosol absorption. As the concentrations of the chemical species are very high in this region, enhanced photolysis frequencies potentially strongly impact photochemical processes in the plume.

4.5 Photochemical Processes in a Biomass Burning Plume

In the following sections, results from the REF simulation for several trace gases are presented and compared to appropriate measurements. The focus is on compounds that are altered by chemical processes in the biomass burning plume. Especially the production of ozone and the formation of nitrogen reservoir species is investigated. Additionally, the oxidation efficiency in the plume is examined.

In order to interpret the results of such a three-dimensional model simulation, suitable quantities have to be defined that characterize the chemical processing and are good measures to compare different model simulations. For this purpose, three different types of quantities are used: absolute concentrations, correlations between different compounds, and photochemical reaction rates. While the first two quantities can be derived from measurements, the photochemical rates can only be extracted from model simulations.

To distinguish between dynamical and chemical processes, correlations between chemical compounds are regularly used in the analysis of measurements of plumes from biomass burning or other sources [e.g., *Andreae et al.*, 1988, 1994, 2001; *Parrish et al.*, 1993; *Mauzerall et al.*, 1996, 1998; *Reid et al.*, 1998; *Ryerson et al.*, 1998; *Goode et al.*, 2000]. In these analyses, simultaneous measurements of the mixing ratios of two compounds, X and Y, are used to perform a linear regression analysis. The slope of the regression line ($\Delta X/\Delta Y$) is the enhancement ratio within the polluted air mass relative to the background. In the present model study, the enhancement ratio between two species is calculated in the same way and can be compared to analyses based on observational data. For the investigation of biomass burning, enhancement ratios have been used to quantify the global emission of trace gases from vegetation fires from known emissions of CO and CO_2 [e.g., *Crutzen and Andreae*, 1990; *Andreae and Merlet*, 2001]. They have also been employed in photochemical studies, e.g., to estimate the photochemical production of ozone. A common enhancement ratio used in photochemical investigations is the $\Delta O_3/\Delta CO$ enhancement ratio that indicates the number of ozone molecules produced per emitted CO molecule [e.g., *Andreae et al.*, 1988, 1994; *Mauzerall et al.*, 1998].

From model simulations, photochemical reaction rates can be extracted. Two different quantities are used in the following sections. Averaged chemical reaction rates (molecule cm^{-3} s^{-1}) in the plume during the simulation time as well as temporal- and spatial-integrated rates are presented. The integrated rate gives the total number of molecules produced or destroyed by a specific chemical reaction in the plume during the simulation time of 90 min. From this quantity, the photochemical lifetime of a compound with respect to that reaction is derived by dividing its total emissions by its integrated chemical loss via this reaction.

4.5.1 Ozone

In this section, the simulated ozone concentration, the ozone enhancement ratio compared to CO, and the photochemical processes leading to the production of ozone are presented. In Figure 4.5, the simulated ozone mixing ratio after 90 min is shown for (a) one cross section along the main plume axis (Section A in Figure 4.3a), (b) one cross section across the plume (Section B in Figure 4.3a) and (c) one cross section at an altitude of 500 m. Above the fire, ozone is strongly depleted due to the fast reaction of ozone with NO, which is emitted from the fire. The NO_x mixing ratio above the fire exceeds the background O_3 mixing ratio (compare Table 4.3 and Table 4.4), resulting in a complete titration of the available ozone into NO_2.

Downwind the fire, the ozone concentration gradually increases due to photochemical processes. In Figure 4.5b, the simulated ozone mixing ratio across the plume after $\sim$40 min of traveling is presented. The ozone concentrations within

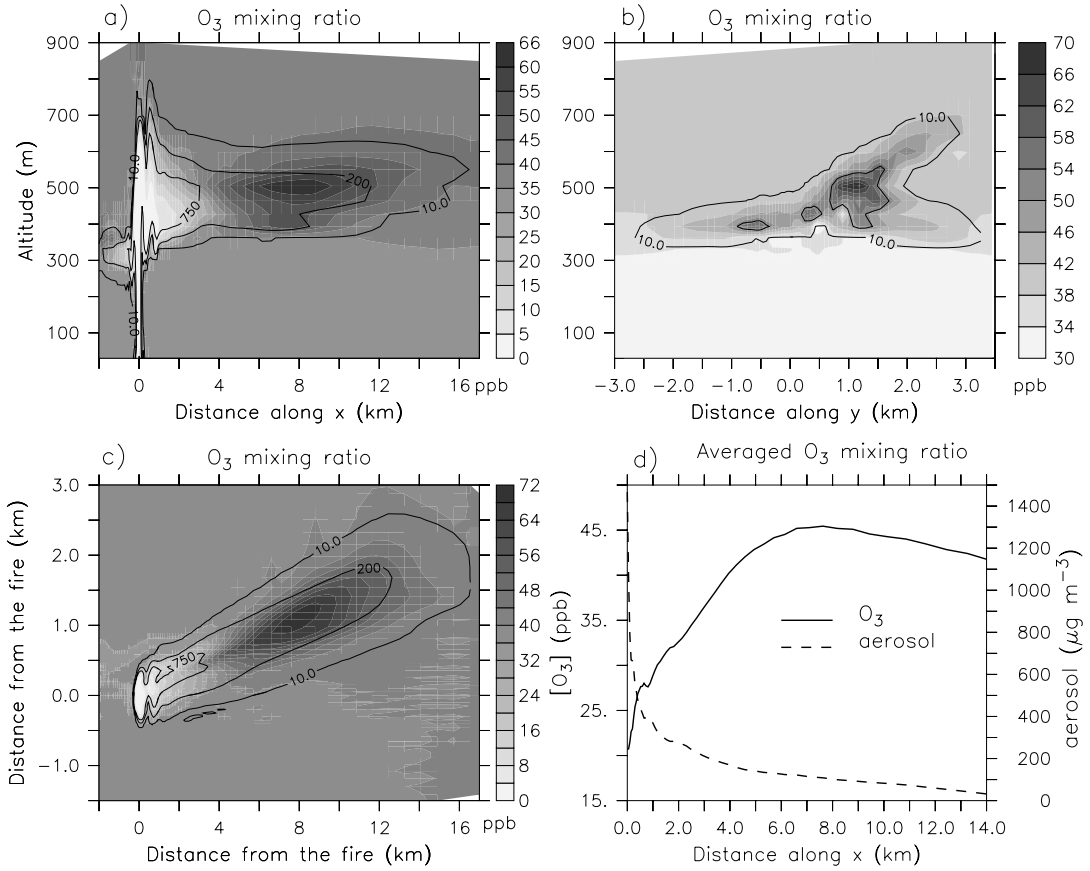

Figure 4.5: O_3 mixing ratio (color coding) for three cross sections through the model domain, at (a) the main plume axis, Section A, (b) x = 8.2 km, Section B, and (c) z = 500 m after 90 min of simulation time. The traveling time from the source to the cross section at a distance of 8.2 km is ∼40 min. Contour lines represent the aerosol mass concentration (μg m^{-3}). (d) Plume-averaged O_3 mixing ratio and aerosol mass concentration with distance from the fire.

the plume are well above background level, with the maximum values being correlated with the highest aerosol concentrations. At the end of the plume, ozone concentrations drop, because of the dilution with the background air and reduced photochemical production.

Figure 4.5d shows the plume-averaged ozone mixing ratio along the plume, together with the plume-averaged aerosol mass concentration. The aerosol concentrations gradually decrease with distance due to the time dependent emission and atmospheric dilution. The averaged ozone concentration along the plume increases up to a value of 45 ppb because of photochemical processes that lead to photochemical ozone production. The maximum and the averaged simulated ozone mixing ratio within the plume are 70 ppb and 40 ppb, respectively.

Measurements in young biomass burning plumes regularly show reduced ozone

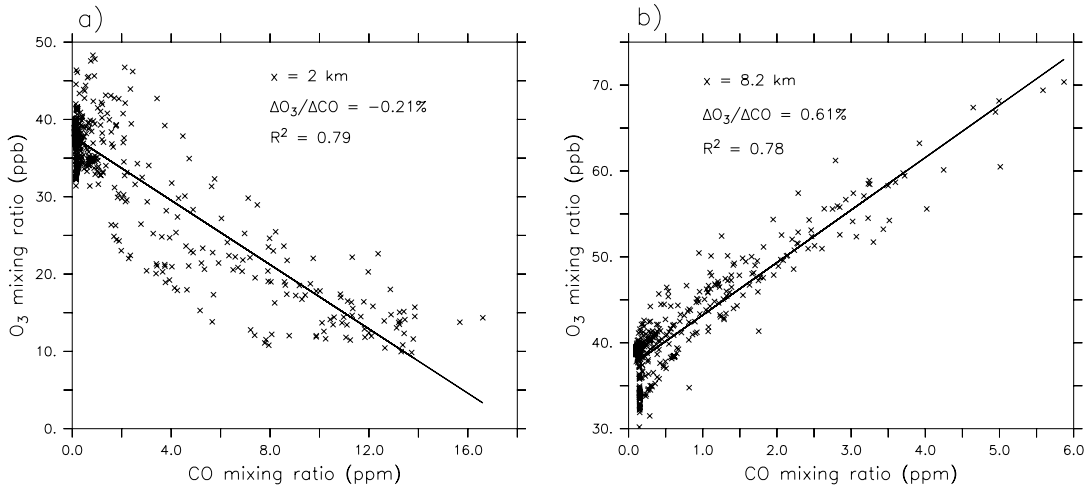

Figure 4.6: Scatter plot and linear regression between the CO and the O_3 mixing ratio in the plume at a distance of (a) 2 km and (b) 8.2 km from the fire after 90 min of simulation time. The elapsed time since the emission is $\sim$10 min and 40 min for distances of 2 km and 8.2 km, respectively.

concentrations close to the fire and enhanced ozone concentrations downwind the fire. Observations during the Quinault fire revealed a minimum ozone mixing ratio of $\sim$5 ppb above the fire, and a maximum of $\sim$80 ppb downwind the fire (see Figure 66.14 of *Hobbs et al.* [1996]). Comparable downwind ozone concentrations between 60 ppb and $\sim$150 ppb were observed in other biomass burning plumes [*Evans et al.*, 1974, 1977; *Stith et al.*, 1981; *Goode et al.*, 2000]. The simulated ozone concentration in the REF simulation therefore seems to be a good representation of the ozone concentration in young biomass burning plumes.

In Figure 4.6, the simulated mixing ratios of CO and O_3 at two cross sections across the plume at (a) x = 2 km and (b) x = 8.2 km are displayed in scatter plots. At both distances, the resulting R^2 from the linear regression analysis is larger than 0.6; the regression line is shown in the figures. Close to the fire (Figure 4.6a) the CO and O_3 concentrations are anticorrelated due to the reaction of ozone with the emitted NO. The $\Delta O_3/\Delta CO$ enhancement ratio is here -0.19%. Downwind the fire (Figure 4.6b) both species are positively correlated with an enhancement ratio of 0.66%, because of the photochemical production of ozone.

The $\Delta O_3/\Delta CO$ enhancement ratio as a function of distance from the fire is presented in Figure 4.7. Close to the fire, ozone and CO are anticorrelated. With increasing distance from the fire, the $\Delta O_3/\Delta CO$ ratio increases, indicating photochemical ozone production during the transport of the emissions. At a distance of 12 km from the fire, the enhancement ratio is 0.75%. Between 3 and 5 km, no linear correlation was found between CO and ozone.

Although the $\Delta O_3/\Delta CO$ enhancement ratio is often used as a measure for photo-

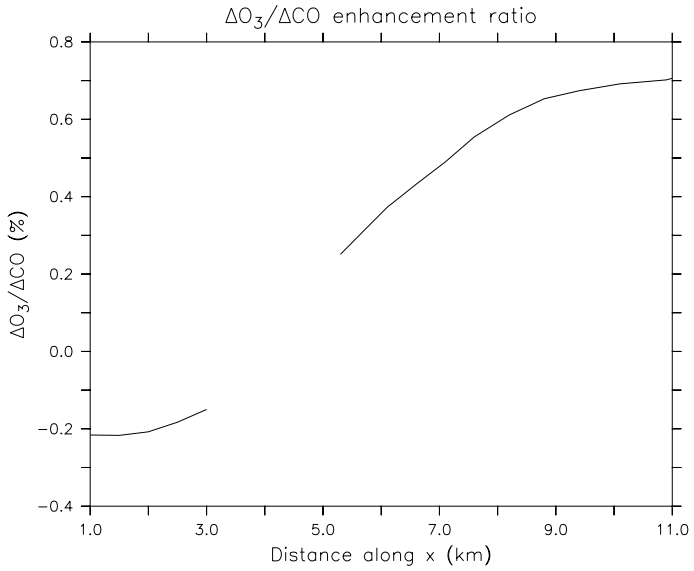

Figure 4.7: Evolution of the $\Delta O_3/\Delta CO$ ratio as a function of distance from the fire for the REF simulation. For the linear regression analysis, only grid cells between 300 m and 800 m altitude were taken into account. Only enhancement ratios with $R^2 > 0.6$ are displayed.

chemical ozone production from biomass burning [*Wofsy et al.*, 1992; *Andreae et al.*, 1988, 1994; *Mauzerall et al.*, 1996, 1998], information about this quantity in young plumes is very limited. Measurements in Africa during the FOS/DECAFE91 (Fire of Savannas/Dynamique et Chimie de l'Atmosphère en Forêt Equatoriale 91) experiment yielded $\Delta O_3/\Delta CO$ enhancement ratios from 1.2% to 16% with an average of 4% for biomass burning plumes a few hours after emission [*Helas et al.*, 1995]. A $\Delta O_3/\Delta CO$ enhancement ratio of $15 \pm 37\%$ was derived from measurements within 4 fresh plumes (less than half-a-day old) observed during the Transport and Atmospheric Chemistry Near the Equator-Atlantic (TRACE-A) expedition [*Mauzerall et al.*, 1998]. The relatively large standard error indicates that at least in one plume a significantly lower enhancement ratio than the average was observed. Recently, a $\Delta O_3/\Delta CO$ enhancement ratio of $7.9 \pm 2.4\%$ was derived from measurements within an Alaskan biomass burning plume $\sim$2 h traveling time downwind the fire [*Goode et al.*, 2000]. Within a second plume, no correlation between CO and O_3 was found, which was attributed to reduced UV radiation at the region of the sampling (300 m below the plume top).

The simulated value for the $\Delta O_3/\Delta CO$ enhancement ratio presented here ($\Delta O_3/\Delta CO = 0.75\%$), is smaller than all reported measurements so far. There are several possible reasons for the underestimation of the enhancement ratio by the model. These include different traveling times and different meteorological situations between the model scenario and the observations. Additionally, the averaged emission ratios or specific aerosol optical properties used in the simulations might be

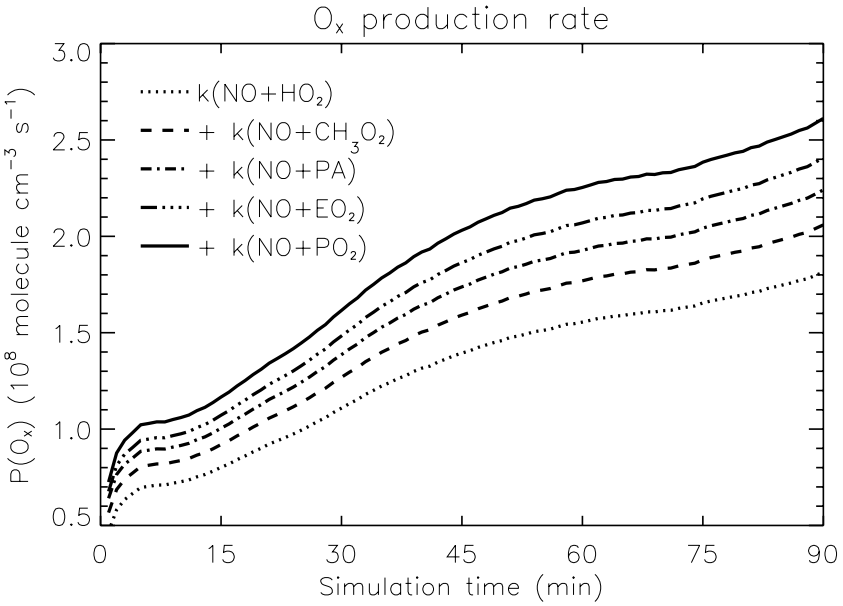

Figure 4.8: Plume-averaged reaction rates for the dominant O_x-producing chemical reactions over the simulation time. Shown are the cumulative reaction rates. The solid line represents the total O_x-production rate from all considered reactions.

responsible for the discrepancy. Limitations in the chemical reaction scheme might also be, in part, responsible for the underestimation of the $\Delta O_3/\Delta CO$ enhancement ratio by the model.

In order to quantify the simulated photochemical ozone production and to identify the main reactions in the model, the rates of the chemical reactions are analyzed. Ozone itself is produced and destroyed in numerous chemical reactions. Most of them are part of null cycles, without net production or destruction of ozone. In order to exclude these null cycles from budget analysis and to avoid numerical problems, the odd oxygen family, O_x, is often introduced in photochemical studies [e.g., *Crutzen et al.*, 1999]. The odd oxygen family includes all chemical compounds that are converted to ozone in fast chemical reactions. Production, $P(O_x)$ of the O_x-family is therefore equivalent to ozone production. In the present study, the odd oxygen family is defined as $O_x = O_3 + O(^1D) + O(^3P) + NO_2 + 2\,NO_3 + 3\,N_2O_5 + HNO_3 + HNO_4 + PAN + CH_3O_2NO_2$.

Photochemical O_x-production is dominated by the reactions of peroxy radicals, e.g., HO_2, with NO leading to the formation of NO_2 that is included in the O_x-family. Besides the hydroperoxy radical, HO_2, the methylperoxy radical, CH_3O_2, the peroxyacetyl radical, PA, the hydroxyethylperoxy radical, EO2, and the hydroxypropylperoxy radical, PO2, contribute to the ozone production. Figure 4.8 shows the

temporal development of the plume-averaged reaction rates for the O_x-production reactions. The relative contribution of each reaction to the O_x-production stays remarkably constant over time. The reactions of NO with HO_2 (69%), CH_3O_2 (10%), PA (7%), EO_2 (6%), and PO_2 (8%) account for nearly all of the photochemical ozone production. The contribution of the peroxy radicals from the alkenes, i.e., EO_2 and PO_2, to the total O_x-production exceeds the contribution of the methylperoxy radical, CH_3O_2. In the background atmosphere, only HO_2 and CH_3O_2 contribute significantly to the photochemical production of O_x [*Crutzen et al.*, 1999]. The average rate of O_x-production within the plume for the 90 min of simulation is 1.84×10^8 molecule cm^{-3} s^{-1} or ~ 25 ppb h^{-1}. The total number of photochemically produced O_x-molecules in the plume during the 90 min is 5.67×10^{27}. During the same time, 1.32×10^{28} molecules of NO_x are emitted from the fire (Table 4.2) yielding a photochemical production of O_x per emitted NO_x of 0.44 after 90 min.

It was shown that the model simulation realistically reproduces the ozone concentration in a young biomass burning plume. The simulated $\Delta O_3/\Delta CO$ enhancement ratio is slightly lower than observed in plumes from other fires. A significant amount of ozone is photochemically produced. This can be seen in the $\Delta O_3/\Delta CO$ enhancement ratio as well as in the analysis of the photochemical reaction rates.

4.5.2 Nitrogen Species

Nitrogen oxides (NO_x = NO + NO_2) play a critical role in tropospheric ozone chemistry. The NO_x concentration is the main determining factor if the oxidation of hydrocarbons produces or destroys ozone. The dependence of the photochemical ozone production on the NO_x concentration is highly nonlinear and depends on the available organic compounds [*Lin et al.*, 1988].

Atmospheric photochemical processing leads to the formation of nitrogen reservoir species NO_z (NO_z = HNO_3 + HNO_4 + HONO + PAN + $CH_3O_2NO_2$). These species are not directly linked to the formation of ozone, but act as a reservoir for nitrogen. Atmospheric transport of these reservoir species and subsequent release of the nitrogen, enhances the NO_x concentration and therefore the photochemical ozone production at remote locations and on a larger scale. The relative contributions of the single compounds to NO_z on the local scale is important for the regional impact of pollution, because of their different atmospheric residence times.

In Figure 4.9, the simulated mixing ratios of NO_x as well as the most abundant NO_z species, i.e., HNO_3, PAN, and HONO, are shown for the cross section along the plume. The NO_x concentration highly exceeds the NO_z concentration. Photochemical formation of NO_z only slightly decreases the NO_x concentration. As the nitrogen reservoir compounds are not emitted from the fire, their concentrations increase downwind the fire due to photochemical production in the plume.

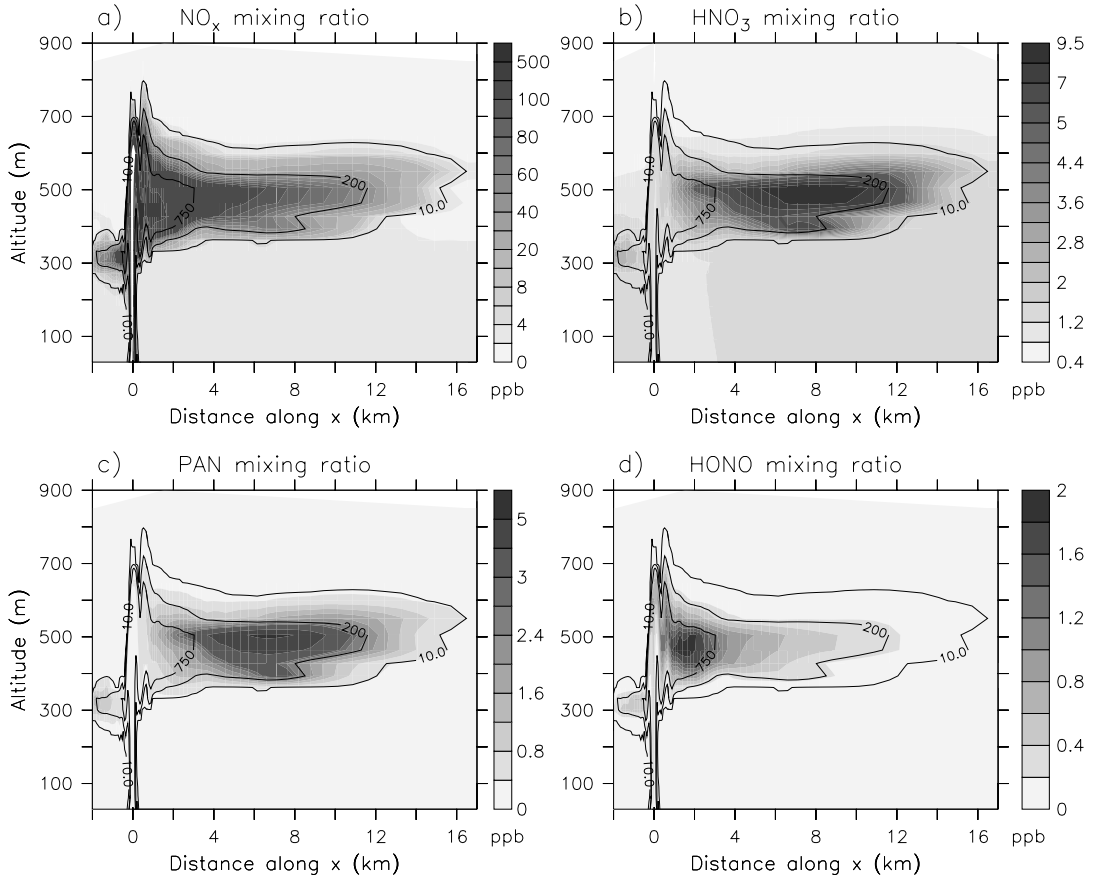

Figure 4.9: Mixing ratios of (a) NO_x and the most abundant NO_z species, i.e., (b) HNO_3, (c) PAN, and (d) HONO, along the main plume axis, Section A in Figure 4.3a, after 90 min. Contour lines represent the aerosol mass concentration (μg m^{-3}).

The maximum HONO concentration occurs closer to the fire than the maximum mixing ratios of HNO_3 and PAN (Figure 4.9). Production of HONO mainly occurs via the reaction of NO with OH ($\sim$97% of the total HONO production). Photolysis is the main loss process of HONO. Close to the fire, the [NO]/[NO_2] ratio is larger than one, because of the high initial ratio from the fire emission. Downwind the fire, this ratio decreases, because of higher ozone concentrations. Therefore, production of HONO is reduced downwind the fire. Additionally, destruction of HONO due to photolysis increases downwind due to the lower aerosol optical depth. As the production of HNO_3 and PAN requires NO_2, their photochemical production increases downwind relative to the production of HONO. While PAN establishes a thermal equilibrium with NO_2, the loss of HNO_3 is dominated by reaction with OH. This reaction is slow on the considered timescale and leads to the high HNO_3 concentrations.

Figure 4.10a shows the plume-averaged NO_x and NO_z mixing ratios as a function

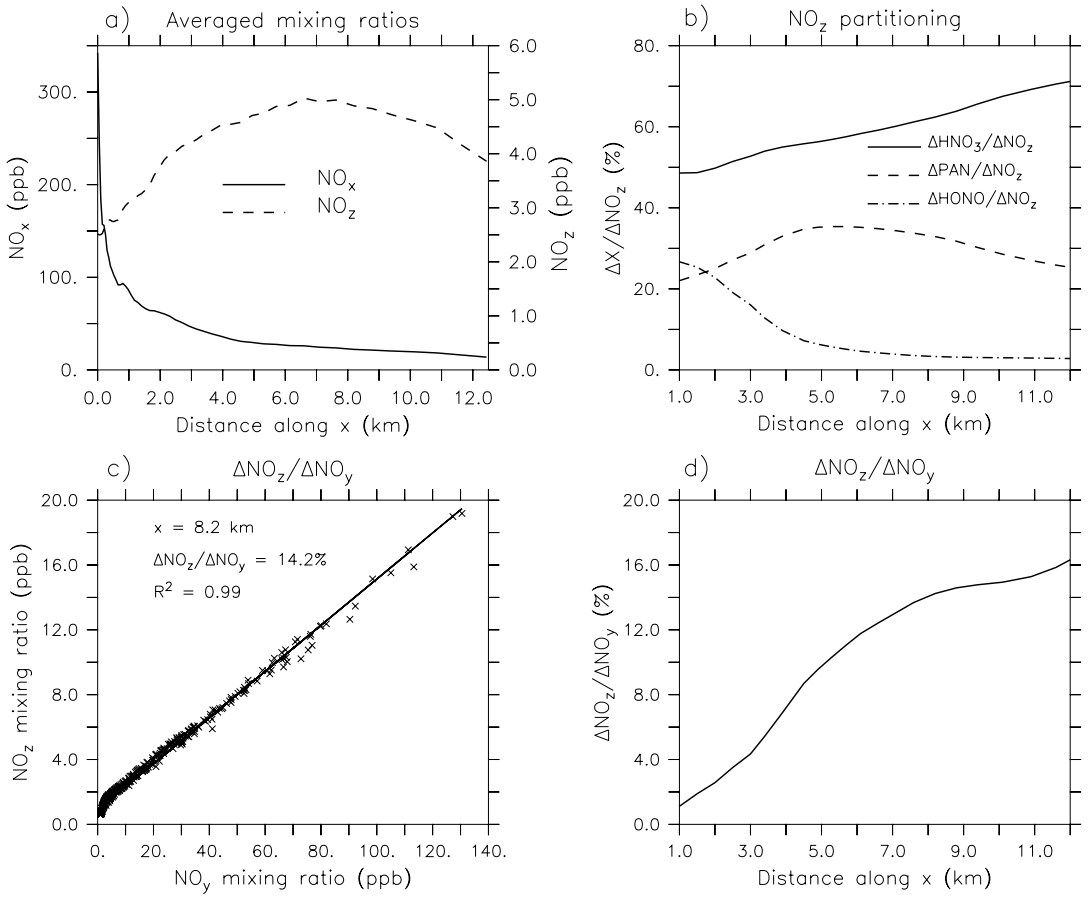

Figure 4.10: (a) Plume-averaged mixing ratio of NO_x and NO_z with distance from the fire after 90 minutes of simulation. (b) Partitioning of NO_z with distance from the fire, derived from linear correlations of HNO_3, PAN, and HONO with NO_z, respectively. (c) Scatter plot of the NO_y and NO_z mixing ratios at a distance of 8.2 km from the fire. Also included is the corresponding regression line with a slope of $\Delta NO_z/\Delta NO_y = 14.2\%$. (d) Enhancement ratio of $\Delta NO_z/\Delta NO_y$ with distance from the fire.

of distance from the fire. The maximum and average mixing ratios of NO_z in the plume after 90 min of simulation are 19.3 ppb and 4.1 ppb, respectively. The most abundant NO_z compound is HNO_3 with a simulated maximum mixing ratio of 12.3 ppb. The maximum mixing ratios of PAN, HONO, HNO_4, and $CH_3O_2NO_2$ are 6.4 ppb, 2.4 ppb, 326.0 ppt and 6.5 ppt, respectively.

Figure 4.10b presents the partitioning of NO_z between the most abundant individual compounds, HNO_3, PAN, and HONO, as a function of distance. This figure is produced from linear correlation analysis between the individual species and the total NO_z at different distances from the fire. The relatively high contribution of HONO close to the fire can also be seen in this figure. The most abundant NO_z compound in all regions of the plume is HNO_3. Its contribution to the total NO_z

increases from roughly 50% close to the fire, to around 70% at 12 km. The contribution of HONO with increasing distance decreases from around 25% at 1 km to less than 5% at a distance of 6 km. PAN contributes between 25% and 35% to the total NO_z.

In Figure 4.10c, the linear regression between the sum of the mixing ratios of all nitrogen species, NO_y ($NO_y = NO_x + NO_z$), and the NO_z mixing ratios at a distance of 8.2 km from the fire is presented. The slope of the regression line indicates that only 14.3% of the NO_y was transfered from the active nitrogen species, NO_x, into the reservoir species, NO_z. The major part of NO_y is still present in the form of NO_x. This $\Delta NO_z/\Delta NO_y$ enhancement ratio can be used as a measure of the photochemical age of a plume or an air mass [*Marion et al.*, 2001]. At the fire, NO_z is close to zero and increases downwind the plume, when photochemistry converts NO_x into NO_z. This behavior is documented in Figure 4.10d, where the change of the simulated $\Delta NO_z/\Delta NO_y$ ratio with distance from the fire is shown. The contribution of NO_z to the NO_y mixing ratio increases steadily with distance from the fire reaching a value of 16% at 12 km downwind the fire.

Measurements of HNO_3, PAN, or other compounds of the NO_z-family in young biomass burning plumes are rare. Observations in plumes from three prescribed fires yielded mean mixing ratios for HNO_3 of 14.6±14.7 ppb, 40.7±34.1 ppb, and 44.6±33.1 ppb, respectively [*LeBel et al.*, 1988, 1991], larger than the simulated maximum mixing ratio of 12.3 ppb. Those high concentrations and the good correlation with CO_2 in the observations indicate primary emission of HNO_3 from these fires, but this emission is neglected in the model simulations as explained in Section 4.2.2. During the Arctic Boundary Layer Experiment (ABLE-3B), a young biomass burning plume was found with mixing ratios of HNO_3 and PAN of $\sim$700 ppt and $\sim$300 ppt, respectively, at low altitude [*Lefer et al.*, 1994; *Singh et al.*, 1994]. Although the simulated mixing ratios are larger than these observations, the measured HNO_3/PAN ratio of around 2.2 agrees fairly well with the modeled value of 1.9. From measurements performed during TRACE-A, a HNO_3/PAN ratio of 0.3 for "fresh plumes" (younger than 12 hours) was calculated [*Mauzerall et al.*, 1998]. As this analysis is based on measurements performed between 1 km and 4 km altitude, higher than the simulations, a comparison with the simulations is not straightforward. Processes during the vertical transport, e.g., scavenging of the HNO_3 by water droplets, as well as the colder temperatures at higher altitudes, might be responsible for the lower HNO_3/PAN ratio in these observations. Overall one can conclude that there are not enough appropriate measurements to evaluate the model results for the nitrogen reservoir species. However, the few available measurements do not contradict the model results.

From the model simulations, the following values for the photochemical produc-

tion of NO_z can be derived. The average net production rate of NO_z, i.e., $P(NO_z) - L(NO_z)$, in the plume is 2.82×10^7 molecule cm^{-3} s^{-1}. In total, 8.42×10^{26} molecules of NO_z were netto photochemically produced within the plume during the simulation time of 90 min, with contributions from HNO_3, PAN, and HONO of 61%, 29%, and 7%, respectively. Together with the number of photochemically produced O_x-molecules presented in Section 4.5.1, the number of O_x-molecules produced per number of NO_x-molecules oxidized, i.e., per number of NO_z-molecules formed, is calculated to 6.7. This value corresponds to the ozone production efficiency (OPE) that describes the number of produced ozone molecules per number of produced NO_z molecules [*Liu et al.*, 1987; *Trainer et al.*, 2000; *Marion et al.*, 2001]. The OPE depends mainly on the chemical composition, especially on the NO_x concentration, of the air mass [*Liu et al.*, 1987; *Lin et al.*, 1988]. For the polluted boundary layer, OPE values range between 1 and 5, for rural conditions they are about 10, and increase to up to 100 in the remote boundary layer and free troposphere [*Jenkin and Clemitshaw*, 2000, and references therein]. The value of 6.7 is on the lower limit of the values reported from observations within the planetary boundary layer over Central Africa during the burning season (6.3 to 14.8) [*Marion et al.*, 2001]. The simulated lifetime of NO_x with respect to the formation of HNO_3 and PAN is 9.9 h. This lifetime compares well to observations in urban and in power plant plumes [*Spicer*, 1982; *Ryerson et al.*, 1998; *Sillman*, 2000].

4.5.3 Oxidizing Efficiency

Radicals, e.g., OH, HO_2 and other peroxy radicals, are essential for atmospheric photochemistry. Atmospheric oxidation of organic molecules occurs mainly by reaction with the OH radical. As the OH radical is formed back in catalytic cycles, even a small concentration of OH in the order of 10^6 molecule cm^{-3} has a substantial impact on atmospheric chemistry [*Crutzen et al.*, 1999]. Within these cycles, the peroxy radicals are responsible for the photochemical formation of ozone. Especially under the conditions of a biomass burning plume, i.e., high concentrations of NO_x and organic compounds, these catalytic cycles are very effective.

In Figure 4.11 the mixing ratios of (a) OH, (b) HO_2, (c) CH_3O_2, and (d) the sum of other peroxy radicals RO_2 along the plume are presented after a simulation time of 90 min. The concentration of RO_2 is dominated by the peroxy radicals from ethene and propene, EO_2 and PO_2, respectively. Above the fire, the concentrations of all radicals are close to zero in the plume. Downwind, the OH, HO_2, and CH_3O_2 concentrations in the plume are smaller than outside the plume, whereas the RO_2 concentration reaches its maximum value inside the plume. High NO_x concentrations are responsible for the enhanced photochemical removal of the radicals inside the plume, leading to the formation of several ppb of HNO_3, PAN, and HONO (Fig-

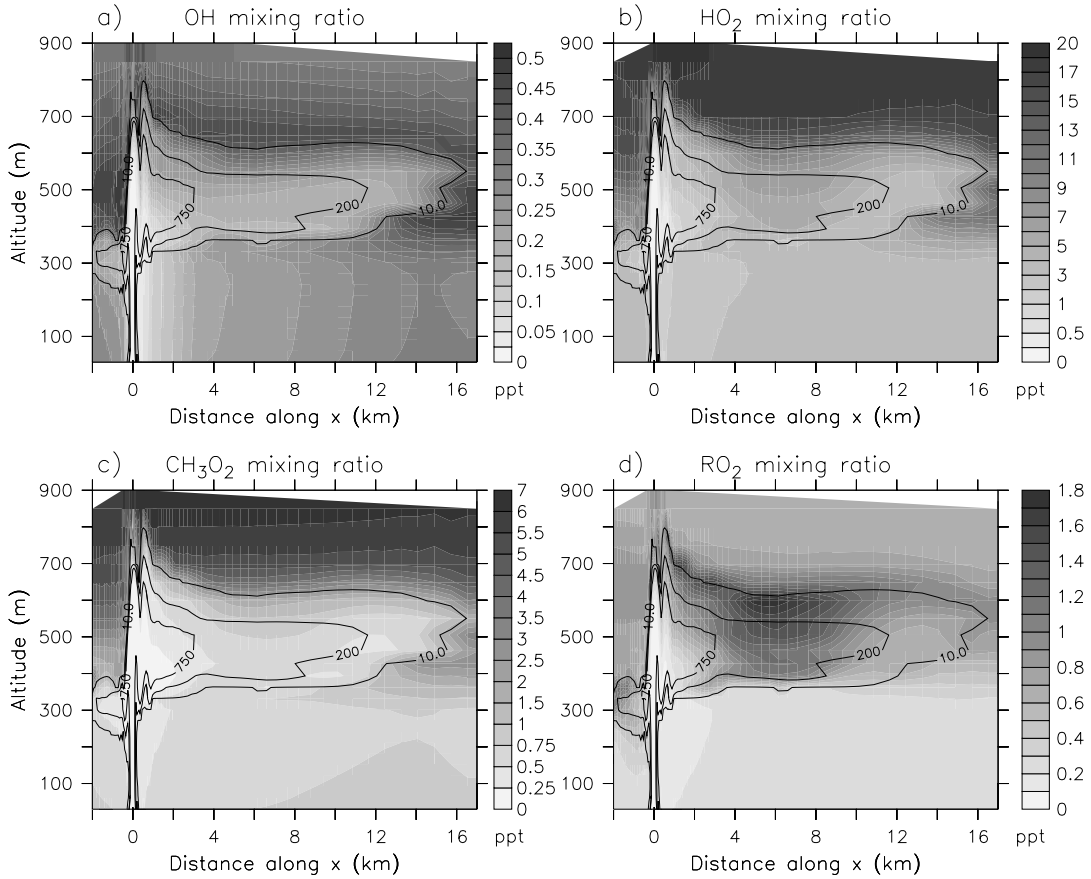

Figure 4.11: Simulated mixing ratios of (a) OH, (b) HO_2 (c) CH_3O_2, and (d) the sum of other peroxy radicals RO_2, RO_2 = PA + $C_2H_6O_2$ + EO_2 + PO_2 + $ACETO_2$) after 90 min along the plume at y = 100 m. Contour lines represent the aerosol mass concentration (μg m^{-3}).

ure 4.9). In the cases of OH, HO_2, and CH_3O_2, these enhanced losses compared to the background cannot be compensated by enhanced production. However, in the case of RO_2, the concentrations of the precursors, i.e., mainly ethene and propene, are highly elevated inside the plume. Additional photochemical production of RO_2 overcomes the enhanced photochemical destruction, and results in maximum concentrations of RO_2 inside the plume. The average mixing ratios of OH and HO_2 inside the plume after 90 min are 0.24 ppt and 4.92 ppt, respectively.

The oxidation efficiency is a quantity to describe the amount of atmospheric photochemical oxidation. In order to derive the oxidation efficiency from concentrations of species, transport and chemical processes have to be separated. This is performed by investigating the enhancement ratio between two compounds that are emitted from the fire. The reference compound should not be influenced by oxidation, and atmospheric dilution should be similar for both compounds. CO is well suited as

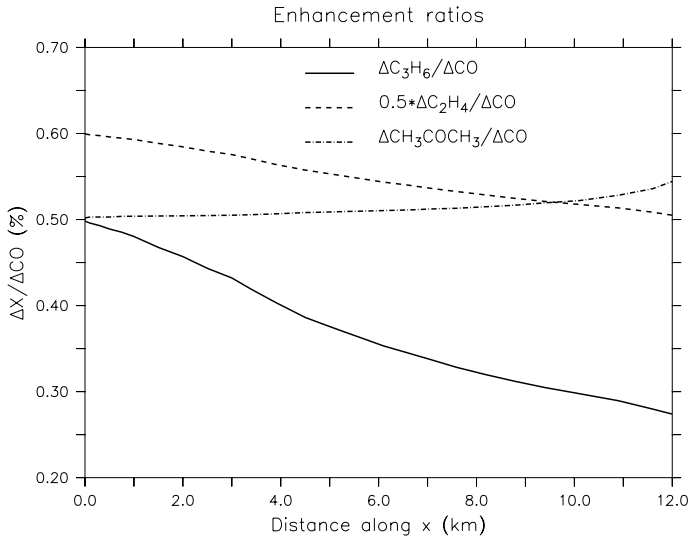

Figure 4.12: Enhancement ratios between C_2H_4, C_3H_6, and CH_3COCH_3 and CO as a function of distance from the fire after 90 minutes of simulation. Note that the $\Delta C_2H_4/\Delta CO$ enhancement ratio is divided by a factor of 2.

a reference compound on the timescale considered here. The concentration of the species of interest has to be significantly affected by the reaction with OH during the 90 min of simulation. Alkenes are well suited for this purpose, e.g., propene, because their lifetimes against reaction with OH is in the order of some hours in the boundary layer [*Jenkin and Clemitshaw*, 2000]. Significant oxidation of alkenes and the reduction of their concentration due to photochemistry is expected to occur during the simulation. The $\Delta C_3H_6/\Delta CO$ and $\Delta C_2H_4/\Delta CO$ emission ratios at the fire are 0.5% and 1.2%, respectively (Table 4.1). At the source, the emission ratio is identical to the enhancement ratio.

In Figure 4.12, the enhancement ratios between propene (C_3H_6) and CO, ethene (C_2H_4) and CO, and, for comparison, between acetone (CH_3COCH_3) and CO are presented. The enhancement ratio between acetone and CO stays roughly constant along the plume, pointing to relatively few photochemical processes that influence the concentrations of these compounds. The slight increase after a distance of 10 km is explained by different dilution efficiencies of CO and acetone, due to relatively high acetone background concentrations. In contrast, $\Delta C_2H_4/\Delta CO$ and $\Delta C_3H_6/\Delta CO$ decrease almost linearly with increasing distance from the fire. This change in the enhancement ratio represents the different reactivities of the alkenes against OH oxidation as compared to CO and can be used as a measure for the oxidation efficiency in the plume.

Observations during SCAR-B yielded a $\Delta C_3H_6/\Delta CO$ enhancement ratio in young smoke plumes (less than 4 minutes after emission) of 0.39% [*Reid et al.*, 1998]. For

compound	total number (molecule)	lifetime
CO	9.98×10^{26}	16.8 d
C_2H_6	7.15×10^{24}	16.4 d
C_2H_4	3.62×10^{26}	13.4 h
C_3H_6	4.61×10^{26}	4.4 h

Table 4.5: Integrated number of molecules oxidized by OH in the plume and lifetime against oxidation with OH during the simulation time of 90 min.

measurements in aged regional haze, this ratio decreased to a value of 0.028% [*Reid et al.*, 1998]. During TRACE-A, the $\Delta C_3H_6/\Delta CO$ enhancement ratio could only be determined for fresh plumes (0.12%). In recent (<1 day old) plumes, however, no correlation between propene and CO was found [*Mauzerall et al.*, 1998]. For ethene, the enhancement ratio compared to CO decreased from 0.69% in fresh plumes to 0.13% in recent plumes. In more aged biomass burning plumes, no correlation between ethene and CO was found. From measurements in a young Alaskan biomass burning plume, a slight reduction of $\Delta C_2H_4/\Delta CO$ from an initial value of 1.9% to a value of $1.6 \pm 0.2\%$ after ~ 2.2 hours of traveling was observed [*Goode et al.*, 2000]. These observations support the simulation results showing a significant photochemical oxidation of alkenes in the plume on the timescale of hours. The reduction of the $\Delta C_2H_4/\Delta CO$ enhancement ratio observed in the Alaskan plume (reduction by $\sim 15\%$) is comparable to the simulated reduction of $\sim 16\%$. It can be concluded that oxidation of alkenes and therefore the oxidation capacity in the plume seems to be reasonably well described in the presented model simulation.

Within a model, different processes are much easier to separate than from observations, and the oxidation efficiency can be derived as the inverse of the lifetime of hydrocarbons against oxidation by OH [*Lawrence et al.*, 2001]. In Table 4.5, the number of molecules oxidized by OH during the simulation time within the plume for selected NMHCs are presented. Additionally, their calculated lifetime against oxidation with OH is given. The total number of oxidized molecules reflects the concentration of the species, as well as its rate constant for the reaction with OH. Due to its high concentration, the total number of oxidized CO molecules exceeds the oxidation of the other hydrocarbons. However, compared to the total emission of CO, oxidation by OH is negligible. This can be seen in the relatively long lifetime of CO compared to the simulation time. For C_2H_6 the situation is similar. In the case of the alkenes, oxidation by OH removes a significant number of molecules as compared to the total emissions. The photochemical lifetimes of alkenes are of the same scale as the simulation time. Therefore, photochemistry affects alkene con-

centration in the plume, as already shown in the previous paragraph. Compared to 'typical lifetimes' [*Jenkin and Clemitshaw*, 2000], the lifetimes presented here are shorter, because the OH concentrations used in the general calculations are diurnaly averaged values, which are generally lower than the instantaneous value used here. These lifetimes are good quantitative indicators for the photochemical activity and will be used for a comparison of the different sensitivity simulations in the next sections.

In the following, the main sources and sinks of the radicals will be investigated. For this purpose, the HO_x-family is defined in order to exclude the fast chemical reactions involved in null cycles: HO_x = OH + HO_2 + CH_3O_2 + $C_2H_6O_2$ + EO_2 + EO + PO_2 + $CH_3COCH_2O_2$ + PA + GCO3 + HNO_4 + HONO + $CH_3O_2NO_2$ + PAN. For the definition of EO_2, EO, PO_2, PA, and GCO3 the reader is referred to table A.1. Besides the radicals, also some compounds of the NO_z-family are included. Under boundary-layer conditions, these compounds (e.g., PAN, HNO_4, HONO, and $CH_3O_2NO_2$) do not act as a permanent sink for the radicals.

The photochemical production of the HO_x-family, $P(HO_x)$, in the plume is dominated by the photolysis of formaldehyde, which accounts for 83.1% of the total HO_x-production. Additional contributions come from the photolysis of acetaldehyde (7.9%), the reaction $O(^1D)$ + H_2O (4.7%), and the ozonolysis of propene (2.4%). On a global scale, the reaction of $O(^1D)$ with H_2O dominates the HO_x-production, accounting for roughly 50% of the HO_x production [*Crutzen et al.*, 1999]. However, photolysis of HCHO and other aldehydes can be the most important source for HO_x radicals, also under urban-polluted conditions [*Jenkin and Clemitshaw*, 2000]. The photochemical loss of HO_x, $L(HO_x)$, under the conditions of a biomass burning plume is dominated by the reaction of OH with NO_2 which accounts for 97.9% of the total HO_x loss. Because PAN is included in the HO_x-family in the present investigation, its formation is no loss of HO_x. The self reaction of HO_2 and the reaction of HO_2 with CH_3O_2, which are significant in the global atmosphere, are only of minor importance under these conditions. No enhanced concentrations of hydroperoxides are found in the simulations.

Direct emission of HCHO from the fire is the dominant source of HCHO, accounting for 1.21×10^{28} molecules (Table 4.2). Secondary formation of formaldehyde due to the oxidation of hydrocarbons accounts for an additional 1.65×10^{27} molecules of HCHO (12% of the total) in the plume. The dominant reactions that account for this secondary production of formaldehyde are CH_3O_2 + NO (32%), EO_2 + NO (11%), EO + NO (24%), and PO_2 + NO (28%). As for the photochemical ozone production presented in Section 4.5.1, the important role of the alkenes for the photochemistry in young biomass burning plumes is also reflected in their large contribution to secondary HCHO formation.

In the previous sections, the concentrations of ozone, nitrogen oxides, radicals, and enhancement ratios of hydrocarbons from the REF simulation were presented and compared with appropriate observations. Although measurements for comparison are rare, the model results seem to be a realistic description of the chemical processes in a young biomass burning plume. The photochemical ozone production and the formation of reactive nitrogen species were quantified for the presented scenario. The oxidation efficiency was estimated by the lifetime of hydrocarbons and the importance of formaldehyde as the major source of radicals was pointed out.

4.6 Sensitivity Studies

In this section, three sensitivity studies are presented and their results are compared to the results from the reference simulation.

In the NO OVOC model simulation, the emission of oxygenated volatile organic compounds (OVOC), i.e., HCHO, CH_3CHO, CH_3OH, HCOOH, CH_3COOH, and CH_3COCH_3, have been omitted. This scenario considers the fact, that emission of these compounds was only recently found in laboratory experiments as well as in field observations [e.g. *Andreae et al.*, 1996a; *Yokelson et al.*, 1997; *Koppmann et al.*, 1997; *Yokelson et al.*, 1999; *Holzinger et al.*, 1999; *Goode et al.*, 2000; *Friedli et al.*, 2001]. The values of their emission factors are still uncertain. Emission of these compounds from biomass burning was included only recently in global model simulations [*Wang et al.*, 1998a; *von Kuhlmann*, 2001]. A recent box model study showed the importance and complex effects on ozone production of the oxygenated compounds in a biomass burning plume [*Mason et al.*, 2001].

The LOW NOX scenario investigates the impact of a different $\Delta NO_x/\Delta CO_2$ emission ratio. Because the nitrogen emission ratio depends on the nitrogen content of the fuel, the emissions vary between different ecosystems. The emission factors for fires in savanna and tropical forest differ by more than a factor of 2 [*Andreae and Merlet*, 2001]. These differences have a potential impact on the photochemistry occurring in biomass burning plumes. For the LOW NOX simulation, the $\Delta NO_x/\Delta CO_2$ emission ratio was reduced from 0.2% used in the REF simulation to 0.15%.

The NO ABS scenario investigates the impact of aerosol absorption on the photochemical processes in a biomass burning plume. Aerosol absorption is one of the major uncertainties in the characterization of the atmospheric aerosol, especially as measurements are rare and uncertain [*Heintzenberg et al.*, 1997]. Previous studies already presented the impact of aerosol absorption and scattering on the ozone production in different scenarios [*Dickerson et al.*, 1997; *He and Carmichael*, 1999]. In the NO ABS simulation, the single-scattering albedo of the aerosol was set to unity

at all wavelengths, resulting in a conservative, non-absorbing aerosol. The use of conservative scattering might not be appropriate for dry biomass burning aerosol. However, considerable uncertainty exists for the single-scattering albedo of biomass burning aerosol as shown in section 2.7. Additionally, the optical properties of clouds, which are often formed above vegetation fires, are much better characterized by conservative scattering than by the relative high absorption of the dry aerosol used in the REF simulation.

In the following sections, the results of the simulation of ozone, nitrogen oxides and the oxidation efficiency from the different simulations will be shown. The discussion of these results will be presented in a separate section.

4.6.1 Ozone

In this section, the simulated ozone concentrations and the photochemical production rates in the different scenarios will be presented.

Figures 4.13a–c display the ozone mixing ratios for the three sensitivity studies along the main plume axis. In the NO OVOC simulation (Figure 4.13a), the simulated ozone concentration in the plume stays below background level at all distances from the fire, although a slight increase with distance from the fire is simulated. The ozone concentration of the LOW NOX (Figure 4.13b) and NO ABS (Figure 4.13c) simulations show highly elevated ozone concentrations inside the plume as compared to the background. The ozone mixing ratios also exceed the results from the REF simulation. This is more clearly seen in Figure 4.13d, where the plume averaged ozone mixing ratio along the plume is shown for the REF and the three sensitivity simulations. The NO OVOC simulation lies well below all other model runs while the results from the NO ABS and LOW NOX simulations exceed the reference simulation at all distances from the fire. Close to the fire, the NO ABS simulation results in the highest averaged ozone concentration whereas downwind of 6 km the LOW NOX scenario simulates the highest ozone values.

The results of the different simulations for ozone are summarized in Table 4.6. Here, the maximum and the plume-averaged ozone mixing ratios, the average O_x-production rate as well as the total number of photochemically produced O_x-molecules are presented. In the NO OVOC simulation, $P(O_x)_{\mathrm{ave}}$ is nearly an order of magnitude smaller than in the other simulations resulting in a $\sim$30% smaller ozone concentration. In the LOW NOX and NO ABS simulation the photochemical ozone production is larger than in the REF simulation, leading to $\sim$10% higher ozone concentrations. Although the production of O_x is $\sim$20% larger in the NO ABS than in the LOW NOX simulation, the averaged ozone concentrations are very similar.

From the previous analysis, the following can be concluded: The emissions of

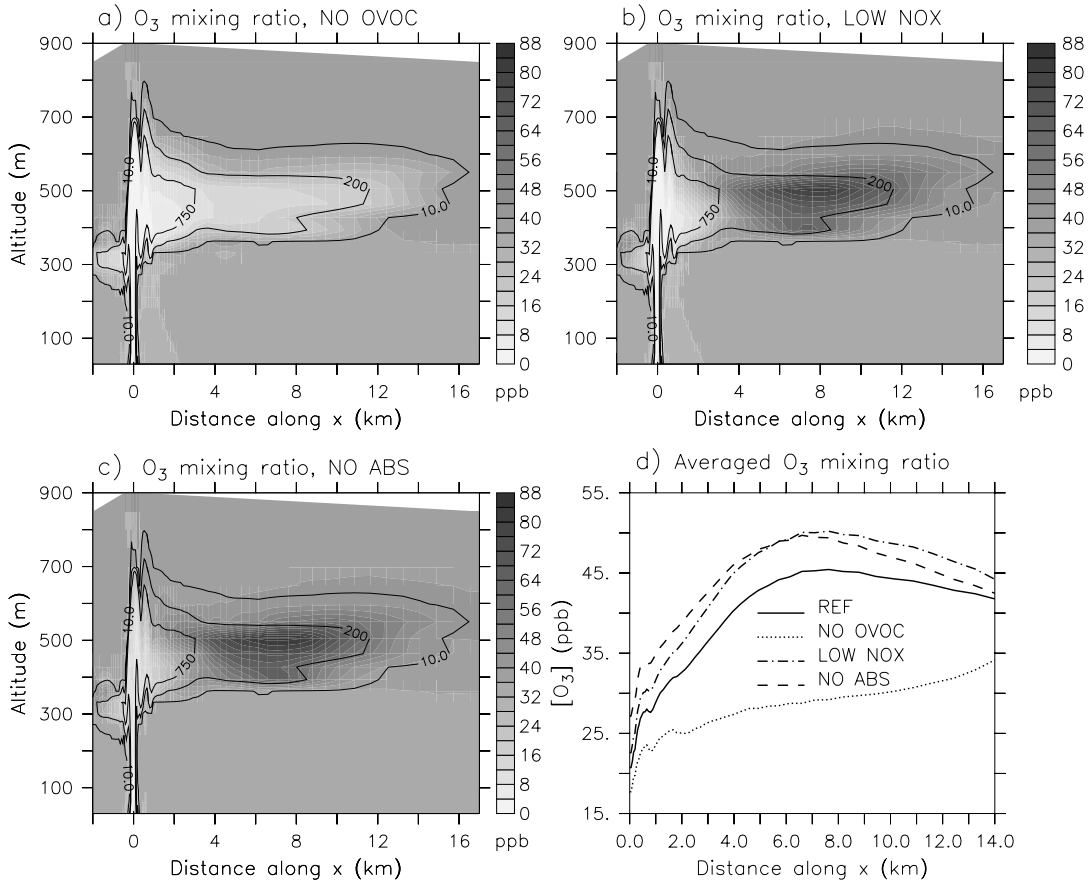

Figure 4.13: O_3 mixing ratio (color coding) for three sensitivity simulations for the cross section along the main plume axis (Section A in Figure 4.3a). (a) NO OVOC, (b) LOW NOX, (c) NO ABS. Note that the color scale is extended compared to the one used in Figure 4.5a. Contour lines represent the aerosol mass concentration (μg m^{-3}). (d) Plume-averaged O_3 mixing ratios for the reference and the sensitivity simulations with distance from the plume.

	$[O_3]_{ave}$ (ppb)	$[O_3]_{max}$ (ppb)	$P(O_x)_{ave}$ (molecule cm^{-3} s^{-1})	$P(O_x)_{tot}$ (molecule)
REF	39.4	70.4	1.84×10^{8}	5.67×10^{27}
NO OVOC	28.0	59.1	2.70×10^{7}	7.52×10^{26}
LOW NOX	43.4	91.4	2.01×10^{8}	6.13×10^{27}
NO ABS	43.6	92.3	2.40×10^{8}	7.51×10^{27}

Table 4.6: Averaged and maximum value for the O_3 mixing ratio from the 4 simulations. Additionally the plume-averaged O_x-production rate and the total number of O_x produced within the 90 minutes of simulation are shown.

OVOCs have significant impact on the simulation of the ozone concentration in a young biomass burning plume. Neglecting their emission leads to unrealistically low ozone concentrations due to an underestimation of the photochemical ozone production. Reduced NO_x emissions lead to an increased photochemical O_x-production and ozone concentrations. The absorbing properties of the aerosol have a substantial effect on the simulated ozone concentration, leading to enhanced concentrations for the case of a non-absorbing aerosol. Especially close to the fire, at high aerosol and NO_x concentrations, multiple scattering enhances photolysis frequencies, photochemical ozone production, and ozone concentrations.

4.6.2 Nitrogen Species

In this section, results for the nitrogen reservoir species, NO_z, from the sensitivity studies are presented and compared to the REF simulation.

The sums of the mixing ratios of the NO_z-compounds for the three sensitivity studies are displayed in Figures 4.14a–c for the cross section along the main plume axis. Additionally, Figure 4.14d shows the plume-averaged mixing ratios along the distance from the fire for all 4 simulations. In the NO OVOC simulation, Figure 4.14a, only a small enhancement of NO_z compared to the background is observed downwind of the fire. The highest NO_z mixing ratio is observed in the NO ABS simulation, Figure 4.14c, with a maximum value inside the plume of 24.4 ppb. The increase of the NO_z concentration inside of the plume begins much closer to the fire in the NO ABS than in all other simulations. This is especially obvious in the averaged mixing ratio shown in Figure 4.14d. The NO_z mixing ratios calculated in the LOW NOX and the REF simulations show very close agreement; the values from the LOW NOX simulations slightly exceed the REF simulation.

The results for the nitrogen reservoir species are summarized in Table 4.7. The maximum and the average NO_z mixing ratios are presented, reflecting the results shown in Figure 4.14d with low values in the NO OVOC simulation and the highest values in the NO ABS simulation. The same trend is reflected in the photochemical production of NO_z, $P(NO_z)$. Note, that $P(NO_z)$ denotes the net production of NO_z. The relative contribution of $P(HNO_3)$ to $P(NO_z)$ differs between the scenarios. The highest relative contribution of HNO_3 is simulated in the NO OVOC calculation, however the total amount of NO_z is very small. The partitioning of NO_z in the REF and NO ABS simulation is similar, although the absolute value of NO_z differs by roughly 20%. In the case of the LOW NOX simulation, the mixing ratio of NO_z is close to that of the REF simulation, but the contribution of HNO_3 is lower. The photochemical lifetime of NO_x against formation of HNO_3 and PAN, is strongly enhanced when OVOC emissions from the fire are neglected. Lower NO_x emission and higher photolysis frequencies lead to a slight reduction in the photochemical lifetime of NO_x.

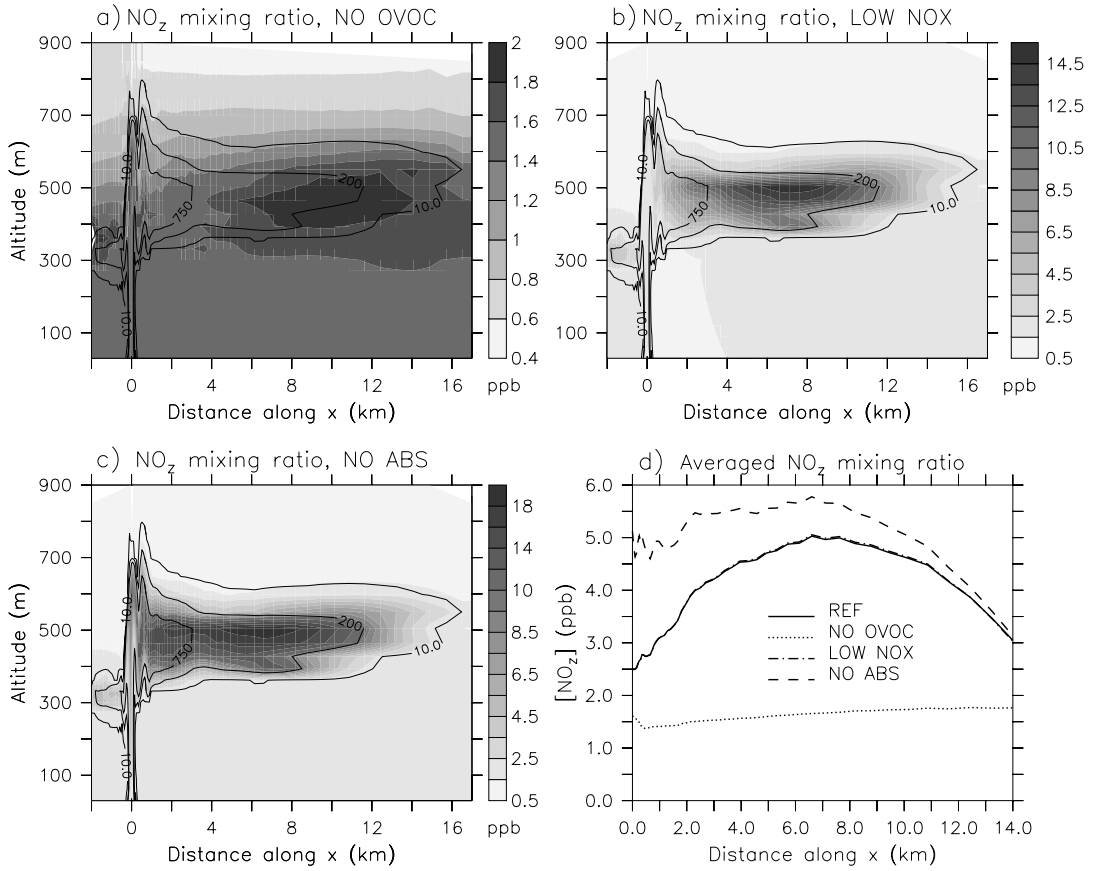

Figure 4.14: NO_z mixing ratio (color coding) for three sensitivity simulations for the same cross section along the main plume axis, Section A in 4.3a, (a) NO OVOC, (b) LOW NOX, (c) NO ABS. Note that the color scale changes from plot to plot. Contour lines represent the aerosol mass concentration (μg m^{-3}). (d) Plume-averaged NO_z mixing ratios for the reference and the sensitivity simulations with distance from the plume.

	$[NO_z]_{ave}$ (ppb)	$[NO_z]_{max}$ (ppb)	$P(NO_z)$ (molecule cm^{-3} s^{-1})	$P(HNO_3)$ (% of $P(NO_z)$)	$\tau(NO_x)$ (h)
REF	4.2	19.3	2.82×10^7	61.0	9.9
NO OVOC	1.6	3.2	5.06×10^6	84.3	19.8
LOW NOX	4.2	19.8	2.83×10^7	56.1	9.5
NO ABS	5.0	24.4	3.58×10^7	60.1	7.7

Table 4.7: Average and maximum value for the NO_z mixing ratio from the 4 simulations. Additionally the average rates of the net production of NO_z in the plume, $P(NO_z)$, during the 90 min of simulation are presented. The contribution of the net production of HNO_3, $P(HNO_3)$, to $P(NO_z)$ and the lifetime of NO_x against formation of HNO_3 and PAN are presented.

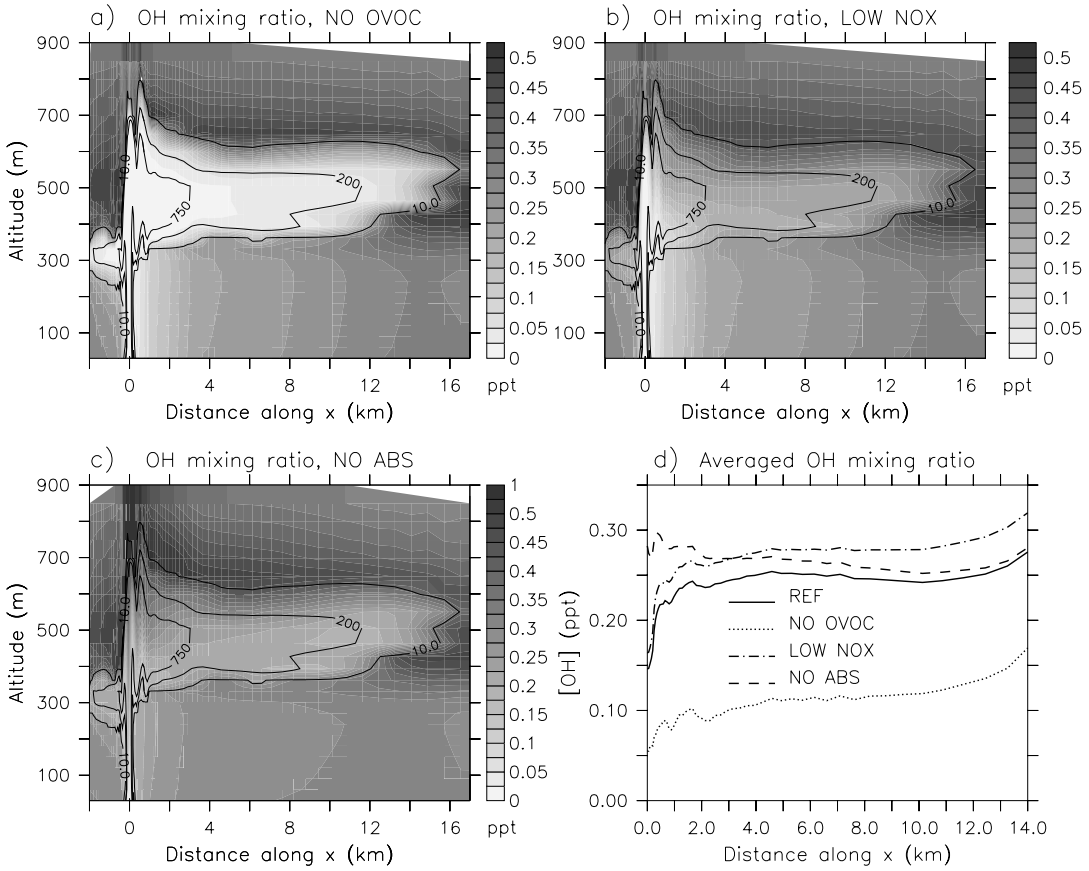

Figure 4.15: OH mixing ratio (color coding) for three sensitivity simulations along the main plume axis, Section A in Figure 4.3a. (a) NO OVOC, (b) LOW NOX, (c) NO ABS. Contour lines represent the aerosol mass concentration (μg m^{-3}). Note the extended scale in (c). (d) Plume-averaged OH mixing ratios for the reference and the sensitivity simulations as a function of distance from the plume.

4.6.3 Oxidizing Efficiency

In the following section, the model results for the oxidizing efficiency are presented. In Figures 4.15a–c, the OH mixing ratios along the main plume axis are displayed for the three sensitivity studies. Figure 4.15d presents the plume-averaged OH mixing ratios for all four simulations as a function of distance. The OH concentration in the NO OVOC simulation is significantly lower than that in all other simulations. The results from the NO ABS and the LOW NOX simulation exceed the REF simulation. The average OH mixing ratio from the LOW NOX simulation follows the REF simulation along the plume at a higher level. The NO ABS simulation is significantly larger close to the fire and decreases to the value of the REF simulation at a distance of 14 km from the fire.

In order to compare the different oxidizing efficiencies of the plume in the different

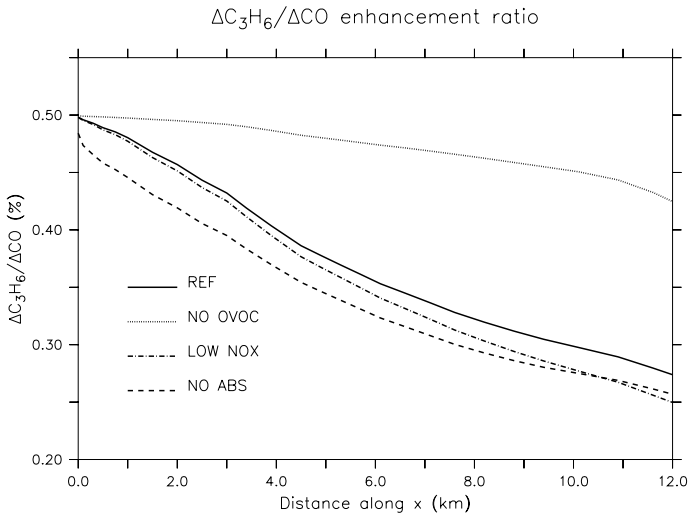

Figure 4.16: Enhancement ratios between C_3H_6 and CO as a function of distance from the fire after 90 minutes of simulation from the reference simulation and the 3 sensitivity studies.

simulations, the $\Delta C_3H_6/\Delta CO$ enhancement ratio along the plume is displayed in Figure 4.16 for the 4 simulations. In the NO OVOC case, the oxidation of propene is much less effective than in all other simulations as can be seen in the only slight reduction of the $\Delta C_3H_6/\Delta CO$ enhancement ratio as a function of distance from the fire. The $\Delta C_3H_6/\Delta CO$ enhancement ratio of the LOW NOX simulation is smaller than in the REF simulation, the difference increases with distance from the fire. The smallest enhancement ratio, pointing to the most effective atmospheric oxidation, is simulated in the NO ABS simulation.

In Tables 4.8 and 4.9, the relevant results from the 4 simulations for the oxidation efficiency of the plume are given. The plume-averaged OH concentrations in the LOW NOX and NO ABS are only slightly higher than in the REF simulation, $\sim 12\%$. However, in the NO OVOC scenario, the average OH concentrations are significantly lower than in the REF scenario. The largest maximum OH and HO_2

	$[OH]_{ave}$, $[OH]_{max}$ (ppt)	$[HO_2]_{ave}$, $[HO_2]_{max}$ (ppt)
REF	0.24, 0.83	4.92, 12.32
NO OVOC	0.11, 1.04	1.24, 10.58
LOW NOX	0.27, 0.77	7.67, 15.75
NO ABS	0.27, 1.30	5.55, 18.41

Table 4.8: Average and maximum value for the OH and HO_2 mixing ratios from the 4 simulations after 90 minutes.

	$P(HO_x)$ (molecule cm^{-3} s^{-1})	J(HCHO) % of $P(HO_x)$	$\tau(C_3H_6)$ (h)
REF	2.80×10^7	83.1	4.4
NO OVOC	3.74×10^6	46.4	19.8
LOW NOX	2.82×10^7	82.6	4.0
NO ABS	3.55×10^7	83.9	3.3

Table 4.9: Average HO_x-production rates in the plume as well as the relative contribution of HCHO photolysis are presented. The last column lists the calculated lifetime of propene.

mixing ratios are simulated in the NO ABS simulation, close to the fire. However, the largest averaged HO_2 mixing ratio is simulated by the LOW NOX scenario. The averaged photochemical production rate of HO_x is nearly identical in the REF and LOW NOX simulation, while it is much smaller in the NO OVOC simulation. The highest value of $P(HO_x)$ is found in the NO ABS simulation due to the enhanced photolysis frequencies (Figure 4.4). In all cases, the photolysis of HCHO is the main individual source of HO_x, with a contribution of more than 80% in the scenarios that include primary HCHO emission. Even in the NO OVOC scenario, where primary HCHO emissions are neglected, HCHO photolysis accounts for 46% of the HO_x-production. The second important reaction in this scenario, is the reaction of $O(^1D)$ with H_2O that accounts for 30% of the HO_x-production rate. In the last column of Table 4.9, the lifetimes of propene from the different scenarios are presented. Although the average OH concentration is the same, the calculated propene lifetimes differ significantly between the LOW NOX and the NO ABS simulations.

In the following section, the results from the sensitivity studies will be discussed and a general picture of the chemistry in young biomass burning plumes will be presented.

4.6.4 Discussion

From the results presented, the following conclusions concerning the photochemical processes occurring in a young biomass burning plume can be derived.

Plume chemistry is highly dominated by the direct emission of trace gases and aerosol particles from the fire. Due to the extremely high concentration of nitrogen oxides, photochemical production of ozone occurs in all investigated scenarios. However, the absolute amount of produced ozone and the resulting ozone concentration strongly depend on the fire emissions and the optical properties of the emitted aerosol. In all presented scenarios, radical loss occurs almost exclusively via the reaction of OH with NO_2. The reactions between radicals, e.g., the self reaction

of HO_2, are only of very minor importance. This dominance of the radical loss via NO_2 is an indication that ozone production occurs in the hydrocarbon limited regime [*Kleinmann et al.*, 1997]. The VOC sensitivity of the ozone production in a biomass burning plume during the first hours was also found in a box model study [*Mason et al.*, 2001].

Neglect of the primary emission of OVOCs from the fire leads to significant changes in photochemistry, resulting in ozone concentrations in the plume that are significantly lower than observed. Photochemical ozone production is strongly decreased in the NO OVOC scenario. Ozone production in the NO OVOC simulation is limited by the availability of peroxy radicals. Their average concentrations are extremely low compared to the REF simulation, (Table 4.8) because emission of HCHO that serves as the dominant precursor for radicals in the plume is not taken into account. However, even without primary HCHO emission, the photolysis of HCHO is the largest single source of radicals in the NO OVOC simulation, because HCHO is secondarily produced from the oxidations of hydrocarbons. The reduced concentrations of radicals are also responsible for the relatively small formation of NO_z compounds, and the increased lifetime of NO_x (Table 4.7) as well as the long lifetime of propene, resulting in a low oxidation efficiency. The enhanced contribution of HNO_3 to the concentration of NO_z as compared to the other simulations is explained by the neglect of the emissions of acetaldehyde, which is the main precursor of PAN.

A reduction of the NO_x emission leads to enhanced photochemical ozone production through reactions of NO with peroxy radicals. The lower NO concentration in the LOW NOX scenario is counteracted by enhanced radical concentrations (Table 4.8), because of a reduced radical loss. Additionally, the partitioning between OH and the peroxy radicals changes under lower NO_x mixing ratios, leading to a larger contribution of the peroxy radicals to the total radical concentration. Lower NO_x mixing ratios reduce the loss of OH through formation of HNO_3, although the OH mixing ratio slightly increases. The higher concentration of peroxy radicals, especially that of the peroxyacetyl radical (PA), can compensate for the reduced NO_x concentration leading to enhanced formation of PAN as compared to HNO_3 (Table 4.7). This effect was also observed in the model study by *Mason et al.* [2001]. The close agreement between the REF and the LOW NOX simulation in the production rate of NO_z is incidental.

The oxidation efficiency is enhanced in the LOW NOX simulation as compared to the REF case. This can be seen in the lifetime of propene (Table 4.9) and the lower enhancement ratio between C_3H_6 and CO (Figure 4.16). The decrease in $\tau(C_3H_6)$ is in the same order of magnitude as the increase of the average OH concentration ($\sim 10\%$).

The change in the absorbing properties of the emitted aerosol particles has the largest effect on atmospheric photochemistry for the considered sensitivity studies. Due to enhanced photolysis in the plume, especially that of HCHO, radical production is highly enhanced. Especially close to the fire, the OH mixing ratio from the NO ABS simulation exceeds the results from the other scenarios (Figure 4.15), because in this region the concentrations of the main HO_x precursor, HCHO, and the aerosol particles are highest. Photochemical ozone production for this scenario is highly enhanced compared to the other studies.

The total amount of photochemically produced NO_z is also highest in the NO ABS simulation, although the average concentration of OH and HO_2 are smaller or identical to the LOW NOX simulation. However, high radical concentrations are present in the NO ABS simulations close to the fire (Figure 4.15 for OH) where also the NO_x concentration is largest. In this region, most of the NO_z production occurs in the NO ABS case, leading to highly elevated NO_z concentrations in this simulation close to the fire (Figure 4.14). The misleading character of the averaged OH mixing ratio is also seen in the comparison of the propene lifetime between the LOW NOX and the NO ABS simulations. Although the averaged OH mixing ratio is identical in both scenarios, the propene lifetime differs by $\sim 18\%$. The reason for the shorter lifetime in the NO ABS simulation are the different spatial distributions of the OH concentration in the two scenarios. While in the LOW NOX case, the highest average value is found downwind the plume, the OH mixing ratio in the NO ABS simulation maximizes above the fire. As the removal of propene is much more effective close to the fire, because of its high concentration, the lifetime of propene is shorter in the NO ABS scenario. The reduced propene lifetime in the NO ABS simulation is also visible in the $\Delta C_3H_6/\Delta CO$ enhancement ratios from the different scenarios (Figure 4.16). A similar problem exists when mean OH concentrations from global models are compared [*Lawrence et al.*, 2001].

Overall it can be concluded that atmospheric photochemistry in a young biomass burning plume depends strongly on the availability of radicals. Formaldehyde is the primary precursor for radicals under these conditions. Neglecting its direct emission from the fire leads to unrealistically low ozone concentrations. Lower NO_x emissions lead to higher ozone production due to higher radical concentrations. The absorbing properties of the emitted aerosol particles strongly impact ozone production, leading to higher ozone production at lower absorption. Measurements of the $\Delta C_3H_6/\Delta CO$ enhancement ratios at different distances can serve as an indicator for the oxidation efficiency in an individual biomass burning plume.

4.7 Conclusions

In the present study, the photochemical processes in a young biomass burning plume were investigated with a three-dimensional (3D) chemical transport model. Meteorological conditions were taken from a previous simulation representing the situation of the plume from the Quinault fire. A chemical mechanism describing the oxidation of volatile organic compounds (VOCs) for the use in 3D atmospheric transport models under the conditions of a biomass burning plume was presented. The modeled concentration of CO and other primary emittants are in the range of observations.

Close to the fire, the ozone in the plume is highly depleted compared to background concentrations due to reaction of ozone with the emitted NO. Photochemical ozone production occurs in the plume at a rate of ~ 25 ppb h^{-1} and the downwind ozone concentration increases above background level. The simulated maximum value of 70 ppb ozone is reasonably close to observations in the plume from the Quinault fire and from other biomass burning plumes. The simulated $\Delta O_3/\Delta CO$ enhancement ratio (0.75%) is smaller than the ones reported from measurements. However, measurements from the Quinault fire are not available, and other appropriate observations are very limited. Photochemical ozone production is dominated by the reaction of HO_2 with NO ($\sim 69\%$). Peroxy radicals from the alkenes also contribute significantly to the ozone production. Formation of nitrogen reservoir species, NO_z, is dominated by HNO_3, which accounts for $\sim 60\%$ of the NO_z production. The second most important nitrogen reservoir species under the conditions presented is peroxyacetyl nitrate (PAN). The role of HONO as a nitrogen reservoir is limited to the regions close to the fire. The partitioning of the inactive nitrogen species is important for the regional effect of biomass burning. Significant atmospheric oxidation of alkenes occurs within the first tens of minutes after their release into the atmosphere. Photochemistry in biomass burning plumes is limited by the availability of radicals. Their photochemical production occurs mainly from the photolysis of formaldehyde, which is emitted from the fire. Secondary production from the oxidation of VOCs accounts for $\sim 12\%$ of the HCHO concentration.

In the sensitivity studies, the importance of the oxygenated volatile organic compounds (OVOCs), the emission ratio of NO_x, and the single-scattering albedo of the aerosol for the simulation of the ozone concentration were shown. The neglect of the primary emissions of OVOCs leads to unrealistic low ozone concentrations. A reduced emission ratio of NO_x as well as a non-absorbing aerosol enhance the ozone concentration within the range of the observations. The production of radicals through the photolysis of HCHO is crucially important for the formation of ozone and nitrogen reservoir species, and the oxidation of alkenes. Any change in this source of radicals, e.g., through the neglect of primary HCHO emissions or through enhanced photolysis due to less aerosol absorption, has a significant effect on pho-

tochemistry. Enhanced radical production leads to enhanced ozone production, enhanced formation of nitrogen reservoir species, and a higher oxidation efficiency. The partitioning of the nitrogen reservoir species is affected by the neglect of acetaldehyde emissions as well as by lower NO_x emissions. In both cases, the contribution of PAN to NO_z increases; however, the effect of the omission of acetaldehyde emissions is much larger than that of reduced NO_x emission. The oxidation efficiency in the plume is not only linked to the average concentration of the OH radical, but additionally to the spatial distribution of its concentration. The enhancement ratio between propene and CO is a good indicator for the oxidation efficiency in a biomass burning plume.

The results from this study show that ATHAM is a valuable tool to investigate photochemical processes in young biomass burning plumes. Future studies will focus on the simulation of vegetation fires in different regions, e.g., the boreal forest, or the tropical savanna. The potential formation of a convective cloud from the fire-induced convection allows the investigation of several other atmospheric processes, e.g., scavenging of gas phase species into water droplets and ice particles, aerosol-cloud interaction, and the formation of ice. As ATHAM includes all the required modules, it is an excellent tool for further studies on the atmospheric processes in young biomass burning plumes.

Chapter 5

Conclusions and Outlook

5.1 Conclusions

The primary goal of this study was to improve the understanding of the atmospheric processes that occur in individual biomass burning plumes during the first tens of minutes after the release of the emissions into the atmosphere. For this purpose, the plume model ATHAM was used and extended by a module to simulate the atmospheric photochemical processes. It was shown that ATHAM is capable of simulating the convection induced by a prescribed fire using an external heat flux. For the case of the Quinault fire, a prescribed fire conducted on the US Pacific Coast, September 1994, the simulated atmospheric concentrations of the emitted aerosol particles compare well with the observations. Remaining differences between the model results and the measurements are attributed to limited meteorological and fire emission information. The aerosol absorption derived from in situ measurements is inconsistent with remote sensing observations of the radiance. While in situ measurements indicate a single-scattering albedo at 550 nm of 0.85, the measured upwelling radiance implies a lower limit of 0.94 for the single-scattering albedo.

Observations of the upward irradiance above the plume are influenced by the finite dimensions of the plume leading to its overestimation in one-dimensional radiative transfer models. The impact of three-dimensional radiation effects on the actinic flux in the plume is significant and depends on the absorbing properties of the aerosol. In the case of a strongly absorbing aerosol, the horizontal photon transport enhances the actinic flux in the plume center by more than +200%, while it changes the actinic flux in the case of a non-absorbing aerosol by around −40%. The magnitude of the three-dimensional radiation effects make them potentially important for the photochemistry in biomass burning plumes and phenomena of similar dimensions, e.g., convective clouds. However, at the present, it is not possible to incorporate three-dimensional solar radiation transfer models in chemical transport

models because of limited computer power.

Photochemical processes in young biomass burning plumes depend highly on the emissions from the fire. Oxidation of the emitted volatile organic compounds in the presence of nitrogen oxides leads to the production of ozone. Model simulations result in maximum ozone mixing ratios in the plume of about 70 ppb for the Quinault fire comparable to observations. Above the fire, ozone concentrations in the plume show a local minimum due to the fast reaction of ozone with the emitted NO. Significant amounts of nitrogen reservoir species, NO_z, are formed in the plume during the first 90 min after the emissions have been released. HNO_3 and peroxyacetyl nitrate (PAN) are the dominant NO_z species accounting for ∼60% and ∼30%, respectively. Oxidation of alkenes, especially that of propene, occurs in young biomass burning plumes as shown in a change in the enhancement ratio between the alkenes and CO as a function of distance from the fire.

The analysis of the simulations shows that the ozone production, the formation of nitrogen reservoir species, and the oxidation of organic compounds are highly limited by the availability of radicals in the plume. Production of radicals is dominated by the photolysis of formaldehyde (∼80% of the total radical production) that is primary emitted by the fire. Neglecting these primary emissions leads to unrealistic low ozone concentrations in the simulations. The relative contributions of HNO_3 and PAN to the nitrogen reservoir species depend on primary emissions of acetaldehyde and slightly on NO_x emissions. The absorbing properties of the emitted aerosol have a significant impact on the photolysis frequencies and on the ozone concentration in the plume. A non-absorbing aerosol leads to enhanced ozone production and ozone concentrations compared to an absorbing aerosol.

Overall, it was shown that young biomass burning plumes are an excellent example to study several aspects of atmospheric science and that ATHAM is a suitable tool for further investigations of processes in these plumes.

5.2 Outlook

Based on the results of this work, future research activities are expected to further increase our understanding of the processes in biomass burning plumes and to improve their representation in atmospheric chemical transport models. As several general atmospheric processes are involved in the evolution of a biomass burning plume, e.g., convective dynamics, transport, formation of hydrometeores, aerosol optics, photochemical processing, improved understanding of the processes in biomass burning plumes also improves our understanding of similar atmospheric features, e.g., convective clouds.

The aerosol absorption was shown to be a very sensitive parameter for the pho-

tochemistry in biomass burning plumes. As it is additionally one of the largest uncertainties in the direct radiative forcing of aerosol particles, especially those from biomass burning [*Penner et al.*, 2001], future studies should try to reduce its uncertainty. As shown in this work and in other studies [*Remer et al.*, 1998; *Kaufman et al.*, 2001], there might be a discrepancy between remote sensing and in situ measurements of the single-scattering albedo. There are indications, that in situ measurements based on the sampling of the aerosol on filters might overestimate the absorption [*Bond et al.*, 1999]. A promising alternative seems to be the use of a photoacoustic spectrometer, which has the ability to measure aerosol absorption without disturbing the aerosol [*Petzold and Niessner*, 1996; *Arnott et al.*, 1999]. Besides different in situ measurement techniques, remote sensing observations should also be incorporated in studies of the aerosol absorption, especially as they more directly measure the climate related effect, i.e., the backscattered radiation, of the aerosol. As a third component in the investigation of the aerosol absorption, measurements of the physical and chemical properties of the aerosol should be performed, in order to calculate the aerosol absorption. For this purpose, the state of mixing, the density and the refractive index of the components have to be determined. Depending on the morphology of the particles, Mie theory might not be appropriate for the calculation of the optical properties of the particles, but more complex methods might be necessary, e.g., the discrete dipole approximation [*Draine and Flatau*, 1994; *Martins et al.*, 1998].

For the interpretation of measurements above finite plumes and clouds, and for the use in small-scale chemical transport models, three-dimensional radiation effects should be taken into account. Because of their high requirements of computer power, three-dimensional radiative transfer models cannot be incorporated on a regular basis in atmospheric transport models. However, further case studies using simulated three-dimensional fields of aerosol particles or cloud droplets might give important insights into three-dimensional radiative effects. A promising attempt to incorporate 3D radiative effects into chemical transport models might be the tilted independent pixel approximation (TIPA) [*Várnai and Davis*, 1999]. However, this method only treats horizontal transport of photons for the direct solar beam. Loss of photons from the plume due to scattering processes as shown in Chapter 3 for the case of the non-absorbing aerosol, cannot be taken into account. The 3D radiation effect on the zenith radiance is expected to be small. A slight wavelength dependence of the 3D effect might be present leading to an underestimation of the retrieved aerosol size distribution from remote sensing [*Tanré et al.*, 1997]. However, this effect has not yet been quantified.

For the photochemical simulations, the incorporation of a flexible tool for the calculation of the optical properties of the aerosol would be desirable. For this

purpose, the parameterization derived by *Grant et al.* [1999] seems to be well suited. It describes the dependence of the aerosol optical properties on the black carbon content and on the relative humidity.

There are a number of open questions for further investigations of the photochemistry in young biomass burning plumes. Further improvements of the representation of the atmospheric chemistry should be performed by including the oxidation of higher volatile organic compounds and aromatic compounds in the plume. Although their emission ratios per molecule are comparable low, their emission ratios per carbon atom and their impact on photochemistry might be significant [*Koppmann et al.*, 1997]. However, their oxidation chain is highly complex and still rather uncertain. There is a recent attempt to include oxidation of aromatic compounds into a reduced mechanism of tropospheric chemistry [*Zaveri and Peters*, 1999]. However, due to the highly optimized treatment in this approach, the transfer of this mechanism into the one developed in this thesis is not straightforward.

Another step to improve the model performance would be an improved treatment of heterogeneous reactions. The interaction of species in the gas phase with the surface of the aerosol particles and hydrometeors might significantly affect their gas phase concentration. There are indications for an uptake of nitric acid, HNO_3, by biomass burning aerosol [*Tabazadeh et al.*, 1998] and of ozone by liquid unsaturated organic compounds [*de Gouw and Lovejoy*, 1998]. In the presence of water droplets, effective scavenging of soluble compounds, e.g., nitric acids, will take place [*Mari et al.*, 2000]. The formation of ice particles changes the scavenging efficiencies significantly [*Mari et al.*, 2000; *Barth et al.*, 2001]. These complex interactions point to the need for a detailed description of these processes. The formation of water and ice droplets is already included in ATHAM [*Textor*, 1999]. The inclusion of heterogeneous reactions on these hydrometeores therefore seems to be straightforward. However, for a more realistic representation, the incorporation of chemical reactions in the hydrometeores would also be required. A more detailed treatment of the interaction of the aerosol particles with the gas phase compounds should be incorporated in ATHAM, including information on the chemical composition of the aerosol. However, only little is known about the chemical properties of the biomass burning aerosol. Some modules are already available, that treat the gas-aerosol interaction [e.g., *Nenes et al.*, 1999; *Capaldo et al.*, 2000] and might be helpful for further investigation of the processes in young biomass burning plumes.

For the evaluation of future model simulations, more measurements of young biomass burning plumes are highly required. For model evaluation, not only observations from the resulting plume, but additionally from the fire, i.e., the heat emissions and the amount of burned biomass, have to be performed. Also a good characterization of the atmospheric conditions, i.e., the temperature and humidity

profiles as well as the wind speed and direction, is of importance for the dynamical simulation. For the model evaluation, remote sensing and in situ measurements would be desirable. While from the remote sensing observations, the general appearance of the plume can be determined, in situ measurements can be used for a more quantitative evaluation of the model results. Quantities to be measured include the aerosol mass concentration, or a quantity that is closely related to that, e.g., the scattering coefficient, and the CO concentration as passive tracers. For photochemical studies, observations of ozone, nitrogen oxides, nitrogen reservoir species, alkenes, and the individual contributions of HNO_3 and PAN to the nitrogen reservoir species would be desirable.

With the help of evaluated model simulations, the representation of vegetation fires in regional and global models can be improved. Therefore, simulations of vegetation fires should be performed under different meteorological situations and fire emissions. These should include typical situations for fires in different ecosystems. These simulations might result in a parameterization of the injection height of the fire emissions using parameters available from regional and global models, e.g., the temperature profile and the horizontal wind speed. Available parameterizations depend only on the maximum energy release of the fire [*Manis*, 1985]. The problems of global models to resolve the photochemical processes at the fires might be addressed with the help of effective emission indices as it is performed for the case of aircraft emissions [*Petry et al.*, 1998]. Other promising approaches might be the method proposed by *Sillman et al.* [1990] or the concept of the intensity of segregation [*Krol et al.*, 2000]. These investigations could result in an improved version of the database for biomass burning emissions presented in Figure 1.1 for the use in global models.

Overall it appears that young biomass burning plumes are an emerging field of research for several disciplines in the atmospheric science community.

Appendix A

Chemical Mechanism

The following tables present the chemical mechanism. Table A.1 lists the considered chemical species, Table A.2 the chemical reactions included in the chemical mechanism together with the used rate coefficients and the references. Most of the reaction rates were taken from evaluations: *Tyndall et al.* [2001], *Sander et al.* [2000], *DeMore et al.* [1997], *Atkinson et al.* [1997], and *Atkinson et al.* [2000].

Table A.1: List of species included in the chemical mechanism.

Species	Symbol
Ozone	O_3
Excited-state oxygen atom	$O(^1D)$
Hydroxyl radical	OH
Hydroperoxyl radical	HO_2
Hydrogen peroxide	H_2O_2
Nitric oxide	NO
Nitrogen dioxide	NO_2
Nitrate radical	NO_3
Nitrogen pentoxide	N_2O_5
Nitrous acid	HONO
Nitric acid	HNO_3
Pernitric acid	HNO_4
Carbon monoxide	CO
Methane	CH_4
Methylperoxy radical	CH_3O_2

continued on next page

continued

Species	Symbol
Methyl hydrogen peroxide	CH_3OOH
Formalydehyde	HCHO
Methanol	CH_3OH
Ethane	C_2H_6
Ethylperoxy radical	$C_2H_5O_2$
Ethyl hydrogen peroxide	C_2H_5OOH
Acetaldehyde	CH_3CHO
Peroxyacetyl nitrate	PAN
Peroxyacetyl radical	PA
Peroxyacetic acid	PAA
Formic acid	HCOOH
Acetic acid	CH_3COOH
Ethene	C_2H_4
Hydroxyethylperoxy radical	EO2
Hydroxyethyloxy radical	EO
Hydroxyethyl hydro peroxide	EOOH
Glycolaldehyde	$HOCH_2CHO$
Hydroxyperoxyacetyl radical	GCO3
Acetone	CH_3COCH_3
Acetonylperoxy radical	$ACETO_2$
Acetonylhydroperoxide	ACETOOH
Propene	C_3H_6
Hydroxypropylperoxy radical	PO2
Hydroxypropylen hydro peroxide	POOH

Table A.2: List of chemical reactions and rate constants included in the mechanism. The units for rate constants k of first-order reactions are s^{-1}; of second-oder reactions, $cm^3\ s^{-1}$; and for third-order reactions, $cm^6\ s^{-1}$

Nr.	Reaction	Rate Constant, k	Note
1	$O_3 + h\nu \longrightarrow O^1(D) + O_2$	$J(O(^1D))$	1
2	$O(^1D) + O_2 \longrightarrow O_3$	$3.2\times10^{-11}\ \exp(70/T)$	1
3	$O(^1D) + N_2 \longrightarrow O_3$	$1.8\times10^{-11}\ \exp(110/T)$	1
4	$O(^1D) + H_2O \longrightarrow 2\,OH$	2.2×10^{-10}	1
5	$O(^1D) + H_2 \longrightarrow OH + HO_2$	5.8×10^{-7}	1
6	$O(^1D) + CH_4 \longrightarrow 0.75\,CH_3O_2 + 0.75\,OH$ $+0.25\,HCHO + 0.4\,HO_2$	1.5×10^{-10}	1
7	$O_3 + OH \longrightarrow HO_2$	$1.5\times10^{-12}\ \exp(-880/T)$	2
8	$O_3 + HO_2 \longrightarrow OH$	$2.0\times10^{-14}\ \exp(-680/T)$	2
9	$HO_2 + OH \longrightarrow H_2O$	$4.8\times10^{-11}\ \exp(250/T)$	1
10	$2\,HO_2 \longrightarrow H_2O_2$	$(k_a+k_b)(1+k_c)$ $k_a= 2.3\times10^{-13}\ \exp(600/T)$ $k_b= 1.7\times10^{-33}\ \exp(1000/T)\ [M]$ $k_c= 1.4\times10^{-21}\ \exp(2200/T)\ [H_2O]$	1,19
11	$H_2O_2 + h\nu \longrightarrow 2\,OH$	$J(H_2O_2)$	1
12	$OH + H_2O_2 \longrightarrow HO_2$	$2.9\times10^{-12}\ \exp(-160/T)$	1
13	$OH + CO \longrightarrow HO_2$	$1.5\times10^{-13}\ (1+0.6\ P_{atm})$	1
14	$CH_4 + OH \longrightarrow CH_3O_2 + H_2O$	$2.8\times10^{-14}\ T^{2/3}\ \exp(-1575/T)$	1
15	$CH_3O_2 + HO_2 \longrightarrow CH_3OOH$	$4.15\times10^{-13}\ \exp(750/T)$	3

Table A.2: continued

Nr.	Reaction	Rate Constant, k	Note
16	$CH_3O_2 + NO \longrightarrow HCHO + HO_2 + NO_2$	2.8×10^{-12} exp(300/T)	3
17	$CH_3O_2 + NO_3 \longrightarrow HCHO + HO_2 + NO_2$	1.3×10^{-12}	4
18	$CH_3O_2 + CH_3O_2 \longrightarrow HCHO + CH_3OH$	9.5×10^{-14} exp(390/T) / (1+26.2 exp(-1130/T))	3
19	$CH_3O_2 + CH_3O_2 \longrightarrow 2\,HCHO + 2\,HO_2$	9.5×10^{-14} exp(390/T) / (1+1/26.2 exp(1130/T))	3
20	$CH_3OH + OH \longrightarrow HCHO + HO_2$	6.7×10^{-12} exp(−600/T)	1
21	$CH_3OOH + h\nu \longrightarrow HCHO + HO_2 + OH$	$J(CH_3OOH)$	1
22	$CH_3OOH + OH \longrightarrow 0.7\,CH_3O_2 + 0.3\,HCHO + 0.3\,OH$	3.8×10^{-12} exp(200/T)	1
23	$HCHO + h\nu \longrightarrow CO + 2\,HO_2$	$J(HCHO)_a$	1
24	$HCHO + h\nu \longrightarrow CO$	$J(HCHO)_b$	1
25	$HCHO + OH \longrightarrow CO + HO_2$	$1.\times10^{-11}$	1
26	$HCHO + NO_3 \longrightarrow HNO_3 + CO + HO_2$	3.4×10^{-13} exp(-1900/T)	5
27	$NO + O_3 \longrightarrow NO_2$	3.0×10^{-12} exp(−1500/T)	2
28	$NO + OH \longrightarrow HONO$	F(7.0(−31),2.6,3.6(−11),0.1,0.6)	1,20
29	$NO + HO_2 \longrightarrow NO_2 + OH$	3.5×10^{-12} exp(250/T)	1
30	$NO + NO + O_2 \longrightarrow 2\,NO_2$	3.3×10^{-39} exp(530/T)	6
31	$NO_2 + h\nu \longrightarrow NO + O_3$	$J(NO_2)$	1
32	$NO_2 + O_3 \longrightarrow NO_3$	1.2×10^{-13} exp(−2450/T)	1
33	$NO_2 + OH \longrightarrow HNO_3$	k_{NO_2+OH}	7
34	$NO_2 + HO_2 \longrightarrow HNO_4$	F(1.8(−31),3.2,4.7(−12),1.4,0.6)	1,20

Table A.2: continued

Nr.	Reaction	Rate Constant, k	Note
35	$NO_2 + CH_3O_2 \longrightarrow CH_3O_2NO_2$	F(1.3(−30),4.0,7.6(−12),2.0,0.6)	3,20
36	$NO_2 \longrightarrow 0.5\,HONO$	γ=1.0×10^{-6}	8
37	$NO_3 + h\nu \longrightarrow NO_2 + O_3$	$J(NO_3)_a$	1
38	$NO_3 + h\nu \longrightarrow NO$	$J(NO_3)_b$	1
39	$NO_3 + NO \longrightarrow 2\,NO_2$	1.5×10^{-11} exp(170/T)	1
40	$NO_3 + NO_2 \longrightarrow N_2O_5$	F(2.0(−30),4.4,1.4(−12),0.7,0.6)	1,20
41	$NO_3 + OH \longrightarrow NO_2 + HO_2$	2.2×10^{-11}	1
42	$NO_3 + HO_2 \longrightarrow 0.8\,OH + 0.8\,NO_2 + 0.2\,HNO_3$	3.5×10^{-12}	1
43	$HONO + h\nu \longrightarrow NO + OH$	0.23×$J(NO_2)$	9
44	$HONO + OH \longrightarrow NO_2$	1.1×10^{-11} exp(−390/T)	1
45	$HNO_3 + h\nu \longrightarrow OH + NO_2$	$J(HNO_3)$	1
46	$HNO_3 + OH \longrightarrow NO_3$	k_d+k_f/(1+k_f/k_e) k_d=2.41×10^{-14} exp(460/T) k_e=2.69×10^{-17} exp(2199/T) k_f=6.51×10^{-34} exp(1335/T) [M]	2,19
47	$HNO_4 + h\nu \longrightarrow 0.39\,NO_3 + 0.39\,OH + 0.61\,NO_2$	$J(HNO_4)$	1
48	$HNO_4 + OH \longrightarrow NO_2$	1.3×10^{-12} exp(380/T)	1
49	$HNO_4 \xrightarrow{M} HO_2 + NO_2$	$k_{NO_2+HO_2}$/(2.1×10^{-27} exp(10900/T))	1
50	$CH_3O_2NO_2 + h\nu \longrightarrow CH_3O_2 + NO_2$	4.66×10^{-3}×J(O(^{1}D))	6, 10
51	$CH_3O_2NO_2 \xrightarrow{M} CH_3O_2 + NO_2$	$k_{NO_2+CH_3O_2}$/(1.3×10^{-28} exp(11200/T))	1

Table A.2: continued

Nr.	Reaction	Rate Constant, k	Note
52	$N_2O_5 + h\nu \longrightarrow NO_3 + NO_2$	$J(N_2O_5)$	1
53	$N_2O_5 \xrightarrow{M} NO_3 + NO_2$	$k_{NO_3+NO_2}/(3.0\times10^{-27}\ \exp(10991/T))$	2
54	$N_2O_5 \longrightarrow 2\,HNO_3$	γ=0.1	1
55	$N_2O_5 + H_2O \longrightarrow 2HNO_3$	$2.5\times10^{-22} + 1.8\times10^{-39}\ [H_2O]$	11,19
56	$C_2H_6 + OH \longrightarrow C_2H_5O_2$	$1.51\times10^{-17}\ T^2\ \exp(-492/T)$	4
57	$C_2H_5O_2 + HO_2 \longrightarrow C_2H_5OOH$	$7.4\times10^{-13}\ \exp(700/T)$	4
58	$C_2H_5O_2 + NO \longrightarrow CH_3CHO + HO_2 + NO_2$	$2.7\times10^{-12}\ \exp(350/T)$	4
59	$C_2H_5OOH + h\nu \longrightarrow CH_3CHO + HO_2 + OH$	$J(CH_3OOH)$	1,21
60	$C_2H_5OOH + OH \longrightarrow 0.7\,C_2H_5O_2 + 0.3\,CH_3CHO + 0.3\,OH$	$3.8\times10^{-12}\ \exp(200/T)$	1,21
61	$CH_3CHO + h\nu \longrightarrow CH_3O_2 + HO_2 + CO$	$J(CH_3CHO)$	1
62	$CH_3CHO + OH \longrightarrow PA$	$5.6\times10^{-12}\ \exp(270/T)$	1
63	$PA + HO_2 \longrightarrow PAA$	$4.3\times10^{-13}\ \exp(1040/T)\ /$ $(1+1/37\ \exp(660/T))$	3
64	$PA + HO_2 \longrightarrow CH_3COOH + O_3$	$4.3\times10^{-13}\ \exp(1040/T)\ /$ $(1+37\ \exp(-660/T))$	3
65	$PA + CH_3O_2 \longrightarrow HCHO + 0.9\,HO_2 + 0.9\,CH_3O_2 + 0.1\,CH_3COOH$	$2.0\times10^{-12}\ \exp(500/T)$	3
66	$PA + NO \longrightarrow CH_3O_2 + NO_2$	$8.1\times10^{-12}\ \exp(270/T)$	3

Table A.2: continued

Nr.	Reaction	Rate Constant, k	Note
67	$PA + NO_2 \longrightarrow PAN$	F(8.5(−29),6.5,1.1(−11),1.0,0.6)	3,20
68	$PA + NO_3 \longrightarrow CH_3O_2 + NO_2$	4.0×10^{-12}	5
69	$PAA + h\nu \longrightarrow CH_3O_2$	$0.025\times J(HCHO)_a$	10
70	$PAA + OH \longrightarrow 0.7\,PA$ $+0.3\,HCHO + 0.3\,OH$	$3.8\times10^{-12}\ \exp(200/T)$	1,21
71	$PAN + h\nu \longrightarrow 0.8\,PA + 0.8\,NO_2$ $+0.2\,CH_3O_2 + 0.2\,NO_3$	$J(PAN)$	1
72	$PAN \xrightarrow{M} PA + NO_2$	$k_{PA+NO_2}/(9.3\times10^{-29}\ \exp(-14000/T))$	3
73	$HCOOH + OH \longrightarrow HO_2 + H_2O$	4.0×10^{-13}	1
74	$CH_3COOH + OH \longrightarrow CH_3O2$	$4.0\times10^{-13}\ \exp(200/T)$	1
75	$C_2H_4 + OH \longrightarrow EO_2$	F(1.0(−28),0.8,8.8(−12),0.0,0.6)	1,20
76	$EO_2 + NO \longrightarrow 0.75\,EO + 0.5\,HCHO$ $+0.25\,HO_2 + NO_2$	9.0×10^{-12}	6, 12
77	$EO_2 + HO_2 \longrightarrow EOOH$	1.0×10^{-11}	6
78	$EO_2 + NO_3 \longrightarrow EO + NO_2$	1.2×10^{-12}	5
79	$EO \longrightarrow HO_2 + 2\,HCHO$	$1.2\times10^{+12}\ \exp(-4750/T)$	12
80	$EO + O_2 \longrightarrow HO_2 + HOCH_2CHO$	$6.0\times10^{-14}\ \exp(-550/T)$	12
81	$HOCH_2CHO + h\nu \longrightarrow CO + 0.8\,HCHO$ $+1.6\,HO_2 + 0.2\,CH_3OH$	$2.5\times J(CH_3COCH_3)$	13
82	$HOCH_2CHO + OH \longrightarrow GCO3$	1.0×10^{-11}	6
83	$EOOH + h\nu \longrightarrow EO + OH$	$J(CH_3OOH)$	1,21

Table A.2: continued

Nr.	Reaction	Rate Constant, k	Note
84	$EOOH + OH \longrightarrow 0.7\,EO_2 + 0.3\,OH$ $+0.3\,HOCH_2CHO$	3.80×10^{-12} exp(200/T)	1,21
85	$GCO3 + HO_2 \longrightarrow PAA$	4.3×10^{-13} exp(1040/T) / (1+1/37 exp(660/T))	3,22
86	$GCO3 + HO_2 \longrightarrow CH_3COOH + O_3$	4.3×10^{-13} exp(1040./T) / (1+37 exp(−660/T))	3,22
87	$GCO3 + NO \longrightarrow NO_2 + HO_2 + HCHO$	8.1×10^{-12} exp(270/T)	3,22
88	$GCO3 + NO_2 \longrightarrow PAN$	1.1×10^{-11} (T/298)$^{-1.0}$	3,22
89	$C_2H_4 + O_3 \longrightarrow HCHO + 0.22\,HO_2$ $+0.12\,OH + 0.24\,CO + 0.52\,HCOOH$	1.2×10^{-14} exp(−2630/T)	1, 14
90	$CH_3COCH_3 + h\nu \longrightarrow PA + CH_3O_2$	$J(CH_3COCH_3)$	15
91	$CH_3COCH_3 + OH \longrightarrow ACETO_2$	8.8×10^{-12} exp(−1320/T)	16
92	$CH_3COCH_3 + OH \longrightarrow CH_3COOH$ $+CH_3O_2$	1.7×10^{-14} exp(423/T)	16
93	$ACETO_2 + HO_2 \longrightarrow ACETOOH$	8.6×10^{-13} exp(700/T)	3
94	$ACETO_2 + NO \longrightarrow NO_2 + PA + HCHO$	2.8×10^{-12} exp(300/T)	3
95	$ACETOOH + h\nu \longrightarrow PA + HCHO + OH$	$J(CH_3OOH)$	1,21
96	$ACETOOH + OH \longrightarrow 0.7\,ACETO_2$ $+0.3\,OH$	3.8×10^{-12} exp(200/T)	1,21
97	$C_3H_6 + OH \longrightarrow PO_2$	F(8.0(−27),3.5,3.0(−11),0.0,0.5)	6,20
98	$PO_2 + HO_2 \longrightarrow POOH$	3.5×10^{-13} exp(1000/T)	17
99	$PO_2 + NO \longrightarrow NO_2 + HCHO + HO_2$ $+CH_3CHO$	4.9×10^{-12} exp(180/T)	17

Table A.2: continued

Nr.	Reaction	Rate Constant, k	Note
100	$POOH + h\nu \longrightarrow OH + HO_2 + HCHO$ $+CH_3CHO$	$J(CH_3OOH)$	1,21
101	$POOH + OH \longrightarrow 0.7\,PO_2 + 0.3\,OH$	$3.8\times10^{-12}\ \exp(200/T)$	1,21
102	$C_3H_6 + O_3 \longrightarrow 0.148\,HCOOH$ $+0.09\,CH_3COOH + 0.71\,CO$ $+0.372\,OH + 0.252\,HO_2 + 0.324\,CH_3O_2$ $+0.084\,CH_4 + 0.702\,HCHO$ $+0.4\,CH_3CHO$	$6.5\times10^{-15}\ \exp(-1900/T)$	1, 18

Notes are 1, Rate constant, absorption cross section, quantum yield, and uptake coefficient from *DeMore et al.* [1997], Photolysis frequencies, J, are calculated using the method of *Landgraf and Crutzen* [1998]; 2, Rate constant, absorption cross section and quantum yield from *Sander et al.* [2000]; 3, Rate constant from *Tyndall et al.* [2001]; 4, Rate constant from *Atkinson et al.* [2000]; 5, Rate constant from *Stockwell et al.* [1997]; 6, Rate constant from *Atkinson et al.* [1997]; 7, Temperature and pressure dependent rate constant from *Dransfield et al.* [1999]; 8, Uptake coefficient from *Kleffmann et al.* [1998]; 9, Correlation taken from the Master Chemical Mechanism (MCM) [*Saunders et al.*, 1997], available at http://cast.nerc.ac.uk/LIBRARY/MCM2/FRMCMindx.htm; 10, Correlation calculated from R. von Kuhlmann [*von Kuhlmann*, 2001, and pers. comm.]; 11, Rate constant from *Wahner et al.* [1998]; 12, Rate constant and branching ratio from *Orlando et al.* [1998]; 13, Correlation coefficient taken from *Bacher et al.* [2001]; 14, Products taken from *Zaveri and Peters* [1999]; 15, Absorption cross sections and quantum yields taken from *Gierczak et al.* [1998]; 16, Rate constants taken from *Wollenhaupt et al.* [2000]; *Wollenhaupt and Crowley* [2000]; 17, General recommendation from *Atkinson* [1994]; 18, The branching ratio for the two channels was set to 4:6, according to *Stockwell et al.* [1997], decomposition of the Criegee radicals was taken from *Atkinson et al.* [1997], stabilized CH_2OO was assumed to be HCOOH; 19, [M] is the air and [H_2O] is the water vapor concentration, both in molecule cm^{-3}; 20, Troe expression function F(k_0^{300}, n, k_∞^{300}, m, F_c), numbers of the form 7.0(−31) are to be read as 7.0×10^{-31}; 21, Reaction rates for oxidation and photolysis for higher hydroperoxides were taken identically to CH_3OOH; 22, Reaction rates for GCO3 were assumed to be identical to the ones from PA.

List of Figures

List of Tables

References

Albrecht, B. A., Aerosols, cloud microphysics, and fractional cloudiness, *Science*, *245*, 1227–1230, 1989.

Anderson, G. P., S. A. Clough, F. X. Kneizys, J. H. Chetwynd, and E. P. Shettle, AFGL atmospheric constituent profiles (0–120 km), *Tech. Rep. AFGL-TR-86-0110*, Air Force Geophys. Lab., Hanscom Air Force Base, Mass., 1986.

Andreae, M. O., Soot carbon and excess fine potassium: Long range transport of combustion derived aerosols, *Science*, *220*, 1148–1151, 1983.

Andreae, M. O., Biomass burning: Its history, use, and distribution and its impact on environmental quality and global climate, in *Global Biomass Burning: Atmospheric, Climatic, and Biospheric Implications*, edited by J. S. Levine, pp. 3–21, MIT Press, Cambridge, Mass., 1991.

Andreae, M. O., The influence of tropical biomass burning on climate and the atmospheric environment, in *Biogeochemistry of Global Change: Radiatively Active Trace Gases*, edited by R. S. Oremland, pp. 113–150, Chapman & Hall, New York, NY, 1993.

Andreae, M. O., and P. Merlet, Emission of trace gases and aerosols from biomass burning, *Global Biogeochem. Cycles*, *15*, 955–966, 2001.

Andreae, M. O., B. E. Anderson, D. R. Blake, J. D. Bradshaw, J. E. Collins, G. L. Gregory, G. W. Sachse, and M. C. Shipham, Influence of plumes from biomass burning on atmospheric chemistry over the equatorial and tropical South Atlantic during CITE 3, *J. Geophys. Res.*, *99*, 12,793–12,808, 1994.

Andreae, M. O., E. Atlas, H. Cachier, W. R. Cofer, G. W. Harris, G. Helas, R. Koppmann, J.-P. Lacaux, and D. Ward, Trace gas and aerosol emissions from savanna fires, in *Biomass Burning and Global Change*, edited by J. S. Levine, pp. 278–295, MIT Press, Cambridge, Mass., 1996a.

Andreae, M. O., J. Fishman, and J. Lindesay, The Southern Tropical Atlantic Region Experiment (STARE): Transport and Atmospheric Chemistry near the Equator-Atlantic (TRACE A) and Southern African Fire-Atmosphere Research Initiative (SAFARI): An introduction, *J. Geophys. Res.*, *101*, 23,519–23,520, 1996b.

Andreae, M. O., et al., Biomass-burning emissions and associated haze layers over amazonia, *J. Geophys. Res.*, *93*, 1509–1527, 1988.

Andreae, M. O., et al., Methyl halide emissions from savanna fires in southern Africa, *J. Geophys. Res.*, *101*, 23,603–23,613, 1996c.

Andreae, M. O., et al., Transport of biomass burning smoke to the upper tropsophere by deep convection in the equatorial region, *Geophys. Res. Lett.*, *28*, 951–954, 2001.

Arnott, W. P., H. Moosmüller, C. F. Rogers, T. Jin, and R. Bruch, Photoacoustic spectrometer for measuring light absorption by aerosol: instrument description, *Atmos. Environ.*, *33*, 2845–2852, 1999.

Atkinson, R., Gas-phase tropospheric chemistry of organic compounds, Monograph No. 2 of the J. Phys. Chem. Ref. Data, 1994.

Atkinson, R., Atmospheric chemistry of VOCs and NO_x, *Atmos. Environ.*, *34*, 2063–2101, 2000.

Atkinson, R., D. L. Baulch, R. A. Cox, R. F. Hampson, Jr., J. A. Kerr, M. J. Rossi, and J. Troe, Evaluated kinetic and photochemical data for atmospheric chemistry, Supplement V, *J. Phys. Chem. Ref. Data*, *26*, 521–1011, 1997, IUPAC Subcommittee in Gas Kinetic Data Evaluation for Atmospheric Chemistry.

Atkinson, R., D. L. Baulch, R. A. Cox, R. F. Hampson, Jr., J. A. Kerr, M. J. Rossi, and J. Troe, Summary of evaluated kinetic and photochemical data for atmospheric chemistry, available at http://www.iupac-kinetic.ch.cam.ac.uk/, 2000.

Bacher, C., G. S. Tyndall, and J. J. Orlando, The atmospheric chemistry of glycolaldehyde, *J. Atmos. Chem.*, *39*, 171–189, 2001.

Barth, M. C., A. L. Stuart, and W. C. Skamarock, Numerical simulations of the July 10, 1996, Stratospheric-Tropsopheric Experiment: Radiation, Aerosols, and Ozone (STERAO)-Deep Convection experiment storm: Redistribution of soluble tracers, *J. Geophys. Res.*, *106*, 2001, 2001.

Benner, T. C., and K. F. Evans, Three-dimensional solar radiative transfer in small tropical cumulus fields derived from high-resolution imagery, *J. Geophys. Res.*, *106*, 14,975–14,984, 2001.

Berkvens, P. J. F., M. A. Botchev, J. G. Verwer, M. C. Krol, and W. Peters, Solving vertical transport and chemistry in air pollution models, Report MAS-R0023, CWI, Amsterdam, 2000, available via the Internet: http://www.cwi.nl/static/publications/reports/reports.html.

Bohren, C. F., and D. R. Huffman, *Absorption and Scattering of Light by Small Particles*, Wiley Science, 1983.

Bond, T. C., T. L. Anderson, and D. Campbell, Calibration and intercomparison of filter-based measurements of visible light absorption by aerosol, *Aer. Sci. Tech.*, *30*, 582–600, 1999.

Borde, R., and H. Isaka, Radiative transfer in multifractal clouds, *J. Geophys. Res.*, *101*, 29,461–29,478, 1996.

Boucher, O., On aerosol direct shortwave forcing and the Henyey–Greenstein phase function, *J. Atmos. Sci.*, *55*, 128–134, 1998.

Brasseur, G. P., D. A. Hauglustaine, S. Walters, P. J. Rasch, J.-F. Müller, C. Granier, and X. X. Tie, MOZART, a global chemical transport model for ozone and related chemical tracers, 1. Model description, *J. Geophys. Res.*, *103*, 28,265–28,289, 1998.

Brasseur, G. P., J. J. Orlando, and G. S. Tyndall (Eds.), *Atmospheric Chemistry and Global Change*, Oxford University Press, 1999.

Briegleb, B. P., P. Minnis, V. Ramanathan, and E. Harrison, Comparison of regional clear-sky albedos inferred from satellite observations and model computations, *J. Climate Appl. Meteor.*, *25*, 214–226, 1986.

Browell, E. V., et al., Ozone and aerosol distribution and air mass characteristics over the South Atlantic Basin during the burning season, *J. Geophys. Res.*, *101*, 24,043–24,068, 1996.

Cahalan, R. F., W. Rodgway, W. J. Wiscombe, T. L. Bell, and J. B. Snider, The albedo of fractal stratocumulus clouds, *J. Atmos. Sci.*, *51*, 2434–2455, 1994.

Cairns, B., A. A. Lace, and B. E. Charlson, Absorption within inhomogeneous clouds and its parameterization in general circulation models, *J. Atmos. Sci.*, *57*, 700–714, 2000.

Capaldo, K. P., C. Plinis, and S. N. Pandis, A computationally efficient hybrid approach for dynamic gas/aerosol transfer in air quality models, *Atmos. Environ.*, *34*, 3617–3627, 2000.

Cess, R. D., et al., Absorption of solar radiation by clouds: Observations versus models, *Science*, *267*, 496–499, 1995.

Chatfield, R. B., and A. C. Delany, Convection links biomass burning to increased tropical ozone: However, models will tend to overpredict O_3, *J. Geophys. Res.*, *95*, 18,473–18,488, 1990.

Chatfield, R. B., J. A. Vastano, L. Li, G. W. Sachse, and V. S. Connors, The Great African plume from biomass burning: Generalizations from a three-dimensional study of TRACE A carbon monoxide, *J. Geophys. Res.*, *103*, 28,059–28,077, 1998.

Chu, D. A., Y. J. Kaufman, L. A. Remer, and B. N. Holben, Remote sensing of smoke from MODIS airborne simulator during the SCAR-B experiment, *J. Geophys. Res.*, *103*, 31,979–31,987, 1998.

Clark, T. L., M. A. Jenkins, J. Coen, and D. Packham, A coupled atmosphere-fire model: Convective feedback on fire-line dynamics, *J. Appl. Meteorol.*, *35*, 875–901, 1996.

CODIAC, Joss (joint office for science support) data system, 1999, available on the internet: http://www.joss.ucar.edu/codiac/.

Connors, V. S., B. B. Gormsen, S. Nolf, and H. G. Reichle, Jr., Spaceborne observations of the global distribution of carbon monoxide in the middle troposphere during April and October 1994, *J. Geophys. Res.*, *104*, 21,455–21,470, 1999.

Crowley, W. P., Numerical advection experiments, *Mon. Weath. Rev.*, *96*, 1–11, 1968.

Crutzen, P., and G. Carmichael, Modeling the influence of fires on atmospheric chemistry, in *Fire in the Environment: The Ecological, Atmospheric, and Climatic Importance of Vegetation Fires*, edited by P. Crutzen and J. Goldammer, pp. 89–105, John Wiley & Sons Ltd., 1993.

Crutzen, P. J., and M. O. Andreae, Biomass Burning in the Tropics: Impact on Atmospheric Chemistry and Biogeochemical Cycles, *Science*, *250*, 1669–1678, 1990.

Crutzen, P. J., L. E. Heidt, J. P. Krasnec, W. H. Pollock, and W. Seiler, Biomass burning as a source of atmospheric gases CO, H_2, N_2O, NO, CH_3Cl and COS, *Nature*, *282*, 253–256, 1979.

Crutzen, P. J., M. G. Lawrence, and U. Pöschl, On the background photochemistry of tropospheric ozone, *Tellus*, *51 A-B*, 123–146, 1999.

Curtis, A. R., and W. P. Sweetenham, Facsimile user's manual, *Tech. rep.*, Computer Science and Systems Division, Harwell Lab., Oxfordshire, Great Britain, 1987.

Damian-Iordache, V., KPP - chemistry simulation development environment, Master's thesis, University of Iowa, 1996, available via the Internet: http://www.cs.mtu.edu/ asandu/Software/software.html.

de Gouw, J. A., and E. R. Lovejoy, Reactive uptake of ozone by liquid organic compounds, *Geophys. Res. Lett.*, *25*, 931–934, 1998.

Delmas, R., J. P. Lacaux, J. C. Menaut, L. Abbadie, X. Le Roux, G. Helas, and J. Lobert, Nitrogen compound emission from biomass burning in tropical african savanna FOS/DECAFE 1991 experiment (Lamto, Ivory Coast), *J. Atmos. Chem.*, *22*, 175–193, 1995.

Delmas, R. A., et al., Experiment for regional sources and sinks of oxidants (EXPRESSO): An overview, *J. Geophys. Res.*, *104*, 30,609–30,624, 1999.

DeMore, W. B., S. P. Sander, D. M. Golden, R. F. Hampson, M. J. Kurylo, C. J. Howard, A. R. Ravishankara, C. E. Kolb, and M. J. Molina, Chemical Kinetics and Photochemical Data for Use in Stratospheric Modeling, Evaluation 12, NASA JPL Pub. 97-4, 1997.

Dickerson, R. R., S. Kondragunta, G. Stenchikov, K. L. Civerolo, B. G. Doddridge, and B. N. Holben, The impact of aerosols on solar ultraviolet radiation and photochemical smog, *Science*, *278*, 827–830, 1997.

Draine, B. T., and P. J. Flatau, Discrete dipole approximation for scattering calculations, *J. Opt. Soc. Am. A*, *11*, 1491–1499, 1994.

Dransfield, T. J., K. K. Perkins, N. M. Donahue, J. G. Anderson, M. M. Sprengnether, and K. L. Demerjian, Temperature and pressure dependent kinetics of the gas-phase reaction of the hydroxyl radical with nitrogen dioxide, *Geophys. Res. Lett.*, *26*, 687–690, 1999.

Duynkerke, P., P. Jonker, A. C. M. van Zanten, J. Cuxart, P. Clark, E. Sanchez, G. Martin, G. Lenderink, and J. Teixeira, Intercomparison of three- and one-dimensional model simulations and aircraft observations of stratocumulus, *Boundary-Layer Meteorology*, *92*, 453–487, 1999.

Dwyer, E., J.-M. Grégoire, and J.-P. Malingreau, A global analysis of vegetation fires using satellite images: Spatial and temporal dynamics, *Ambio*, *27*, 175–181, 1998.

Emmons, L. K., D. A. Hauglustaine, J.-F. Müller, M. A. Carroll, G. P. Brasseur, D. Brunner, J. Staehelin, V. Thouret, and A. Marenco, Data composites of airborne observations of tropospheric ozone and its precursors, *J. Geophys. Res.*, *105*, 20,497–20,538, 2000.

Evans, K. F., The spherical harmonics discrete ordinate method for three-dimensional atmospheric radiative transfer, *J. Atmos. Sci.*, *55*, 429–446, 1998.

Evans, L. F., N. K. King, D. R. Packham, and E. T. Stephens, Ozone measurements in smoke from forest fires, *Environ. Sci. Technol.*, *8*, 75–76, 1974.

Evans, L. F., I. A. Weeks, A. J. Eccleston, and D. R. Packham, Photochemical ozone in smoke from prescribed burning of forests, *Environ. Sci. Technol.*, *11*, 896–900, 1977.

Fenn, M., et al., Ozone and aerosol distributions and air mass characteristics over the South Pacific during the burning season, *J. Geophys. Res.*, *104*, 16,197–16,212, 1999.

Fenn, R. W., S. A. Clough, W. O. Gallery, R. E. Good, F. X. Kneizys, J. D. Mill, L. S. Rothmann, E. P. Shettle, and F. E. Volz, Optical and infrared properties of the atmosphere, in *Handbook of Geophysics and the Space Environment*, edited by A. Jursa, pp. 18–1–18–27, Air Force Geophysics Laboratory Hanscon Air Force Base, Bedford, M.A., 1985.

Ferek, R. J., J. S. Reid, P. V. Hobbs, D. R. Blake, and C. Liousse, Emission factors of hydrocarbons, halocarbons, trace gases and particles from biomass burning in Brazil, *J. Geophys. Res.*, *103*, 32,107–32,118, 1998.

Ferguson, S. A., D. V. Sandberg, and R. Ottmar, Modelling the effects of land-use changes on global biomass emissions, in *Biomass burning and its inter-relationships with the climate system*, edited by J. L. Innes, M. Beniston, and M. M. Verstraete, pp. 33–50, Kluwer Academic Publishers, 2000.

Fishman, J., and V. G. Brackett, The climatological distribution of tropospheric ozone derived from satellite measurements using version 7 Total Ozone Mapping Spectrometer and Stratospheric Aerosol and Gas Experiment data sets, *J. Geophys. Res.*, *102*, 19,275–19,278, 1997.

Fishman, J., C. E. Watson, J. C. Larsen, and J. A. Logan, Distribution of tropospheric ozone determined from satellite data, *J. Geophys. Res.*, *95*, 3599–3617, 1990.

Fishman, J., K. Fakhruzzaman, B. Cros, and D. Nganga, Identification of widespread pollution in the Southern Hemisphere deduced from satellite analyses, *Science*, *252*, 1693–1696, 1991.

Fishman, J., J. M. Hoell Jr., R. D. Bendura, R. J. McNeal, and V. W. J. H. Kirchhoff, NASA GTE TRACE A Experiment (September-October 1992): Overview, *J. Geophys. Res.*, *101*, 23,865–23,879, 1996.

Friedli, H. R., E. Atlas, V. R. Stroud, L. Giovanni, T. Campos, and L. F. Radke, Volatile organic trace gases emitted from North American wildfires, *Global Biogeochem. Cycles*, *15*, 435–452, 2001.

Gabriel, P. M., S.-C. Tsay, and G. L. Stephens, A Fourier-Riccati approach to radiative transfer. Part I: Foundations, *J. Atmos. Sci.*, *50*, 3125–3147, 1993.

Galanter, M., H. Levy II, and G. R. Carmichael, Impacts of biomass burning on tropospheric CO, NO_x, and O_3, *J. Geophys. Res.*, *105*, 6633–6653, 2000.

Gassó, S., and D. A. Hegg, Comparison of columnar aerosol optical properties measured by the MODIS Airborne Simulator with *in situ* measurements: A case study, *Remote Sens. Environ.*, *66*, 138–152, 1998.

Gear, C. W., The automatic integration of ordinary differential equations, *Numer. Math.*, *14*, 176–179, 1971.

Gierczak, T., J. B. Burkholder, S. Bauerle, and A. R. Ravishankara, Photochemistry of acetone under tropospheric conditions, *Chem. Phys.*, *231*, 229–244, 1998.

Goode, J. G., R. J. Yokelson, R. A. Susott, and D. E. Ward, Trace gas emissions from laboratory biomass fires measured by open-path Fourier transform infrared spectroscopy: Fires in grass and surface fuels, *J. Geophys. Res.*, *104*, 21,237–21,245, 1999.

Goode, J. G., R. J. Yokelson, D. E. Ward, R. A. Susott, R. E. Babbitt, M. A. Davis, and W. M. Hao, Measurements of excess O_3, CO_2, CO, CH_4, C_2H_4, C_2H_2, HCN, NO, NH_3, HCOOH, CH_3COOH, HCHO, and CH_3OH in 1997 Alaskan biomass burning plumes by airborne Fourier transform infrared spectroscopy (AFTIR), *J. Geophys. Res.*, *105*, 22,147–22,166, 2000.

Graf, H.-F., M. Herzog, J. M. Oberhuber, and C. Textor, The effect of environmental conditions on volcanic plume rise, *J. Geophys. Res.*, *104*, 24,309–24,320, 1999.

Graf, H.-F., D. Rosenfeld, and F. J. Nober, Sensitivity of global climate to the detrimental impact of smoke on rain clouds, Report No. 315, MPI for Meteorology, Hamburg, 2001.

Granier, C., J.-F. Müller, and G. Brasseur, The impact of biomass burning on the global budget of ozone and ozone precursors, in *Biomass Burning and its Inter-Relationship with the Climate System*, edited by J. L. Innes, M. Beniston, and M. M. Verstraete, pp. 69–85, Kluwer Academic Publishers, 2000.

Grant, K. E., C. C. Chuang, A. S. Grossman, and J. E. Penner, Modeling the spectral optical properties of ammonium sulfate and biomass burning aerosols: parameterization of relative humidity effects and model results, *Atmos. Environ.*, *33*, 2603–2620, 1999.

Green, R. O., et al., Imaging spectroscopy and the airborne visible/infrared imaging spectrometer (AVIRIS), *Remote Sens. Environ.*, *65*, 227–248, 1998.

Griffith, D. W., W. G. Mankin, M. T. Coeffey, D. E. Ward, and A. Riebau, FTIR remote sensing of biomass burning emissions of CO_2, CO, CH_4, CH_2O, NO, NO_2, NH_3, and N_2O, in *Global Biomass Burning: Atmospheric, Climatic, and Biospheric Implications*, edited by J. S. Levine, pp. 230–239, MIT Press, Cambridge, Mass., 1991.

Grishin, A. M., Mathematical modelling of forest fires, in *Fire in Ecosystems of Boreal Eurasia*, edited by J. Goldammer and V. Furyaev, pp. 285–302, Kluwer Academic, 1996.

Halthore, R. N., and S. E. Schwartz, Comparison of model-estimated and measured diffuse downward irradiance at surface in cloud-free skies, *J. Geophys. Res.*, *105*, 20,165–20,177, 2000.

Hao, W. M., and M.-H. Liu, Spatial and temporal distribtion of tropical biomass burning, *Global Biogeochem. Cycles*, *8*, 495–503, 1994.

Harriss, R. C., S. C. Wofsy, J. M. Hoell, Jr., R. J. Bendura, J. W. Drewry, R. J. McNeal, D. Pierce, V. Rabine, and R. L. Snell, The Arctic Boundary Layer Experiemnt (ABLE-3B): July-August 1990, *J. Geophys. Res.*, *99*, 1635–1643, 1994.

Hauglustaine, D. A., G. P. Brasseur, S. Walters, P. J. Rasch, J.-F. Müller, L. K. Emmons, and M. A. Carroll, MOZART, a global chemical transport model for ozone and related chemical tracers, 1. Model results and evaluation, *J. Geophys. Res.*, *103*, 28,291–28,335, 1998.

He, S., and G. R. Carmichael, Sensitivity of photolysis rates and ozone production in the troposphere to aerosol properties, *J. Geophys. Res.*, *104*, 26,307–26,324, 1999.

Heintzenberg, J., R. J. Charlson, A. D. Clarke, C. Liousse, V. Ramaswamy, K. P. Shine, M. Wendisch, and G. Helas, Measurements and modelling of aerosol single-scattering albedo: Progress, problems and prospects, *Beitr. Phys. Atmosph.*, *70*, 249–263, 1997.

Helas, G., et al., Ozone production due to emissions from vegetation burning, *J. Atmos. Chem.*, *22*, 163–174, 1995.

Herring, J. A., and P. V. Hobbs, Radiatively driven dynamics of the plume from 1991 Kuwait oil fires, *J. Geophys. Res.*, *99*, 18,809–18,826, 1994.

Herzog, M., H.-F. Graf, C. Textor, and J. M. Oberhuber, The effect of phase changes of water on the development of volcanic plumes, *J. Volcanol. Geotherm. Res*, *87*, 55–74, 1998.

Hobbs, P. V., and J. D. Locatelli, Ice nuclei from a natural forest fire, *J. Appl. Meteorol.*, *8*, 833–834, 1969.

Hobbs, P. V., and L. F. Radke, Cloud condensation nuclei from a simulated forest fire, *Science*, *163*, 279–280, 1969.

Hobbs, P. V., L. F. Radke, J. H. Lyons, R. J. Ferek, D. J. Coffman, and T. J. Casadevall, Airborne measurements of particles and gas emissions from the 1990 volcanic eruptions of Mount Redoubt, *J. Geophys. Res.*, *96*, 18,735–18,752, 1991.

Hobbs, P. V., J. S. Reid, J. A. Herring, J. D. Nance, R. E. Weiss, J. L. Ross, D. A. Hegg, R. D. Ottmar, and C. Liousse, Particle and trace-gas measurements in the smoke from prescribed burns of forest products in the Pacific Northwest, in *Biomass Burning and Global Change*, edited by J. S. Levine, pp. 697–715, MIT Press, Cambridge, Mass., 1996.

Holben, B. N., Y. J. Kaufman, A. W. Setzer, D. D. Tanre, and D. E. Ward, Optical properties of aerosol emissions from biomass burning in the tropics, BASE-A, in *Global Biomass Burning: Atmospheric, Climatic, and Biospheric Implications*, edited by J. S. Levine, pp. 403–411, MIT Press, Cambridge, Mass., 1991.

Holzinger, R., C. Warneke, A. Hansel, A. Jordan, W. Lindinger, D. Scharffe, G. Schade, and P. J. Crutzen, Biomass burning as a source of formaldehyde, acetaldehyde, methanol, acetone, acetonitrile, and hydrogen cyanide, *Geophys. Res. Lett.*, *26*, 1161–1164, 1999.

Horowitz, L. W., J. Liang, G. M. Gardner, and D. J. Jacob, Export of reactive nitrogen from North America during summertime: Sensitivity to hydrocarbon chemistry, *J. Geophys. Res.*, *103*, 13,451–13,476, 1998.

Horvath, H., Atmospheric light absorption - A review, *Atmos. Environ.*, *27A*, 293–317, 1993.

Jacob, D. J., et al., Summertime photochemistry of the troposphere at high northern latitudes, *J. Geophys. Res.*, *97*, 16,421–16,431, 1992.

Jacobson, M. Z., Studying the effect of aerosols on vertical photolysis rate coefficient and temperature profiles over an urban airshed, *J. Geophys. Res.*, *103*, 10,593–10,604, 1998a.

Jacobson, M. Z., *Fundamentals of Atmospheric Modeling*, Cambridge University Press, 1998b.

Jenkin, M. E., and K. C. Clemitshaw, Ozone and other secondary photochemical pollutants: chemical processes governing their formation in the planetary boundary layer, *Atmos. Environ.*, *34*, 2499–2527, 2000.

Jones, N. B., C. P. Rinsland, J. B. Liley, and J. Rosen, Correlation of aerosol and carbon monoxide at 45°S: Evidence of biomass burning emissions, *Geophys. Res. Lett.*, *28*, 709–712, 2001.

Junkermann, W., et al., Actinic radiation and photolysis processes in the lower troposphere: Effect of clouds and aerosols, accepted for publication in the *J. Atmos. Chem.*, 2001.

Kato, S., T. P. Ackermann, E. E. Clothiaux, J. H. Mather, G. G. Mace, M. L. Wesely, F. Murcray, and J. Michalsky, Uncertainties in modeled and measured clear-sky surface shortwave irradiances, *J. Geophys. Res.*, *102*, 25,881–25,898, 1997.

Kaufman, Y. J., and R. S. Fraser, The effect of smoke particles on clouds and climate forcing, *Science*, *277*, 1636–1639, 1997.

Kaufman, Y. J., and T. Nakajima, Effect of Amazon smoke on cloud microphysics and albedo – Analysis from satellite imaginery, *J. Appl. Meteorol.*, *32*, 729–744, 1993.

Kaufman, Y. J., D. Tanré, O. Dubovik, A. Karnieli, and L. A. Remer, Absorption of sunlight by dust as inferred from satellite and ground-based remote sensing, *Geophys. Res. Lett.*, *28*, 1479–1482, 2001.

Kaufman, Y. J., et al., Relationship between remotely sensed fire intensity and rate of emission of smoke: SCAR-C experiment, in *Biomass Burning and Global Change*, edited by J. S. Levine, pp. 685–696, MIT Press, Cambridge, Mass., 1996.

Kaufman, Y. J., et al., Smoke, Clouds, and Radiation-Brazil (SCAR-B) experiment, *J. Geophys. Res.*, *103*, 31,783–31,808, 1998.

Kent, G. S., C. R. Trepte, K. M. Skeens, and D. M. Winker, LITE and SAGE II measurements of aerosols in the southern hemisphere upper troposphere, *J. Geophys. Res.*, *103*, 19,111–19,127, 1998.

Key, J. R., Streamer user's guide, *Tech. Rep. 96-01*, Department of Geography, Boston University, 1999, available via the Internet: http://stratus.ssec.wisc.edu/streamer/streamer.html.

Kirchner, F., and W. R. Stockwell, Effect of peroxy radical reactions on the predicted concentrations of ozone, nitrogenous compounds, and radicals, *J. Geophys. Res.*, *101*, 21,007–21,022, 1996.

Kleffmann, J., K. H. Becker, and P. Wiesen, Heterogeneous NO_2 conversion processes on acid surfaces: Possible atmospheric implications, *Atmos. Environ.*, *32*, 2721–2729, 1998.

Kleinmann, L. I., P. H. Daum, J. H. Lee, Y.-N. Lee, L. J. Nunnermacker, S. R. Springston, L. Newmann, J. Weinstein-Lloyd, and S. Sillman, Dependence of ozone production on NO and hydrocarbons in the troposphere, *Geophys. Res. Lett.*, *24*, 2299–2302, 1997.

Koppmann, R., A. Khedim, J. Rudolf, D. Poppe, M. O. Andreae, G. Helas, M. Welling, and T. Zenker, Emissions of organic trace gases from savanna fires in southern Africa during the 1992 Southern African Fire Atmosphere Research Initiative and their impact on the formation of tropospheric ozone, *J. Geophys. Res.*, *102*, 18,879–18,888, 1997.

Kotchenruther, R. A., and P. V. Hobbs, Humidification factors of aerosols from biomass burning in Brazil, *J. Geophys. Res.*, *103*, 32,081–32,089, 1998.

Krekov, G. M., Models of atmospheric aerosols, in *Aerosol Effects on Climate*, edited by S. G. Jenkins, pp. 9–72, The University of Arizona Press, 1992.

Krol, M. C., M. J. Molemaker, and J. Vilà Guerau de Arellano, Effects of turbulence and heterogeneous emissions on the photochemically active species in the convective boundary layer, *J. Geophys. Res.*, *105*, 6871–6884, 2000.

Lacaux, J. P., et al., Biomass burning in the tropical savannas of the Ivory Coast: An overview of the field experiement Fire Of Savannas (FOS/DECAFE '91), *J. Atmos. Chem.*, *22*, 195–216, 1995.

Landgraf, J., and P. Crutzen, An efficient method for online calculations of photolysis and heating rates, *J. Atmos. Sci.*, *55*, 863–878, 1998.

Langmann, B., M. Herzog, and H.-F. Graf, Radiative forcing of climate by sulfate aerosols as determined by a regional circulation chemistry transport model, *Atmos. Environ.*, *32*, 2757–2768, 1998.

Lawrence, M. G., P. J. Crutzen, P. J. Rasch, B. E. Eaton, and N. M. Mahowald, A model for studies of tropospheric photochemistry: Description, and global distributions, and evaluation, *J. Geophys. Res.*, *104*, 26,245–26,277, 1999.

Lawrence, M. G., P. Jöckel, and R. von Kuhlmann, What does the global mean OH concentration tell us?, *Atmos. Chem. Phys.*, *1*, 37–49, 2001.

LeBel, P. J., W. R. Cofer, J. S. Levine, S. A. Vay, and P. D. Roberts, Nitric acid and ammonia emissions from a mid-latitude prescribed wetland fire, *Geophys. Res. Lett.*, *15*, 792–795, 1988.

LeBel, P. J., S. A. Vay, and P. D. Roberts, Ammonia and nitric acid emissions from wetlands and boreal forest fires, in *Global Biomass Burning: Atmospheric, Climatic, and Biospheric Implications*, edited by J. S. Levine, pp. 225–229, MIT Press, Cambridge, Mass., 1991.

Lefer, B. L., et al., Enhancement of acidic gases in biomass burning impacted air masses over Canada, *J. Geophys. Res.*, *99*, 1721–1737, 1994.

Lelieveld, J., and F. J. Dentener, What controls tropospheric ozone?, *J. Geophys. Res.*, *105*, 3531–3551, 2000.

Liao, H., Y. L. Yung, and J. H. Seinfeld, Effects of aerosols on tropospheric photolysis rates in clear and cloudy atmospheres, *J. Geophys. Res.*, *104*, 23,697–23,707, 1999.

Lin, X., M. Trainer, and S. C. Liu, On the nonlinearity of the tropospheric ozone production, *J. Geophys. Res.*, *93*, 15,879–15,888, 1988.

Lindesay, J. A., M. O. Andreae, J. G. Goldammer, G. Harris, H. J. Annegarn, M. Garstang, and R. J. S. an B. W. van Wilgen, International Geosphere-Biosphere Programme/International Global Atmospheric Chemistry SAFARI-92 field experiment: Background and overview, *J. Geophys. Res.*, *101*, 23,521–23,530, 1996.

Liousse, C., J. Penner, C. Chuang, J. Walton, H. Eddleman, and H. Cachier, A global three-dimensional model study of carbonaceous aerosols, *J. Geophys. Res.*, *101*, 19,411–19,432, 1996.

Liu, S. C., M. Trainer, F. C. Fehsenfeld, D. D. Parrish, E. J. Williams, D. W. Fahey, G. Hübler, and P. C. Murphy, Ozone production in the rural troposphere and the implications for regional and global ozone distribution, *J. Geophys. Res.*, *92*, 4191–4207, 1987.

Lobert, J., and J. Warnatz, Emissions from combustion process in vegetation, in *Fire in the Environment: The Ecological, Atmospheric, and Climatic Importance of Vegetation Fires*, edited by P. Crutzen and J. Goldammer, pp. 15–37, John Wiley & Sons Ltd., 1993.

Lobert, J., W. C. Keene, J. A. Logan, and R. Yevich, Global chlorine emissions from biomass burning: Reactive Chlorine Emissions Inventory, *J. Geophys. Res.*, *104*, 8373–8389, 1999.

Lobert, J. M., D. H. Scharffe, W.-M. Hao, T. A. Kuhlbusch, R. Seuwen, P. Warneck, and P. J. Crutzen, Experimental evaluation of biomass burning emissions: Nitrogen and carbon containing compounds, in *Global Biomass Burning: Atmospheric, Climatic, and Biospheric Implications*, edited by J. S. Levine, pp. 289–304, MIT Press, Cambridge, Mass., 1991.

Los, A., M. van Weele, and P. G. Duynkerke, Actinic fluxes in broken cloud fields, *J. Geophys. Res.*, *102*, 4257–4266, 1997.

Loughlin, P. E., T. Trautmann, A. Bott, W. G. Panhans, and W. Zdunkowski, The effect of different radiation parameterizations on cloud evolution, *Q. J. R. Meteorol. Soc.*, *123*, 1985–2007, 1997.

Lu, R., C. Lin, R. Turco, and A. Arakawa, Cumulus transport of chemical tracers 1. Cloud-resolving model simulations, *J. Geophys. Res.*, *105*, 10,001–10,021, 2000.

Lurmann, F. W., A. C. Lloyd, and R. Atkinson, A chemical mechanism for use in long-range transport/acid deposition computer modelling, *J. Geophys. Res.*, *91*, 10,905–10,936, 1986.

Lyapustin, A. I., and Y. J. Kaufman, Role of adjacency effect in the remote sensing of aerosol, *J. Geophys. Res.*, *106*, 11,909–11,916, 2001.

Madronich, S., Photodissociation in the atmosphere, 1. Actinic flux and effects of ground reflections and clouds, *J. Geophys. Res.*, *92*, 9740–9752, 1987.

Manis, P. C., Cloud heights and stratospheric injections resulting from a thermonuclear war, *Atmos. Environ.*, *19*, 1245–1255, 1985.

Marchuk, G. I., G. A. Mikhailiv, M. A. Nazaraliev, R. A. Darbinjan, B. A. Kargina, and B. S. Elepov, *The Monte Carlo Methods in Atmospheric Optics, Springer Ser. Opt. Sci., vol. 12*, Springer-Verlag, New York, 1980.

Mari, C., D. J. Jacob, and P. Bechtold, Transport and scavenging of soluble gases in a deep convective cloud, *J. Geophys. Res.*, *105*, 22,255–22,267, 2000.

Marion, T., P. E. Perros, R. Losno, and E. Steiner, Ozone production efficiency in savanna and forested areas during the EXPRESSO experiment, *J. Atmos. Chem.*, *38*, 3–30, 2001.

Marshak, A., A. Davis, W. Wiscombe, and R. Cahalan, Radiative smoothing in fractal clouds, *J. Geophys. Res.*, *100*, 26,247–26,261, 1995.

Martins, J. V., P. Artaxo, P. V. Hobbs, C. Liousse, H. Cachier, Y. Kaufman, and A. Plana-Fattori, Particle size distribution, elemental composition, carbon measurements, and optical properties of smoke from biomass burning in the Pacific Northwest of the United States, in *Biomass Burning and Global Change*, edited by J. S. Levine, pp. 716–732, MIT Press, Cambridge, Mass., 1996.

Martins, J. V., P. Artaxo, C. Liousse, J. S. Reid, P. V. Hobbs, and Y. J. Kaufman, Effects of black carbon content, particles size, and mixing on light absorption by aerosols from biomass burningin Brazil, *J. Geophys. Res.*, *103*, 32,041–32,050, 1998.

Marufu, L., F. Dentener, J. Lelieveld, M. O. Andreae, and G. Helas, Photochemistry of the African troposphere: Influence of biomass-burning emissions, *J. Geophys. Res.*, *105*, 14,513–14,530, 2000.

Mason, S. A., R. F. Field, R. J. Yokelson, M. A. Kochivar, M. R. Tinsley, D. E. Ward, and W. M. Hao, Complex effects arising in smoke plume simulations due to inclusion of direct emissions of oxygenated organic species from biomass combustion, *J. Geophys. Res.*, *106*, 12,527–12,539, 2001.

Mauzerall, D. L., D. J. Jacob, S.-M. Fan, J. D. Bradshaw, G. L. Gregory, G. W. Sachse, and D. R. Blake, Origin of tropospheric ozone at remote high northern latitudes in summer, *J. Geophys. Res.*, *101*, 4175–4188, 1996.

Mauzerall, D. L., et al., Photochemistry in biomass burning plumes and implications for tropospheric ozone over the tropical South Atlantic, *J. Geophys. Res.*, *103*, 8401–8423, 1998.

Mayol-Bracero, O. L., P. Guyon, B. Graham, G. Roberts, M. O. Andreae, S. Decesari, M. C. Facchini, S. Fuzzi, and P. Artaxo, Water-soluble organic compounds in biomass burning aerosols over amazonia: 2. Apportionment of the chemical composition and importance of the polyacidic fraction, submitted to *J. Geophys. Res.*, 2001.

McCarter, R. J., and A. Broido, Radiative and convective energy from wood crib fires, *Pyrodynamics*, *2*, 65–85, 1965.

McDow, S. R., M. Jang, Y. Hong, and R. M. Kamens, An approach to studying the effect of organic composition on atmospheric aerosol photochemistry, *J. Geophys. Res.*, *101*, 19,539–19,600, 1996.

McKee, D. J. (Ed.), *Tropospheric Ozone, Human Health, and Agricultural Impacts*, Lewis, Boca Raton, Flo., 1993.

Meerkötter, R., and M. Degünther, A radiative transfer case study for 3-d cloud effects in the UV, *Geophys. Res. Lett.*, *28*, 1683–1686, 2001.

Müller, F., Estimation of the error due to operator splitting for micro-physical-multiphase chemical systems in meso-scale air quality models, Report No. 314, MPI for Meteorology, Hamburg, 2000.

Nenes, A., S. N. Pandis, and C. Plinis, Continued development and testing of a new therodynamic aerosol module for urban and regional air quality models, *Atmos. Environ.*, *33*, 1553–1560, 1999.

Novakov, T., and C. E. Corrigan, Thermal characterization of biomass smoke particles, *Mikrochim. Acta*, *119*, 157–166, 1995.

Oberhuber, J. M., M. Herzog, H.-F. Graf, and K. Schwanke, Volcanic plume simulation on large scales, *J. Volcanol. Geotherm. Res*, *87*, 29–53, 1998.

O'Hirok, W., and C. Gautier, A three-dimensional radiative transfer model to investigate the solar radiation within a cloudy atmosphere. Part I: Spatial effects, *J. Atmos. Sci.*, *55*, 2162–2179, 1998a.

O'Hirok, W., and C. Gautier, A three-dimensional radiative transfer model to investigate the solar radiation within a cloudy atmosphere. Part II: Spectral effects, *J. Atmos. Sci.*, *55*, 3065–3076, 1998b.

Orlando, J. J., G. S. Tyndall, M. Bilde, C. Ferronato, T. J. Wallington, L. Vereecken, and J. Peeters, Laboratory and theoretical study of the oxy radicals in the OH- and Cl-initiated oxidation of ethene, *J. Phys. Chem. A*, *102*, 8116–8123, 1998.

Parrish, D. D., J. S. Holloway, M. Trainer, P. C. Murphy, G. L. Forbes, and F. C. Fehsenfeld, Export of North American ozone pollution to the North Atlantic Ocean, *Science*, *259*, 1436–1439, 1993.

Penner, J. E., L. C. Haselman, Jr., and L. L. Edwards, Smoke-plume distribution above large-scale fires: Implications for simulations of "Nuclear Winter", *J. Climate and Appl. Meteorol.*, *25*, 1434–1444, 1986.

Penner, J. E., M. M. Bradley, C. C. Chuang, L. L. Edwards, and L. F. Radke, A numerical simulation of the aerosol-cloud interaction and atmospheric dynamics of the hardiman township, ontario, prescribed burn, in *Global Biomass Burning: Atmospheric, Climatic, and Biospheric Implications*, edited by J. S. Levine, pp. 420–426, MIT Press, Cambridge, Mass., 1991.

Penner, J. E., et al., Aerosols, their direct and indirect effects, in *Climate Change 2001: The Scientific Basis. Contribution of Working Group I to the Third Assessment Report of the Intergovernmental Panel on Climate Change*, edited by J. T. Houghton, Y. Ding, D. J. Griggs, M. Noguer, P. J. van der Linden, X. Dai, K. Maskell, and C. A. Johnson, pp. 289–348, Cambridge University Press, Cambridge, United Kingdom and New York, NY, USA, 2001.

Petry, H., J. Hendricks, M. Möllhoff, E. Lippert, A. Meier, A. Ebel, and R. Sausen, Chemical conversion of subsonic aircraft emissions in the dispersing plume: Calculation of effective emission indices, *J. Geophys. Res.*, *103*, 5759–5772, 1998.

Petzold, A., and R. Niessner, Photoacoustic soot sensor for in-situ black carbon monitoring, *Appl. Phys. B*, *63*, 191–197, 1996.

Podgorny, I. A., A. M. Vogelmann, and V. Ramanathan, Effects of cloud shape and water vapor distribution on solar absorption in the near-infrared, *Geophys. Res. Lett.*, *25*, 1899–1902, 1998.

Poppe, D., R. Koppmann, and J. Rudolph, Ozone formation in biomass burning plumes: Influence of atmospheric dilution, *Geophys. Res. Lett.*, *25*, 3823–3826, 1998.

Pöschl, U., R. von Kuhlmann, N. Poisson, and P. J. Crutzen, Development and intercomparison of condensed isoprene oxidation mechanisms for global atmospheric modeling, *J. Atmos. Chem.*, *37*, 29–52, 2000.

Pueschel, R. F., and G. Langer, Sugar cane fires as a source of ice nuclei in Hawai, *J. Appl. Meteorol.*, *12*, 549–551, 1973.

Radke, L. F., J. L. Stith, D. A. Hegg, and P. V. Hobbs, Airborne studies of particles and gases from forest fires, *J. Air Pollut. Control Assoc.*, *28*, 30–34, 1978.

Radke, L. F., J. H. Lyons, P. V. Hobbs, and R. E. Weiss, Smokes from the burning of aviation fuel and their self-lofting by solar heating, *J. Geophys. Res.*, *95*, 14,071–14,076, 1990.

Radke, L. F., D. A. Hegg, P. V. Hobbs, J. D. Nance, J. H. Lyons, K. K. Laursen, R. E. Weiss, P. J. Riggan, and D. E. Ward, Particulate and trace gas emissions from large biomass fires in north america, in *Global Biomass Burning: Atmospheric, Climatic, and Biospheric Implications*, edited by J. S. Levine, pp. 209–224, MIT Press, Cambridge, Mass., 1991.

Ramanathan, V., B. Subasilar, G. J. Zhang, W. Conant, R. D. Cess, J. T. Kiehl, H. Grassl, and L. Shi, Warm pool heat budget and shortwave cloud forcing: A missing physics?, *Science*, *267*, 499–503, 1995.

Ramaswamy, V., O. Boucher, J. Haigh, D. Hauglustaine, J. Haywood, G. Myhre, T. Nakajima, G. Y. Shi, and S. Solomon, Radiative forcing of climate change, in *Climate Change 2001: The Scientific Basis. Contribution of Working Group I to the Third Assessment Report of the Intergovernmental Panel on Climate Change*, edited by J. T. Houghton, Y. Ding, D. J. Griggs, M. Noguer, P. J. van der Linden, X. Dai, K. Maskell, and C. A. Johnson, pp. 349–416, Cambridge University Press, Cambridge, United Kingdom and New York, NY, USA, 2001.

Reichle, H. G., V. S. Connors, J. A. Holland, W. D. Hypes, H. A. Wallio, J. C. Casas, B. B. Gormsen, and M. S. S. W. D. Hesketh, Middle and upper tropospheric carbon monoxide mixing ratios as measured by a satellite-borne remote sensor during November 1981, *J. Geophys. Res.*, *91*, 10,865–10,887, 1986.

Reid, J. S., Emission, evolution, and radiative properties of particles from biomass burning in brazil, Ph.D. thesis, University of Washington, 1998.

Reid, J. S., P. V. Hobbs, R. J. Ferek, D. R. Blake, J. V. Martins, M. R. Dunlap, and C. Liousse, Physical, chemical, and optical properties of regional hazes dominated by smoke in Brazil, *J. Geophys. Res.*, *103*, 32,059–32,080, 1998.

Remer, L. A., Y. J. Kaufman, B. N. Holben, A. M. Thompson, and D. McNamara, Biomass burning aerosol size distribution and modeled optical properties, *J. Geophys. Res.*, *103*, 31,879–31,891, 1998.

Rosenfeld, D., TRMM observed first direct evidence of smoke from forest fires inhibiting rainfall, *Geophys. Res. Lett.*, *26*, 3105–3108, 1999.

Ross, J. L., P. V. Hobbs, and B. Holben, Radiative characteristics of regional hazes dominated by smoke from biomass burning in Brazil: Closure tests and direct radiative forcing, *J. Geophys. Res.*, *103*, 31,925–31,941, 1998.

Ryerson, T. B., et al., Emissions lifetimes and ozone formation in power plant plumes, *J. Geophys. Res.*, *103*, 22,569–22,583, 1998.

Sandberg, D. V., and J. Peterson, A source strength model for prescribed fire in coniferous logging slash, in *Proceedings of the 21st annual meeting of the Air Pollution Control Association; 1984 November 12-14, Portland, Oregon*, 1984.

Sander, S. P., et al., Chemical Kinetics and Photochemical Data for Use in Stratospheric Modeling, Evaluation 13, Supplement to Evaluation 12: Update of Key Reactions, NASA JPL Pub. 00-3, available at http://jpldataeval.jpl.nasa.gov/, 2000.

Saunders, S. M., M. E. Jenkin, R. G. Derwent, and M. J. Pilling, World wide web side of a master chemical mechanism (MCM) for use in tropospheric chemistry models, *Atmos. Environ.*, *31*, 1249, 1997.

Seiler, W., and P. J. Crutzen, Estimates of gross and net fluxes of carbon between the biosphere and the atmosphere from biomass burning, *Clim. Change*, *2*, 207–247, 1980.

Seinfeld, J. H., and S. N. Pandis, *Atmospheric Chemistry and Physics: From Air Pollution to Climate Change*, John Wilsey & Sons, Inc., 1998.

Sillman, S., Ozone production efficiency and loss of NO_x in power plant plumes: Photochemical model and interpretation of measurements in Tennessee, *J. Geophys. Res.*, *105*, 9189–9202, 2000.

Sillman, S., J. A. Logan, and S. C. Wofsy, A regional scale model for ozone in the United States with subgrid representation of urban and power plant plumes, *J. Geophys. Res.*, *95*, 5731–5748, 1990.

Singh, H. B., et al., Biomass burning influences on the composition of the remote South Pacific troposphere: analysis based on observations from PEM-Tropics-A, *Atmos. Environ.*, *34*, 635–644, 2000.

Singh, H. N., et al., Summertime distribution of PAN and other reactive nitrogen species in the northern high-latitude atmosphere of eastern Canada, *J. Geophys. Res.*, *99*, 1821–1835, 1994.

Skamarock, W. C., et al., Numerical simulations of the July 10 Stratospheric-Tropospheric Experiment: Radiation, Aerosols, and Ozone/Deep Convection Experiment convective system: Kinematics and transport, *J. Geophys. Res.*, *105*, 19,973–19,990, 2000.

Sloane, C. S., Optical properties of aerosols – Comparison of measurements with model calculations, *Atmos. Environ.*, *17*, 409–416, 1983.

Smolarkiewicz, P. K., A fully multidimensinal positive definite advection transport algorithm with small implicit diffusion, *J. Comp. Phys.*, *54*, 325–362, 1984.

Spicer, C. W., Nitrogen oxide reactions in the urban plume of Boston, *Science*, *215*, 1095–1097, 1982.

Stamnes, K., S. Tsay, W. Wiscombe, and K. Jayaweera, Numerically stable algorithm for Discrete–Ordinate–Method: Radiative transfer in multiple scattering and emitting layered media, *Appl. Opt.*, *27*, 2502–2509, 1988.

Stevens, B., et al., Simulations of trade wind cumuli under a strong inversion, *J. Atmos. Sci.*, *58*, 1870–1891, 2001.

Stith, J. L., L. F. Radke, and P. V. Hobbs, Particle emissions and the production of ozone and nitrogen oxides from the burning of forest slash, *Atmos. Environ.*, *15*, 73–82, 1981.

Stockwell, W., F. Kirchner, M. Kuhn, and S. Seefeld, A new mechanism for regional atmospheric chemistry modeling, *J. Geophys. Res.*, *102*, 25,847–25,879, 1997.

Sutherland, R. A., and R. K. Khanna, Optical properties of organic-based aerosols produced by burning vegetation, *Aerosol Sci. Technol.*, *14*, 331–342, 1991.

Tabazadeh, A., M. Z. Jacobson, H. B. Singh, O. B. Toon, J. S. Lin, R. B. Chatfield, A. N. Thakur, R. W. Talbot, and J. E. Dibb, Nitric acid scavenging by mineral and biomass burning aerosol, *Geophys. Res. Lett.*, *25*, 4185–4188, 1998.

Tanré, D., Y. J. Kaufman, M. Herman, and S. Mattoo, Remote sensing of aerosol properties over oceans using the MODIS/EOS spectral radiances, *J. Geophys. Res.*, *102*, 16,971–16,988, 1997.

Tegen, I., P. Hollrig, M. Chin, I. Fung, D. Jacob, and J. Penner, Contribution of different aerosol species to the global aerosol extinction optical thickness: Estimates from model results, *J. Geophys. Res.*, *102*, 23,895–23,915, 1997.

Textor, C., Numerical simulation of scavenging processes in explosive volcanic eruption clouds, Ph.D. thesis, University Hamburg, 1999.

Thompson, A. M., J. C. Witte, R. D. Hudson, H. Guo, R. R. Herman, and M. Fujiwara, Tropical tropospheric ozone and biomass burning, *Science*, *291*, 2128–2132, 2001.

Toon, O. B., J. B. Pollack, and B. N. Khare, The optical constants of several atmospheric aerosol species: Ammonium Sulfate, Aluminium Oxide, and Sodium Chloride, *J. Geophys. Res.*, *81*, 5733–5748, 1976.

Trainer, M., D. D. Parrish, P. D. Goldan, J. Roberts, and F. C. Fehsenfeld, Review of observation-based analysis of the regional factors influencing ozone concentrations, *Atmos. Environ.*, *34*, 2000.

Trautmann, T., I. Podgorny, J. Landgraf, and P. J. Crutzen, Actinic fluxes and photodissociation coefficients in cloud fields embedded in realistic atmospheres, *J. Geophys. Res.*, *104*, 30,173–30,192, 1999.

Trentmann, J., B. Früh, O. Boucher, T. Trautmann, and M. O. Andreae, Three-dimensional solar radiation effects in a biomass burning plume, submitted to *J. Geophys. Res.*, 2001.

Trentmann, J., M. O. Andreae, H.-F. Graf, P. V. Hobbs, R. D. Ottmar, and T. Trautmann, Simulation of a biomass-burning plume: Comparison of model results with observations, accepted for publication in *J. Geophys. Res.*, 2002.

Twomey, S., Pollution and the planetary albedo, *Atmos. Environ.*, *8*, 1251–1256, 1974.

Tyndall, G. S., R. A. Cox, C. Granier, R. Lesclaux, G. K. Moortgat, M. J. Pilling, A. R. Ravishankara, and T. J.Wallington, Atmospheric chemistry of small organic peroxy radicals, *J. Geophys. Res.*, *106*, 12,157–12,182, 2001.

Valero, F. P., R. D. Cess, M. Zhang, S. K. Pope, A. Bucholtz, B. Bush, and J. Vitko, Jr., Absorption of solar radiation by the cloudy atmosphere: Interpretations of collocated aircraft measurements, *J. Geophys. Res.*, *102*, 29,917–29,927, 1997.

Várnai, T., and R. Davis, Effects of cloud heterogeneities on shortwave radiation: Comparison of cloud-top variabiliy and internal heterogeneity, *J. Atmos. Sci.*, *56*, 4206–4224, 1999.

Verwer, J. G., E. J. Spee, J. G. Blom, and W. H. Hundsdorfer, A second order Rosenbrock method applied to photochemical dispersion problems, Report MAS-R9717, CWI, Amsterdam, 1997, available via the Internet: http://www.cwi.nl/static/publications/reports/reports.html.

Verwer, J. G., E. J. Spee, J. G. Blom, and W. H. Hundsdorfer, A second order Rosenbrock method applied to photochemical dispersion problems, *SIAM J. Sci. Comp.*, *20*, 1456–1480, 1999.

Vilà-Guerau de Arellano, J., and J. W. M. Cuijper, The chemistry of a dry cloud: The effect of radiation and turbulence, *J. Atmos. Sci.*, *57*, 1573–1584, 2000.

Vogelmann, A. M., V. Ramanathan, and I. A. Podgorny, Scale dependence of solar heating rates in convective cloud systems with implications to general circulation models, *J. Climate*, *14*, 1738–1752, 2001.

von Kuhlmann, R., Tropospheric photochemistry of ozone, its precursors and the hydroxyl radical: A 3D-modeling study considering non-methane hydrocarbons, Ph.D. thesis, University Mainz, 2001.

Wahner, A., T. F. Mentel, and M. Sohn, Gas-phase reaction of N_2O_5 with water vapor: Importance of heterogeneous hydrolysis of N_2O_5 and surface desorption of HNO_3 in a large teflon chamber, *Geophys. Res. Lett.*, *25*, 2169–2172, 1998.

Waibel, A. E., H. Fischer, F. G. Wienhold, P. C. Siegmund, B. Lee, J. Ström, J. Lelieveld, and P. J. Crutzen, Highly elevated carbon monoxide concentrations in the upper troposphere and lowermost stratosphere at northern midlatitudes during the STREAM II summer campaign in 1994, *Chemosphere - Global Change Science*, *1*, 233–248, 1999.

Wang, Y., D. J. Jacob, and J. A. Logan, Global simulation of tropospheric O_3-NO_x-hydrocarbon chemistry: 1. Model formulation, *J. Geophys. Res.*, *103*, 10,713–10,725, 1998a.

Wang, Y., J. A. Logan, and D. J. Jacob, Global simulation of tropospheric O_3-NO_x-hydrocarbon chemistry: 2. Model evaluation and global ozone budget, *J. Geophys. Res.*, *103*, 10,727–10,755, 1998b.

Ward, D. E., et al., Smoke and fire characteristics for cerrado and deforestation burns in Brazil: BASE-B experiment, *J. Geophys. Res.*, *97*, 14,601–14,619, 1992.

Warneck, P., *Chemistry of the Natural Atmosphere*, Academic Press, 1999.

Watson, C., J. Fishman, and H. G. Reichle, Jr., The significance of biomass burning as a source of carbon monoxide and ozone in the southern hemisphere tropics: A satellite analysis, *J. Geophys. Res.*, *95*, 16,443–16,450, 1990.

Wehrli, C., World Radiation Center (WRC) Publication No. 615, Davos, Switzerland, 1985, available on the internet: ftp://ftp.pmodwrc.ch/publications/pmod615.asc.

Wendisch, M., and A. Keil, Discrepancies between measured and modeled solar and UV radiation within polluted boundary layer clouds, *J. Geophys. Res.*, *104*, 27,373–27,385, 1999.

Wild, M., Discrepancies between model-calculated and observed shortwave atmospheric absorption in areas with high aerosol loadings, *J. Geophys. Res.*, *104*, 27,361–27,371, 1999.

Wofsy, S. C., et al., Atmospheric chemistry in the arctic and subarctic: Influence of natural fires, industrial emissions, and stratospheric inputs, *J. Geophys. Res.*, *97*, 16,731–16,746, 1992.

Wollenhaupt, M., and J. N. Crowley, Kinetic studies of the reactions $CH_3 + NO_2 \longrightarrow$ Products, $CH_3O + NO_2 \longrightarrow$ Products, and $OH + CH_3C(O)CH_3 \longrightarrow CH_3C(O)OH + CH_3$, over the range of temperature and pressure, *J. Phys. Chem. A*, *104*, 6429–6438, 2000.

Wollenhaupt, M., S. A. Carl, A. Horowitz, and J. N. Crowley, Rate coefficients for reaction of OH with acetone between 202 and 395 K, *J. Phys. Chem. A*, *104*, 2695–2705, 2000.

Wotawa, G., and M. Trainer, The influnce of Canadian forest fire on pollutant concentrations in the United States, *Science*, *288*, 324–328, 2000.

Yokelson, R. J., D. W. Griffith, and D. E. Ward, Open-path Fourier transform infrared studies of large-scale laboratory biomass fire, *J. Geophys. Res.*, *101*, 21,067–21,080, 1996.

Yokelson, R. J., R. Susott, D. E. Ward, J. Reardon, and D. W. Griffith, Emissions from smoldering combustion of biomass measured by open-path Fourier transform infrared spectroscopy, *J. Geophys. Res.*, *102*, 18,865–1877, 1997.

Yokelson, R. J., J. G. Goode, D. E. Ward, R. A. Susott, R. E. Babbitt, D. D. Wade, I. Bertschi, D. W. T. Griffith, and W. M. Hao, Emissions of formaldehyde, acetic acid, methanol, and other trace gases from biomass fires in North Carolina measured by airborne Fourier transform infrared spectroscopy, *J. Geophys. Res.*, *104*, 30,109–30,125, 1999.

Zaveri, R. A., and L. K. Peters, A new lumped structure photochemical mechanism for large-scale applications, *J. Geophys. Res.*, *104*, 30,387–30,415, 1999.

Zdunkowski, W. G., W.-G. Panhans, R. M. Welch, and G. J. Korb, A radiation scheme for circulation and climate models, *Beitr. Phys. Atmos.*, *55*, 215–238, 1982.

Danksagung

Bedanken möchte ich mich bei den Menschen, die zu dieser Arbeit beigetragen haben.

Zunächst bedanke ich mich bei Prof. Dr. Meinrat O. Andreae und Dr. Hans Graf für die Bereitstellung des spannenden Themas, die sehr guten Arbeitsmöglichkeiten, sowie der Möglichkeit, selbständig arbeiten zu können.

Prof. Dr. Graßl danke ich für die spontane Zusage, meine Arbeit zu begutachten, sowie Prof. M. Schatzmann und Dr. G. Lammel für die Bereitschaft zur Teilnahme an meiner Prüfungskommission.

Bei Christiane Textor, Michael Herzog und Josef Oberhuber bedanke ich mich für die Entwicklung von ATHAM, sowie die Unterstützung bei allen meinen Fragen bzgl. ATHAM.

Bei Thomas Trautmann und Olivier Boucher bedanke ich mich für viele, oft spontane, fruchtbare Diskussionen.

Mein besonderer Dank gilt Barbara Früh, für die Durchführung der 3-dimensionalen Strahlungstransportrechnungen, sowie für die intensiven Diskussionen der Ergebnisse.

Für die vielfältige Hilfe bei technischen und fachlichen Fragen gilt mein Dank der Modellierungsgruppe, insbesondere Patrick Jöckel, Rolf von Kuhlmann, Roland von Glasow, Rolf Sander, Christoph Brühl, Benedikt Steil und Mark Lawrence.

Für die gute Zusammenarbeit mit der Cloud and Aerosol Research Group an der University of Washington, Seattle, sowie die Bereitstellung der Meßdaten möchte ich mich bei Peter V. Hobbs, Santiago Gassó, Dean Hegg, Art Rangno und Tom Wilson bedanken.

Bei Sue Ferguson und Roger Ottmar bedanke ich mich für die Bereitstellung der Daten des EPM-Modells, sowie für die ausführlichen Diskussionen.

Für die unkomplizierte Bereitstellung der AVIRIS-Daten bedanke ich mich bei Yoram Kaufman und Rong Rong Li.

Bei Johann Goldammer, Günther Helas, Tobias Zorn, Florian Resch und Hans Page bedanke ich mich für die interessanten Einblicke in die vielfältige Welt der Feuerforschung, die meine Faszination für das Feuer geweckt haben.

Für die immer angenehme Atmosphäre im Büro bedanke ich mich bei Olga Mayol-Bracero.

Meinen Eltern und Tanja danke ich für ihre Unterstützung.